Decentralized Control of Electromagnetic ChipSat Swarm Formations

Rui Manuel Gomes Gondar

Dissertação para obtenção do Grau de Mestre em
Engenharia Aeronáutica
(Mestrado integrado)

Orientador: Anna Guerman
Orientador: Danil Ivanov

maio de 2021

Acknowledgements

I would like to thank my coordinator, Prof. Dr. Anna Guerman, for the opportunity to work on this project and for inspiring my interest in the field of astrodynamics. To Prof. Dr. Danil Ivanov, with whom I worked directly with on the article developed during this period, thank you for your guidance and patience throughout this challenging learning experience.

A special thank you to my parents, for teaching me the value of education, and for always supporting my choices. To my grandfather, for his kindness and wisdom.

And finally, to my friends, thank you for standing by me along the way.

Resumo

Formações de pequenos satélites oferecem novas opções para exploração espacial e experiências científicas. Grupos de satélites, operando a curtas distâncias relativas, possibilitam importantes aplicações tais como instrumentação espacialmente distribuída para amostragem atmosférica ou sistemas de sensoriamento remoto. A capacidade de controlar de forma independente o movimento de cada satélite é crucial para estabelecer uma formação em enxame, utilizando um grande número de satélites movendo-se ao longo de trajetórias relativas limitadas. Este tipo de missão impõe várias restrições ao nível do consumo de energia, da massa e do tamanho dos satélites, consequentemente, é necessária uma abordagem autónoma e auto-sustentável para assegurar o controlo das trajetórias relativas. Um novo conceito de satélite miniatura, denominado *ChipSat*, consiste de uma única placa de circuito impresso que pode ser equipada com diferentes conjuntos de componentes microelectrónicos. Este estudo considera um enxame de *ChipSats* equipados com *magnetorquers*, operando a distâncias relativas extremamente reduzidas, e usando a força de interação eletromagnética para controlo do movimento relativo e orientação dos satélites, assumindo que a posição absoluta e relativa de cada unidade é conhecida. Apesar das limitações impostas por usar os *magnetorquers* como únicos atuadores a bordo, a interação magnética dipolar pode ser usada para limitar trajetórias relativas e estabelecer um enxame compacto. Seguindo uma abordagem descentralizada, os *ChipSats* são periodicamente ligados em pares intermutáveis de modo a aplicar o algoritmo de control baseado no teorema de Lyapunov, impedindo o aumento da distância relativa entre todos os satélites no enxame. O momento magnético dipolar é usado para amortecimento da velocidade angular quando o control orbital não é necessário, e uma força eletromagnética repulsiva é usada para controlo de colisão quando dois ChipSats estão perigosamente próximos. A análise de performance é feita através de simulações Monte Carlo no MATLAB, estudando os parâmetros operacionais e o efeito das condições iniciais após o lançamento.

Palavras-chave

Voo em formação, Enxame de satélites, *ChipSats*, Algoritmos de control da orientação e navegação, Controlo eletromagnético descentralizado, *Magnetorquers*, Equações HCW

Abstract

Small satellite formation missions offer new options for space exploration and scientific experiments. Groups of satellites flying within short relative distances allow various important applications, such as spatially distributed instruments for atmospheric sampling or remote sensing systems. The ability to independently control the relative motion of each satellite is crucial to establish a swarm formation, using a large number of satellites moving along bounded relative trajectories. This type of mission poses several constraints on mass, size, and energy consumption; therefore, an autonomous and self-sufficient approach is necessary to assure relative motion control. A novel concept of miniaturized satellites, referred to as ChipSats, consists of a single printed circuit board which can be equipped with different sets of microelectronic components including power and communication systems, a variety of sensors, and a microcontroller. This study considers a swarm of ChipSats equipped with magnetorquers, operating at extremely short relative distances, and using the electromagnetic interaction force for relative motion and attitude control, assuming the absolute position and relative state of each unit is known. Despite the limitations imposed by using magnetorquers as the sole actuators onboard, the dipole interaction between drifting satellites can be used to achieve bounded relative trajectories, and to establish and maintain a compact swarm. Following a decentralized approach, the ChipSats are periodically linked in interchangeable pairs in order to apply the Lyapunov-based control algorithm and prevent relative drift between all satellites in the swarm. The magnetic dipole moments are used for angular velocity damping when orbit control is not required, and a repulsive collision avoidance electromagnetic control force is applied when two ChipSats are within dangerously close proximity to each other. The performance assessment is conducted through Monte Carlo simulations using MATLAB, by analyzing operational parameters and the effect of initial conditions after deployment.

Keywords

Formation flying, Satellite swarm, ChipSats, GNC algorithms, Attitude control, Relative motion control, Electromagnetic control, Decentralized control, Magnetorquers, HCW equations

Contents

List of Figures

List of Tables

List of Acronyms

ATO	Along-Track Orbit
CanX	Canadian Advanced Nanospace eXperiment
CCD	Charge-Coupled Device
CEP	Celestial Ephemeris Pole
CME	Coronal Mass Ejection
COTS	Commercial Off-The-Shelf
DOF	Degrees of Freedom
ECI	Earth-Centered Inertial
ESA	European Space Agency
FIONA	Formation flying Integrated Onboard Nanosatellite Algorithm
GNC	Guidance, Navigation and Control
GNSS	Global Navigation Satellite System
GPS	Global Positioning System
HCW	Hill-Clohessy-Wiltshire
ISS	International Space Station
ISL	Intersatellite link
LEO	Low Earth Orbit
LQR	Linear Quadratic Regulator
LVLH	Local-Vertical Local-Horizontal
MEMS	Microelectromechanical system
OASYS	Onboard Attitude System Software
PCB	Printed Circuit Board
PCO	Projected Circular Orbit
PRISMA	Prototype Research Instruments and Space Mission Technology Advancement
RealNav	Relative Navigation algorithm
SWIFT	Silicon Wafer Integrated Femtosatellite
UHF	Ultra-High Frequency
VBS	Visual-Based Sensor

Nomenclature

a	Semi-major axis	$[m]$
$\boldsymbol{a}_{J2}$	Second harmonic acceleration	$[m/s^2]$
b	Semi-minor axis	$[m]$
$\boldsymbol{B}_{geo}$	Geomagnetic field	$[T]$
$\boldsymbol{B}_j$	Magnetic field	$[T]$
$C_1, \ldots, C_6$	HCW constants	$[m]$
E	Eccentric anomaly	-
e	Eccentricity	-
$\boldsymbol{F}_{ij}$	Force	$[N]$
G	Gravitational constant	$[m^3/kg\ s^2]$
$\boldsymbol{h}$	Angular momentum	$[kg\ m^2/s]$
i	Inclination	$[^o]$
$\boldsymbol{J}$	Inertia tensor	$[kg\ m^2]$
J_2	Second harmonic coefficient	-
M	Torque	$[N\ m]$
m	Mass	$[kg]$
m_0	Vacuum permeability constant	$[T\ m/A]$
$\boldsymbol{m}_i, \boldsymbol{m}_j$	Magnetic dipole moment	$[A/m^2]$
$\boldsymbol{m}_{damp}$	Angular velocity damping moment	$[A/m^2]$
$\boldsymbol{m}_{geo}$	Geomagnetic dipole moment	$[A/m^2]$
N	Number of satellites	-
n	Mean motion	$[rad/s]$
p	Semi-latus rectum	$[m]$
R_E	Earth's equatorial radius	$[m]$
$\boldsymbol{R}_i, \boldsymbol{R}_j$	Absolute position vector	$[m]$
$\boldsymbol{r}_c$	Center of mass	$[m]$
$\boldsymbol{r}_{ij}$	Relative position vector	$[m]$
T	Orbital period	$[s]$
t	Time	$[s]$
$\boldsymbol{u}_{ij}$	Control acceleration vector	$[m/s^2]$
$\boldsymbol{V}_i, \boldsymbol{V}_j$	Absolute velocity vector	$[m/s]$
$\boldsymbol{X}_i, \boldsymbol{X}_j$	State vector	-
$\boldsymbol{x}_{ij}$	Relative state vector	-
θ	True anomaly	$[^o]$
μ	Earth's standard gravitational parameter	$[m^3/s^2]$
τ	time of passage at the periapsis	$[s]$
Ω	Longitude of the ascending node	$[^o]$
$\boldsymbol{\omega}$	Angular velocity vector	$[^o/s]$
ω	Argument of periapsis	$[^o]$
Λ	Quaternion	-

Chapter 1

Introduction

New approaches to space exploration have motived extensive research and development of multi-satellite systems in an attempt to distribute and enhance the capability of monolithic spacecrafts. These complex systems consist of multiple smaller units, flying at short relative distances from one another or in similar orbits, working simultaneously towards the same task. Small satellite formations offer new scientific and commercial applications as distributed sensor systems due to the increasing capability of its low-power microelectronics, flexible modular design, and tolerance for individual unit failure. The performance of the formation can be maintained over several launches by replacing malfunctioning or damaged units. From an economic standpoint, smaller satellites are far easier to manufacture and launch into orbit than its larger counterparts. Budget reductions and technological innovation over the years originated new classes of satellites that can be mass-produced at a reduced cost and deployed in large numbers from a single launch. The classification of small satellites given in Table 1.1 is commonly used among the scientific community.

Table 1.1: Classification of small satellites

Class	Mass (kg)
Minisatellite	100 - 500
Microsatellite	10 - 100
Nanosatellite	1 - 10
Picosatellite	0.1 - 1
Femtosatellite	0.01 – 0.1
Attosatellite	0.001 – 0.01

The potential for instrument distribution with the reduced cost of mission makes these formations an accessible and promising alternative for scientific data acquisition and communication networks.

1.1 Background

Small satellites are not a novel concept and were particularly popular during the first decade of space exploration. The first active nanosatellite, Vanguard 1, with a mass of less than 10 kg, solid-state electronics and primitive solar cells was introduced in 1958. It carried two continuous wave transmitters for monitoring the spacecraft's internal temperature and the total integrated electron density between the satellite and the ground station. At the time, the former Soviet Union was launching larger and more complex satellites, such as the Sputnik 1, launched in 1957 with a mass of 84kg, which is known

today as the first artificial satellite to orbit Earth. Nanosatellite launches seized between 1968 and 1996. Due to the limited technology available, larger, more expensive satellites were necessary to satisfy increasingly challenging mission requirements. This was the period of government-funded space programs and large commercial geosynchronous satellites, as part of a global communications network. As technology matured, the integrated circuit density of transistors doubled roughly every 2 years, resulting in the significant improvement of microprocessors and other microelectronics. In 1997, Sputnik 40 was deployed. A 4 kg, 1/3 scale model of Sputnik 1, built forty years after the historical launch, marked the reappearance of nanosatellites. In the early 2000s, several nanosatellites already included 3-axial attitude control, gas thrusters, a variety of charge-coupled device (CCD) sensors, GPS receivers and ultra-high frequency intersatellite links for data exchange. The technological leap to lithium-ion batteries significantly decreased mass per unit stored energy. CubeSats, with a mass of 1kg, became widely available with inexpensive, state-of-the-art electronics. CubeSats are nanosatellites built to standard dimensions (Units or "U") of 10 x 10 x 10 cm per U. The CanX-1 mission, launched in 2003, had five 1U CubeSats with active magnetic 3-axial attitude stabilization and complementary metal-oxide-semiconductors imager sensors for observation and star tracking, setting the standards for CubeSats launched in the following years [1, Secs 1.I-1].

The evolution of satellites enabled the development of multi-satellite systems as distributed, self-organizing formations. As opposed to constellations (i.e. GPS), where each satellite is individually controlled from a ground station, formations can self-organize based on direct intersatellite data exchange, distributed control, and relative navigation. Formation flying applications include radar and optical interferometry, rendezvous/docking and gravitational/magnetic field measurements. The Global Navigation Satellite System (GNSS) provides a convenient source for relative positioning; using triangulation methods, three-dimensional space can be derived from pseudorange measurements. Additionally, orbital control is necessary to achieve bounded relative trajectories after deployment, as well as for formation maintenance and re-configuration during the operational period. Autonomous relative motion and accurate attitude control are essential for the spatial distribution and pointing precision required for accurate measurements and reliable communication links. Although current technology has made this possible on the nanosatellite level, it still poses a significant challenge for femtosatellite formations today, due to size, mass, and power restrictions [1, Secs 15.I–3d].

The Prototype Research Instruments and Space Mission technology Advancement (PRISMA) was the first demonstration of autonomous formation flying using high precision relative GPS and RF metrology instruments. Launched in 2010, it served as a

testbed for Guidance, Navigation and Control (GNC) algorithms and sensors for closed-loop flying formations and rendezvous. This mission was executed with two expensive, high-performance satellites with a mass of 145 and 50 kg, in a collaborative effort between international organizations. For several years, the Space Flight Laboratory from the University of Toronto Institute for Aerospace Studies has been conducting research on nanosatellite formation flight with their smaller-scale CanX missions. Launched in 2014, the CanX–4 and CanX–5 dual-spacecraft mission was the first successful demonstration of autonomous nanosatellite formation flight with sub-meter control error and centimeter-level relative position determination, using 6.85 kg 2U CubeSats [1, Secs 16.I–3e]. Due to its reduced production cost and increasing operational capability, CubeSats are now implemented in large constellations and formation flying missions. Although the quality of the collected data and individual reliability of each unit can be further improved, the ability to provide in-situ measurements from numerous sample points in multiple locations simultaneously, outweighs the disadvantages of this type of orbital system. This methodology was successfully used by Planet Labs Inc. in their 3U CubeSats, referred to as "Doves" [2]. This constellation operates in Low Earth Orbit (LEO) at 475 km of altitude, using 29 Megapixel sensors for real-time land surface observation, with 3.7 m ground resolution and a temporal cadence of ~1-72 h. Although temporal resolution – the time needed to acquire data for the exact same location - is lower than that provided by geostationary satellites, their spatial resolution is several orders of magnitude higher when compared with pixel sizes of 0.25–2 km for geostationary imagers. In some cases, consecutive data acquisition can provide multiple images of the same region within few minutes. The multi-spectral high resolution imagery provided is ideal for monitoring geophysical phenomena such as volcanic activity [3]. According to the Nanosats Database [4,5], that lists up-to-date information on past, present and future small satellite missions, by late-2020 Planet Labs had an astonishing 418 Doves in orbit, making it the largest commercial nanosatellite constellation to date. The constellation was replenished over several launches, and includes upgraded iterations of their proprietary CubeSats, now called "Super Doves", capable of producing five times as much data as its predecessors [6].

Given the progress in miniaturization and the knowledge gathered from previous small satellite missions, the next step in the technological evolution of distributed space systems may be femto- or attosatellites. These tiny spacecrafts consist of either single or stacked printed circuit boards (PCB) and were initially developed as passive devices without any type of control. Due to their small size, a minimalist configuration must be adopted with only a few essential systems mounted onto the PCB. Traditional integrated propulsion systems cannot be sufficiently scaled down to match mass and size requirements, leaving room for the development of alternative, propellant-free approaches to control.

Nevertheless, the reduced the cost and build complexity of these devices dramatically expands its accessibility to unprecedented level for both academic and recreational developers. Large clusters of ChipSats equipped with a variety of electromagnetic and nanofluidic sensors, and microelectromechanical systems (MEMS), can potentially allow large-scale, in-situ atmospheric, gravitational, and magnetic surveys in LEO that are impractical or impossible to current multi-satellite systems, allowing hundreds or even thousands of data points to be collected simultaneously over large spatial volumes with high-degree tolerance for individual unit failure [7].

KickSat is project founded in 2011 with the goal of advancing core technologies needed to enable low-cost ChipSat missions. The satellite design, called “Sprite”, consists of a 3.5 x 3.5 cm PCB equipped with solar cells, a microprocessor with a built in radio, an antenna, an amplifier, and passive switching circuitry. The first prototypes developed served as a testbed for non-radiation-hardened electronic components in space environment. In 2014, a total of 104 Sprites were launched into LEO in a 3U CubeSat. Although the CubeSat was successfully launched, a critical software error prevented the Sprites from being deployed. The main objective of the mission was to establish direct communication between the satellites in LEO and Earth ground stations [8]. A second mission eventually reached orbit in 2019, and successfully demonstrated the technology by deploying and receiving signals from the deployed Sprites, proving the feasibility of ChipSats. Direct communication between ChipSats and a ground station is difficult to achieve with limited power, lack of attitude control, and limited radio frequency bandwidth. A different approach can be taken by utilizing the CubeSat used to deploy the ChipSats for communication relay between Earth and the ChipSats. The KickSat Sprites weigh just 5 grams, and are therefore classified as attosatellites, whose mass ranges from 1 to 10 grams. However, these tiny satellites operate solely on direct solar power, with no additional batteries for energy storage, and can still transmit short bursts of frequencies in the 400 megahertz range with only milliwatts of power. With energy storage capability and a variety of sensors and communication systems available, only limited by the PCB size, it is safe to assume ensuing prototypes will be within the femtosatellite level. The next generation of KickSat Sprites will include GPS navigation capability and sensors to measure atmospheric behaviors and magnetic fields [9].

In the context of this dissertation, the term “swarm” refers to a numerous cluster of satellites utilized as a distributed space system moving along arbitrary relative trajectories and operating independently without the need for ground station control. Ideally, the spacecrafts should be capable of individual coordinated motion control, in 6 degrees of freedom (DOF), for maintaining relative positions and stable pointing attitude, in order to

enhance its synergetic interactive behavior. This type of formation requires small, low-mass satellites, capable of carrying the required payload (sensors). The first approach to swarm formations was conducted by the European Space Agency (ESA) with a modest three satellite swarm-type formation to study the direction and strength of Earth's magnetic field in LEO with high-level accuracy [10]. A more ambitious concept is proposed in article [11], using hundreds to thousands of 0.1 kg femtosatellites in swarm formation. Different wafer fabrication and integration techniques are considered to produce the Silicon Wafer Integrated Femtosatellites (SWIFT) equipped with sensing and control capabilities. The goal of this study was to assess the feasibility of SWIFT fabrication as well as the individual and synergetic GNC capability. The article acknowledges the importance of highly nonlinear orbital and attitude dynamics, fuel-efficient algorithms to meet the optimal performance requirements desired for swarm formations. Fully centralized algorithms for a large swarm of femtosatellites results in significant computation and communication requirements. Consequently, decentralized feedback control algorithms should be considered [11].

1.2 Review of Formation Flying Research

This section gives a descriptive analysis of past formation flying missions, focusing on orbital maneuvers and GNC algorithms. The missions presented in 1.2.1 and 1.2.2 successfully demonstrated new technology applications, laying the foundations for the future of formation flight. The mission in 1.2.3 does not classify as formation flying but as a swarm, nevertheless, it represents a significant technology advancement and established the operational feasibility of a new class of small satellites referenced throughout this dissertation.

1.2.1 PRISMA

The Prototype Research Instruments and Space Mission technology Advancement or PRISMA was the first autonomous rendezvous formation flying mission demonstration. The project was founded in 2005 by the Swedish Space Corporation in collaboration with German Aerospace Center, the French National Space Center and the Technical University of Denmark and served as in-orbit testbed for GNC algorithms and sensors for advanced closed-loop formation flight with decimeter precision using relative GPS and radio-frequency metrology instruments. Additionally, proximity autonomous maneuvering was performed with a visual-based sensor (VBS) using "line of sight" information only [12]. The main objectives of the mission were:

- Autonomous formation flight based on GPS and formation flying radio-frequency sensor system

- Homing and rendezvous based on a VBS only
- Proximity operations, based on GPS and VBS
- Final Approach and Recede Operations based on VBS only

On June 15, 2010, two satellites, presented in Figure 1.1 were launched together into a 720-780 *km* sun synchronous orbit. The follower spacecraft, also referred to as "Main", classified as a minisatellite with a mass of 145 kg, features 3-axis stabilization with reaction wheels and magnetic torque rods, based on a stellar-inertial sensor system for star-tracking, and is equipped with a hydrazine propulsion system providing full orbit control capability. The leader or "Target" spacecraft, which classifies as a microsatellite with a mass of 45 kg, also features 3-axis stabilization but with an attitude control system based on sun sensors, a magnetometer and magnetic torque rods, however, it does not have any orbit control capability [13].

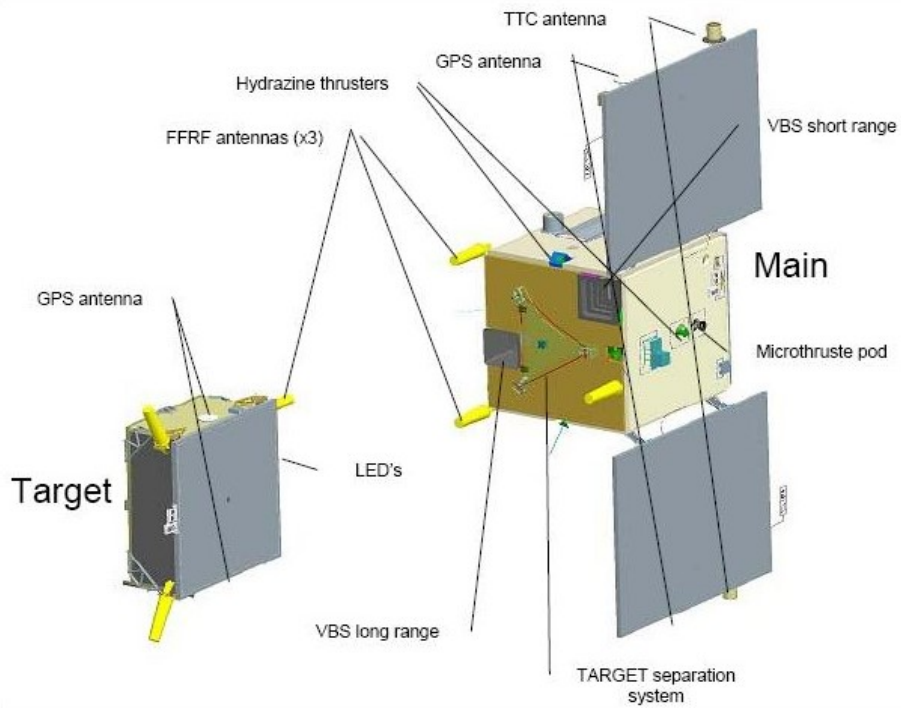

Figure 1.1: Main and Target configuration [12]

While the Main spacecraft is equipped for full maneuverability, the Target is solely used as a reference for the different experiments performed. To reduce the cost, size, and weight, the payload was minimized. Since there are no reaction wheels on the Target, the torque rods are the only actuators on board, and can only provide magnetic attitude control along the two axes normal to the Earth's magnetic field. The attitude control system of the Target spacecraft can operate in two different modes. *Sun Acquisition and Safe Mode* are used to reduce the angular rates after separation from the Main. Once the system is

stabilized, the spacecraft points its solar array towards the Sun, tumbling around the z-axis with a lower angular rate (typically 0.5 deg/s). *Normal Mode* can be used in the manual pointing sub-mode, mimicking a lost spacecraft turning around the z-axis with an angular rate of 0.2 deg/s, or in Sun/zenith pointing sub-mode, with the satellite turning around the z-axis which can point any direction between the sun vector and the orbit normal, depending on the mission priority [14]. The attitude estimation filter onboard the Target is a 9-state extended Kalman filter with time-varying gain. Three states are dedicated to attitude and three states to angular rate. The additional three states were added to estimate the spacecraft residual magnetic moment, for improved attitude estimation and control. The attitude controller is based on Linear Quadratic Regulation (LQR) control law using linearized dynamic equations around the satellite's operational state. Disturbances caused by gravity gradient torque, gyroscopic torque and residual magnetic dipole torque were considered and successfully compensated despite the limitations of the passive magnetic control. The results obtained from the 3-axial attitude control used on the Target satellite demonstrated the feasibility of passive magnetic actuators for the mission requirements [15].

The GNC experiments conducted with the Main spacecraft for autonomous formation flying and rendezvous, proximity operations and final approach/recede maneuvers were designed to represent important model missions. Orbit control approaches vary from VBS to GPS-based navigation, depending on the experiment phase. A summarized description of the experimental procedures is presented below [13]:

Autonomous formation flying concerns passive relative orbits used to create a natural periodic motion. Orbit control is required to correct external disturbances responsible for orbit degradation, such as solar pressure, aerodynamic drag, and gravitational irregularities. Relative distances range from 20 to 5000 m, and control is GPS-based with navigation data provided by the Kalman navigation filter. The states coming from the filter are correlated to determine the relative position and velocity of the satellites. The autonomous flying formation uses a feedback orbit control function on model-predictive control, taking up to seven input relative position coordinates in order to optimize the next control request based on propagation over the planning points. Propagation is implemented for the general case of elliptical orbits. The feedback control function requests a certain impulse from a thruster command distribution function, which calculates the commands to each individual thruster, taking into account spacecraft attitude as well.

Homing and Rendezvous consists of a complete and autonomous approach to rendezvous performed using only the VBS onboard the Main satellite. It includes the autonomous position determination of the Target, orbit phasing, intermediate transfer, and the final approach, get within a relative distance that allows the approach/recede maneuver functions to take over. For each execution, the Main spacecraft is placed in a specific relative orbit by ground command after which autonomy is enabled. An orbit-determination filter is initialized to estimate the position and velocity of the Target, while the Main's orbit propagator serves as reference. The data from the VBS is processed on the star-tracker unit. The VBS uses one long range and one short range CCD camera to deliver inertial direction to the Target from up to 100 000 *m* down to 10 m. From approximately 100 *m* and below, the light on the CCD coming from the solar illumination of Target will blind the sensor, thus making inertial determination of Target's location impossible using only the long range camera. In this case, attitude-determination cameras are used. The short range camera is used from a few tens of meters down to less than 1 m. When orbit alignment is complete, the Main satellite will have about the same mean Keplerian elements as the Target, except for the mean anomaly.

Proximity operations and final approach/recede were conducted with forced trajectories in close proximity of the Target, ranging from 5 to 100 m. The navigation is based on a virtual network of flight-paths designed for on-orbit servicing, inspection, and assembly about large objects with appendages and no-fly zones, such as the International Space Station (ISS). One approach to navigation uses the VBS to track the flashing LED markers and geometric features of the Target to determine relative distance and attitude. The navigation plan is commanded according to the allowed points and flight-paths established by the virtual map. Alternatively, navigation can be guided by GPS measurements with the same model-predictive orbit control function used for the autonomous formation flying mode.

These experiments were particularly interesting to assess the performance of the orbit determination filter. The states of the satellites were accurately determined down to 0.05 *m* using relative GPS. Despite initial calibration errors of up to 1 *km* in range and substantial velocity errors in the initial relative orbits, the filter was successful in converging relative trajectories to the correct state once the corrected measurements were considered. The autonomous formation flying implemented a relative elliptical orbit centered 3 *km* behind the Target, spanning 2 *km* around its center with a variation of 1 *km* in radial direction. The first phase of the rendezvous, during which the VBS is used to perform a systematic search for the Target's LED patterns, was also subject to state

estimation errors due to the premature activation of the filter caused by other light sources in the line of sight [16].

1.2.2 CanX-4 and CanX-5

The Canadian Advanced Nanospace eXperiment (CanX) program was founded in 2001 at the Space Flight Laboratory at the University of Toronto Institute for Aerospace Studies to develop accessible state-of-the-art nanosatellite technology for new scientific space applications. The CanX satellites use commercial off-the-shelf (COTS) components in order to take advantage of the latest technologies and to benefit from their significantly reduced cost when compared to radiation hardened components. The CanX-4 and CanX-5, launched in June 2014, are two identical 6.85 kg nanosatellites utilized to demonstrate autonomous formation flying in LEO with accurate orbit control, relative position estimation and 3-axis attitude control. The two satellites are classified as 2U CubeSats and based on a 20 cm cubic "generic nanosatellite bus", an adaptable modular template which is suited for several different mission applications and significantly reduces the structural design and development time. The structure consists of six external panels and two internal trays in order to maximize the payload bay while providing additional internal room for scientific instruments, sensors, or communication devices. This configuration includes standard components, such as solar cells, communication antennas, a magnetometer, sun sensors for attitude determination, and three reaction wheels combined with a magnetorquer for accurate attitude control. The reaction wheels are used for fine pointing accuracy while the magnetorquer coils are used for detumbling and dumping angular momentum, preventing the saturation of the wheels. A view of the twin satellites' layout is presented in Figure 1.2. The CubeSats are equipped with two onboard computers, each with a ARM7 microcontroller, one computer for handling communication with the ground station and for processing telemetry data, the other interfaces with the attitude sensors/actuator and runs the attitude control algorithm. Given the specific mission description, the additional room in the payload bay houses a third computer to interface with the propulsion system and GPS receiver, and to run the formation flying algorithm. The main mission objectives were the following [17]:

- Autonomous achievement and maintenance of several dual-satellite formations
- Demonstrate carrier phase differential GPS techniques for relative position determination measurements with an error of 0.01 m or less
- Position control with sub-meter error
- Develop and validate fuel efficient formation flying algorithms
- Establish an intersatellite communication system

In order to demonstrate precise formation flight with sub-meter control error, four different formation were designed in a leader-follower configuration. Two formations are Along-Track Orbits (ATO) with a relative separation distance of 500 m and 1000 m, in which the leader and the follower maintain a fixed relative separation in the same orbit, but with different true anomaly. The other two are Projected Circular Orbits (PCO) with a relative separation distance of 50 m and 100 m, which is a type of leader-centered circular orbit when projected into the vertical plane of the Local-Vertical Local-Horizontal (LVLH) reference frame. The circular reference trajectories were periodic solutions to the Hill-Clohessy-Wiltshire (HCW) equations to obtain a linear approximation of the relative motion of the follower with respect to the leader. The dynamics of the two satellites are non-linear and no set of solutions can provide bounded relative motion due to natural occurring perturbations, such as the J2 effect. However, periodic solution can produce reference trajectories particularly useful for controller design and orbit tracking. An analytical description of the HCW equations is provided in Section 2.4. The trajectories are given by the following solutions to the HCW equations:

$$x(t) = \frac{1}{2} d_1 sin(nt + \alpha)$$
$$y(t) = d_1 cos(nt + \alpha) + d_3$$
$$z(t) = d_2 sin(nt + \beta) \quad (1.1)$$

where n is the mean orbital angular velocity of the leader satellite and $d1$, $d2$, $d3$, α and β are specific formation design parameters. The solutions are expressed in the rotating LVLH reference frame, also referred to as the Hill frame. Table 1.2 exhibits the design parameters for the four different formations planned for this mission [18].

Table 1.2: CanX-4 & CanX-5 trajectory parameters

Formation	***d1* (m)**	***d2* (m)**	***d3* (m)**	**α (rad)**	**β (rad)**
ATO 1000 m	60	30	1000	0	π/2
ATO 500 m	60	30	500	0	π/2
PCO 100 m	100	100	0	0	0
PCO 50 m	50	50	0	3π/2	3π/2

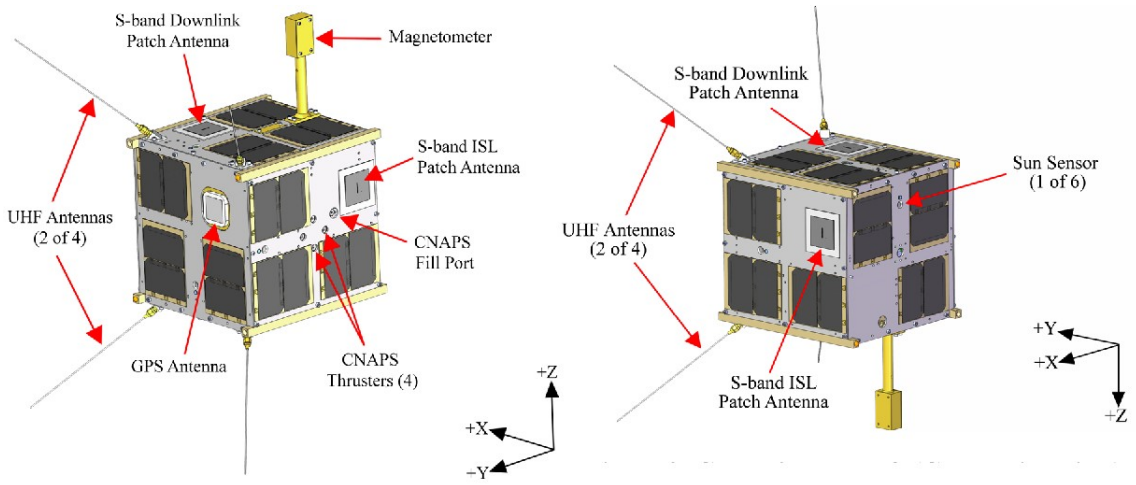

Figure 1.2: Opposite views of the of the CanX-4/-5 external structure [17]

Both satellites run on three pieces of navigation and control software integrated onboard in order to achieve mission requirements: The formation flying integrated onboard nanosatellite Algorithm (FIONA), the relative navigation algorithm (RealNav), and the onboard attitude system software (OASYS). During fine formation control, OASYS commands the attitude of the spacecraft in inertial quaternions computed by FIONA and selects the thrusters to be used in upcoming maneuvers. In the absence of an attitude target OASYS is programmed to revert autonomously to zenith-tracking. The attitude of the follower is adjusted to maximize the number of satellites in view and is sent via intersatellite S-band radio link to the leader so that both satellites acquire the same attitude, this improves relative navigation a minimizes differential perturbations. Attitude is determined using an extend Kalman filter to estimate the quaternion and angular velocity, attitude is then propagated using quaternion kinematics and Euler's equation of angular motion. On the leader satellite the reaction wheels are used for attitude pointing and the magnetorquers for angular momentum dumping, while the follower's OASYS selects thrust nozzles to reduce angular momentum instead of the magnetorquers to improve attitude accuracy. The relative navigation algorithm RealNav is an extended Kalman filter which uses carrier phase differential GPS to estimate the state of the follower relative to the leader and provide input data for the formation control laws. The estimated dynamic state vector depends on the number of GPS satellites commonly tracked by both spacecrafts, limited by the GPS receiver to a maximum of 14 independent communication channels. RealNav provides scalar measurements, updated every 5 seconds, by processing pseudorange and carrier phase measurements from each GPS satellite connection. FIONA uses the relative state measurements to autonomously compute the necessary formation control maneuvers and to determine the tracking error from a set of reference trajectories. Using a linear state feedback control law, FIONA

corrects this error and communicates the thrust directions to the propulsion system and to the attitude control system. An extended Kalman filter is used to estimate the state of both satellites for auxiliary control parameters and to convert the relative state estimated by RealNav into the LVLH frame in order to apply the formation control law. The filter is necessary to reduce the noise from the GPS signal, in order to obtain accurate single-point position. FIONA uses both continuous and discrete steady-state forms of LQR to minimize the dynamic error of the HCW equations. Using the reference trajectories as a solution to the equations of relative motion, the LQR output is converted to a control impulse to be applied by the thrusters. The continuous form is primarily used during reconfiguration maneuvers to transfer the follower from one formation to the next. The discrete form is used for control gain calculation throughout all formation flying orbits enabling longer periods with no control actuation required [18].

The formation control experiment in the 1000 *m* ATO was established and maintained for the required orbit period. However, the control error was kept below 1 *m* only during 88% of the formation period. This was caused by poor navigation performance which led FIONA to command a wrong attitude target. With the GPS antennas pointing away from zenith, fewer satellites were commonly tracked, reducing the precision of control thrusts. Despite not obtaining the desired sub-meter control error, the maximum deviation observed during the experiment was 2.25 m, which is still a positive result. After identifying the cause of the reduced performance during the first experiment, a software update was performed before attempting further experiments. With improved attitude targeting, the second experiment in the 500 *m* ATO was successful, maintaining sub-meter control error for the entirety of the formation period following the initial convergence. During the initial phase of the two PCO experiments, the control error was larger than expected likely due an inaccuracy in the magnitude/direction of thrust impulses, but after the LQR took over the control error was successfully reduced to sub-meter level for the remainder of the formation period. The experimental results were considered a complete success with all mission objectives accomplished, pushing the boundary of what can be achieved with nanosatellite technology and formation flying control algorithms [18].

1.2.4 KickSat

The KickSat project was developed in 2011 at Cornell University, and made possible through a crowd-funding campaign on the website Kickstarter that gathered a total of $74,586 (the initial goal was $30,000) pledged by 315 individual backers [19]. Backers were rewarded according to the amount donated, from having their name silkscreened onto flight hardware to receiving their own development kit with a full functioning

satellite. The hardware designs, code, and documentation for all of these systems were released under open-source licenses [20]. This project was inspired by the miniaturization and increasing capability of low-cost COTS components especially driven by the smartphone industry, which enabled to the development of a minimal chip-sized satellite concept using the same devices and techniques used in the consumer electronics industry. Due to the passive nature of the satellites, the mission objective was not to perform formation flight but to demonstrate the communication capabilities of ChipSats in large clusters, operating in LEO. Nevertheless, the ability to mass-produce these small devices with a variety of sensors enables a new class of space mission that allows large-scale in-situ surveys of planetary atmospheres and magnetic field measurements. The developed Sprite ChipSat, exhibited in Figure 1.3, is a 3.5 x 3.5 cm PCB attosatellite with a mass of 5 g equipped with low-cost, low-power microelectronics including solar cells, a microcontroller with an integrated radio, a 3-axis magnetometer, and 3-axis MEMS gyro. The microcontroller provides the essential computing and communication capabilities, it includes an integrated Ultra-High Frequency (UHF) transceiver with an output power up to 10 mW and data rates up to 500 kbps. The antenna is made from nitinol, a nickel-titanium alloy, which can be deformed and still return to its original shape, so it could be coiled within a small footprint until deployment. It was designed for easy tuning with a 50 ohm characteristic impedance, which eliminates the need for a matching network. The solar cells were chosen to accommodate the power budget and can deliver up to 60 mA of current at 2.2 volts directly to the electronics with no need for energy storage or power conditioning. The Sprite's approximate maximum power consumption is only 35 mA, leaving a considerable margin for operation, once there is sufficient solar energy to create a radio-frequency emission, the passive switching circuitry engages the microprocessor. Nevertheless, the small size of the ChipSat poses a significant challenge to its communication capabilities. The goal was to setup as many low-cost ground station receivers as possible to attempt direct communication between the Sprites and Earth, despite preliminary studies predicting the signal would be mostly noise. Due to the lack of attitude control, an antenna with an omnidirectional gain pattern is required to transmit the signal over several hundred kilometers [7].

The KickSat spacecraft is a 3U CubeSat composed of a 2U ChipSat deployer that contains the Sprites stacked in columns in a 2-by-2 arrangement, and a 1U bus that provides power, communication, data handling, and attitude determination/control. The ChipSat deployer was designed for simplicity and robustness using COTS components. The Sprites are housed in individual slots, compressed by a spring mechanism which unlocks once deployment is triggered. A deployment example is presented in Figure 1.4. The KickSat-1

mission was launched into LEO with a total of 104 ChipSats onboard, on the SpaceX CRS-3 in April 2014. After the successful separation from the launch vehicle and antenna deployment, telemetry was received by Cornell's ground station and amateur collaborators around the world to analyze and decode flight data and make re-entry predictions. Unfortunately, the Sprite deployment was delayed due to scheduling conflicts with another NASA spacecraft bound for the ISS. After a 14-day delay, the KickSat spacecraft momentarily lost power causing the avionics to reset. As a result, the 16-day deployment timer was restarted. Despite efforts made to uplink an override command, after 25 day in orbit, KickSat-1 re-entered Earth's atmosphere without deploying the payload [21]. A re-flight of this mission, KickSat-2, featuring improved avionics and power systems was developed and prepared for launch at NASA's Ames Research Center in collaboration with Stanford University. Eventually it was launched on the ELaNa-16 mission on board of the Cygnus CRS-10 cargo vehicle and was deployed in February 2019 from the spacecraft's external deployer after departing from the ISS. In March 2019, the 128 Sprites were deployed and signals from several Sprites were received [22]. The Sprites were expected to re-enter the atmosphere and burn up completely within a few days or weeks, depending on atmospheric conditions. There is a real concern regarding space debris hazard caused by ChipSats while still in orbit, however their worst-case maximum orbital lifetime is estimated at 6 weeks.

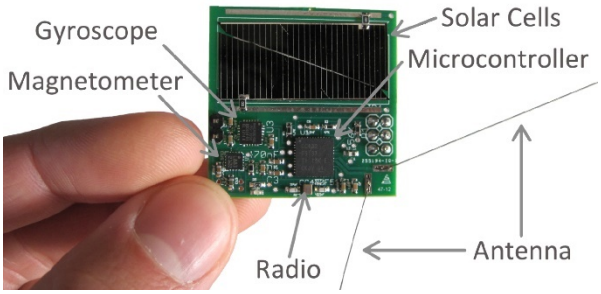

Figure 1.3: KickSat Sprite [21]

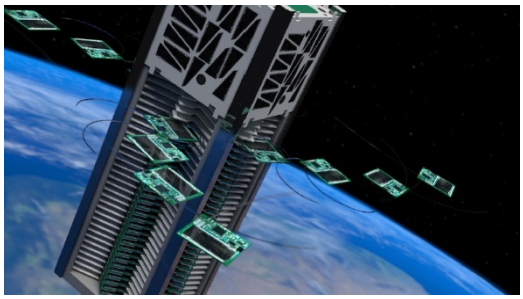

Figure 1.4: KickSat Sprite deployment [21]

Chapter 2

ChipSats

ChipSats are a fairly new type of small satellite, consisting of a PCB with integrated microelectronic components. Their configuration and built-in functions depend entirely on the mission concept. Recent technology advancements driven by consumer-electronics industries, such as smartphones and gaming platforms, resulted in improved onboard computing power, energy conversion and storage, communication systems and data transmission rates. These satellites are conceptually simple and thus can be easily mass-produced with COTS components at a very reduced cost. ChipSats are generally classified as either attosatellites, or in some cases femtosatellites. The inclusion of additional systems and sensors on more complex designs, limited only by the PCB footprint, implies an increased mass, likely surpassing the femtosatellite threshold. Nevertheless, the inherently reduced mass and production cost of these devices allows a large number of ChipSats to be deployed simultaneously from a single launch. ChipSats are designed to operate synergistically in massive clusters in order to collect spatially and temporally distributed data. The scientific applications of ChipSat swarms as distributed space systems can be extended well beyond the Earth, to other planets of our solar system. In our own planet, ChipSats can reach a part of the atmosphere too high for airplanes and balloons, but too low for traditional satellites. Understanding lesser-known segments of the atmosphere will help us to better understand our Earth and its climate. The same principle is applied for in-situ magnetic field measurements and space weather monitoring. The main challenge with these type of satellites remains the implementation of active attitude and orbit control.

2.1. Hardware

An example of a minimal attosatellite design is the 5 g KickSat Sprites passive spacecraft equipped only with essential communication components and no control system or power storage onboard. The KickSat mission established the feasibility of communication across large distances with low-power 10mW transmissions [7]. However, ensuing prototypes designs have since surpassed its operational capabilities. The Monarch, presented in Figure 2.1, is a 2.5 g ChipSat prototype currently under development at Cornell University in an attempt to enhance the core capabilities of their previous Sprite ChipSat. Telemetry and command take place via a 25 mW radio with an embedded antenna and data transmission rates below 84 kbps, since the low-power transmitter cannot accommodate a

high-gain antenna. Rather than receiving large amounts of high-quality data from a few sensors on a single spacecraft, a swarm of Monarchs provides a different sort of dataset from hundreds to thousands of distributed sensors at a lower rate. Each Monarch is equipped with a gyroscope, a magnetometer, and light sensors acting as coarse Sun-sensors for 3-axis attitude determination. Additionally, each ChipSat carries a GPS receiver and antenna for position and velocity determination. A noteworthy technology application on the Monarch design is the inclusion of attitude control by driving electrical current through a coil wire embedded in the PCB in order to create a magnetic field. The magnetic torque interacts with the Earth's magnetic field, as a 2-axis control solution, providing spin stabilization about its normal axis. The inclusion of batteries keeps the satellites operational and thermally regulated during eclipsed orbit periods. Because of its form-factor and high level of integration of the components, Monarchs can reach thermal equilibrium much faster than larger satellites. At this size, it is more energy consuming to keep a battery warm when eclipsed, than the energy that battery can store when sunlit. To ensure constant network operability, a small thermally insensitive capacitor was included in the design to allow the ChipSats to continue to function at a low-duty cycle during eclipse periods [23]. An alternative approach is to use a dawn-dusk Sun synchronous orbit to provide constant solar flux. In a dawn-dusk orbit, the orbit plane remains perpendicular to the incoming solar radiation, the ChipSats would therefore be under direct illumination during the entire orbit period in order to maximize electrical power generation for the payload [24].

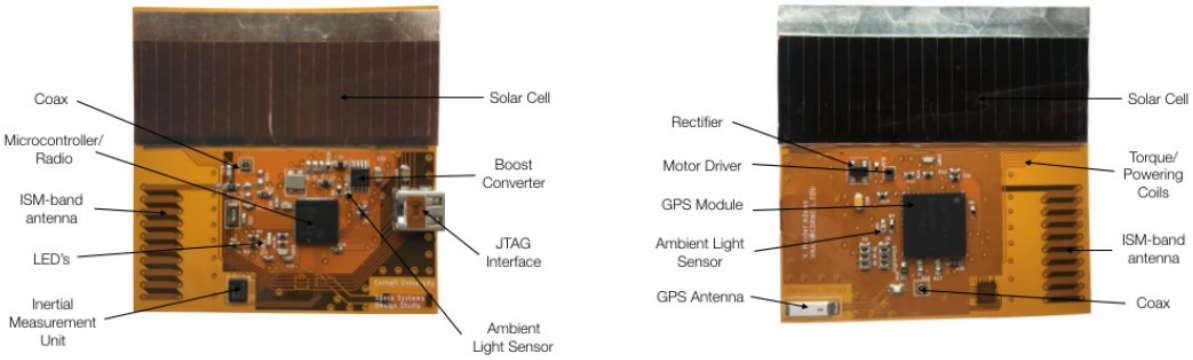

Figure 2.1: Monarch ChipSat prototype [23]

The development and demonstration of ChipSats with active control represents significant progress to swarm formations. The ability to actively adjust the attitude of a satellite enables increased Sun exposure to power the payload, as well as improved stability for optical sensor systems and higher rate RF transmissions. Considering this control strategy, a femtosatellite prototype, exhibited in Figure 2.2, was developed in 2019

featuring an active 3-axial attitude control system using miniaturized orthogonal magnetorquers. Instead of using a low data rate signal for long range transmissions between the satellites and the ground station, the communication system of this ChipSat was designed around a CubeSat deployer which acts as a communication hub for signal relay. The electrical power system consists of a DC-DC converter controller supplied by two 28% high efficiency solar cells with maximum current of 14.5 mA, and maximum output power of 34 mW. The effectiveness of solar power for ChipSats is dependent on the duration of time during orbit for which the solar cells are exposed to the Sun. Power storage options are limited to the potential use of commercial batteries. A small 65 mAh coin battery is used in combination with several capacitors for power storage and buffer, however this technology has not yet been tested in space environment. The ChipSat includes a microprocessor with built-in RF functionality to transmit/receive data through a matching network using a monopole antenna. The attitude of each satellite is estimated through magnetometer and gyroscope measurements via an explicit complementary filter. The magnetorquers, exhibited in Figure 2.3, consist of two orthogonally mounted iron-core torque rods and air-core coil were custom-built to fit the 3.3 x 3.3 x 0.5 cm footprint of the PCB. These are the sole actuators onboard. When activated, these magnetorquers generate magnetic dipoles which interact with the Earth's magnetic field to produce control torques on the femto-satellite's axes [25]. The magnetic dipole moment generated is weaker than in high-performance magnetorquer, but the resulting interaction force may be sufficiently strong to implement relative motion control to nearby Femtosatellites due to their low mass. The swarm formation control strategy described in this dissertation is based on the electromagnetic interaction of the ChipSats. The 3-axial electromagnetic properties of the prototype presented in [25] are used as a reference for the purposes of the developing the proposed control algorithm.

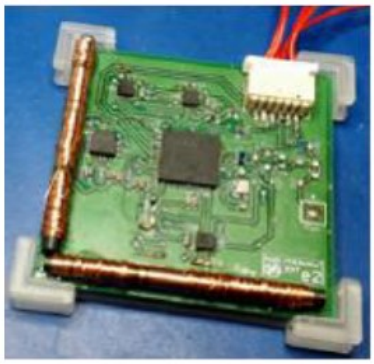

Figure 2.2: Femtosatellite ChipSat prototype [25]

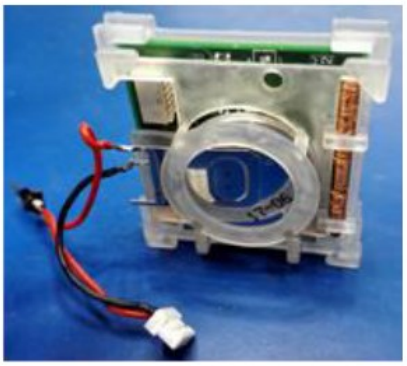

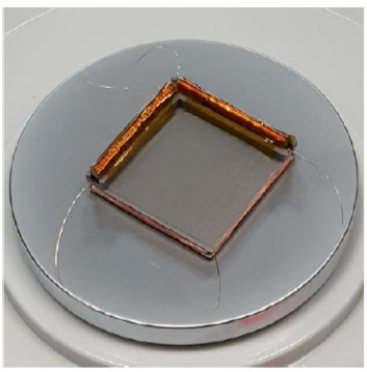

Figure 2.3: Custom-built magnetorquer [25]

2.2 Mission Applications

ChipSats are designed to compose multi-satellite systems and provide different payload options that can be adapted to mission requirements. Due to their unique configuration and capabilities, various scientific missions can be made possible with currently available technology. Furthermore, the potential commercial and scientific return of swarm missions can be considerably enhanced in the near future by optimizing core microelectronic components and data collection sensors. A large number of ChipSats can be stored inside multiple CubeSat carriers and deployed on command to collect spatially and temporally distributed measurements at LEO altitudes. The swarm will operate autonomously in a decentralized manner, while CubeSat carriers can be used to relay the collected information back to the host ground station. This data can be combined with ground-based measurements from other sources to study the effects of space weather on Earth's magnetic field [26].

Changes in the magnetic field can have a significant impact on Earth's biosphere and can also cause disruption to technology-based infrastructures. A Coronal Mass Ejections (CME), such as the Carrington flare [27] which occurred in 1859, can produce extremely powerful geomagnetic storms. CMEs are characterized as massive expulsions of plasma from the Sun's corona, which generate clouds of charged particles that can reach Earth in less than a day. The 1859 geomagnetic storm, although harmless to humans, produced intense auroras around the globe and strong electrical currents capable of taking down telegraph systems, electrocuting operators and starting fires. A much smaller flare affected Québec in 1989, causing a power blackout for a period of nine hours. If an event like the Carrington flare were to occur today, it would cause serious damage to a wide array of electrical networks, global industries, supply chains, and communication satellites [28]. The cumulative worldwide losses could reach up to an estimated $10 trillion US dollars, and full recovery time is expected to take several years. Despite the potential global economic impact, space weather and superflares have not been as thoroughly studied as asteroid impact hazards or Earth-based natural catastrophes [29]. ChipSat swarms could provide valuable scientific information to better understand the nature of the magnetosphere, and to predict and mitigate the risk impact of space weather events.

Ionospheric anomalies including the ones caused by space weather and solar wind can affect RF communication, limiting the accuracy of navigation signals for air-traffic control, military, and emergency services. Space weather observation could exploit the capability of distributed data collection, to characterize areas of depleted density in ionospheric plasma, which can cause deflection of communication signals [30]. ChipSats in LEO can

also monitor ionospheric phenomena like auroras which result from the interaction between solar wind and the magnetosphere. The Earth's magnetic field is also affected by natural events such as tectonic plate movements, earthquakes, and volcanic activity. The ionospheric anomalies registered prior to these events could potentially be used to study the correlation between seismicity and geomagnetic storms [31].

Long-term changes in the magnetosphere have been correlated with climate change, however thermal variations in the ionosphere are not uniform across its layers, nor across the globe, and therefore multiple data points from different locations would be a valuable asset to study these effects over time [26]. Swarm formations can also serve as complementary methods for measuring ocean flow, as moving sea-water produces its own magnetic field, the signature of which can be detected at LEO altitudes. Ocean-climate models can be derived from the magnetic signal sensed, by determining the depth-integrated velocity of ocean water circulation, even in regions covered by ice. Magnetic ocean flow observations at satellite altitude can be compared to existing simulated solar/lunar tide models to correct inaccuracies [10].

Technological evolution in the space industry has led to an increased demand for component testing in space environment which can be challenging due to scarce flight opportunities and the consequential increase in development cost. However, ChipSats may provide a feasible platform for testing small components designed for pico- or nanosatellites in space. Because of the small size and low mass of these satellites launch opportunities might be easier to secure. The component could be quickly iterated for testing, and launched on multiple ChipSats to obtain rapid, statistical data for a fraction of the development cost [30].

The swarm missions described require hundreds of miniature satellites orbiting Earth. These small objects may constitute a real space debris hazard and their end-of-life phase should be planned carefully. Existing simulations for the dynamics of space debris rely on atmospheric density approximations and on aerodynamic characteristics like the ballistic coefficient, which measures a body's ability to overcome air resistance during flight. ChipSats have an extremely low ballistic coefficient and are expected to remain in LEOs for only a few days before re-entering and burning up in the atmosphere, minimizing the risk of becoming space debris [7]. Additionally, ChipSats could be used to determine the ballistic coefficient under various atmospheric densities contributing to more precise space debris simulations. Measurements at different points in time at various atmospheric densities would add to the precision of orbital decay simulations.

2.3 Guidance and Relative Navigation

Relative positioning and attitude determination are key features for formation flight. For two given satellites within a formation, the motion of the follower relative to the leader is determined by a set of six parameters representing the translational and rotational degrees of freedom (DOF). The leader satellite can be deemed “cooperative” if it is able to provide the follower with relative position and attitude information. When considering a swarm formation with multiple satellites operating in close proximity, the need for autonomy is motived by the fact that communication delays and loss of signal make relative navigation maneuvers based on ground station commands impractical [32]. The navigation system generally consists of a filter that processes the information inputs obtained from different sensors. The purpose of a filtering scheme is to reduce the noise from transmission signals in order to obtain an estimate of the state with minimal error. The guidance system must provide the desired state vector, at each point in time, which will be correlated with the estimated state, provided by the navigation system. The guidance function generates the relative position and velocity profiles for closed-loop controlled trajectories and determines the execution time and duration of maneuvers, enabling the controller to generate the required commands to correct the deviations between guidance and navigation states [33].

The PRISMA mission demonstrated that RF metrology can be exploited to obtain full position and attitude determination from a relative distance of several kilometers down to contact, by using a S-band intersatellite link (ISL) to provide GPS pseudorange and visual-based measurements. The primary navigation solution used in this mission is GPS-based. This requires the inclusion of GNSS receivers and antennas on board the leader and the follower, as well as a reliable communication link between the two satellites to exchange measurements. This technology can be used to obtain relative position measurements through differential GPS or carrier phase differential GPS approaches. When the receivers on both satellites target the same set of GPS satellites, the states coming from the filter will be correlated making use of the relative GPS properties. Then, an orbit guidance function takes as input the position and velocity for a relative trajectory. For the PRISMA formation, a feedback orbit control function was used, taking as input up to seven planning relative position coordinates, times, and control boxes, optimizing upcoming control requests based on propagation over the planning points [13]. The secondary navigation solution designed for this mission is a line of sight navigation filter, based on an extended Kalman filter, which estimates the trajectory of the follower relative to the leader using line of sight measurements from the optical sensors, and the spacecraft

attitude using accelerometer measurements [16]. The visual-based navigation sensor installed on the follower includes two cameras based on star-tracker technology. One far range camera for homing and rendezvous maneuvers to estimate the relative distance of the leader from up to 100 km, and another for proximity operations, capable of detecting LED patterns and the geometry of the leader, to estimate both relative distance and relative attitude [12].

The CanX-4&5 mission followed the same approach to GPS-based navigation, using an S-band radio ISL for communication between the two satellites. Three distinct pieces of GNC software were used to meet the formation control requirements. The navigation algorithm onboard, RealNav, is an extended Kalman filter that estimates the position and velocity of the follower relative to the leader by processing pseudorange and carrier phase measurements from commonly tracked GPS satellites. A separate algorithm, OASYS, performs the attitude determination using an extended Kalman filter which incorporates measurements from the magnetometer, sun sensors, rate gyro, and reaction wheel. FIONA, the formation control algorithm, is also an extended Kalman filter which provides coordinate transformations for mapping the relative state estimation and computes the relative trajectories of the satellites according to the control laws [34].

When considering a GNC system design for ChipSats, GPS-based navigation is the most promising approach. Since space-qualified GPS receivers are too heavy, representing approximately 30% of the maximum femtosatellite mass [35], COTS GPS modules are a suitable option from the accuracy point of view, but would require radiation hardening and a space-suitable software upgrade. The novel Monarch ChipSat protype [23] includes a GPS module and antenna, however, no further information on the hardware is provided on published literature. Thus, reliable lightweight GPS modules are considered a technology development area [11]. For the operation of the swarm, each ChipSat must estimate its own state and transmit this information to neighboring ChipSats in order to estimate the relative states required by the control algorithm. Given the short relative operation distances, the accuracy of the state information is crucial to achieve close-loop control. The reference ChipSat prototype [25] is equipped with a MEMS gyroscope and a 3-axial magnetometer providing measurements for attitude estimation. As an alternative to the Kalman filter, the explicit complementary filter is used to compare the Earth's magnetic field vector, measured in the satellite's frame by the onboard magnetometer, with the Earth's magnetic field vector estimation via rotation transformation, and calculate the attitude error. The attitude is described in quaternion form. The gyroscope measures the angular rate of the satellite providing feedforward control to improve the bandwidth of attitude determination.

2.4 Formation Flying Control

The swarm can be controlled using a centralized or decentralized approach. A centralized approach implies a “chief” satellite leading the formation, while the remaining satellites monitor its motion and correct their own relative trajectories accordingly, demonstrated in figure 2.4. This approach may be inadequate for large swarms due to limited tracking range and limited communication links. Additionally, if the mother flies out of range or suffers critical system failure, the formation is compromised. In a decentralized approach, shown in figure 2.5, each unit controls its own relative motion, based on motion information from neighboring satellites, in order to avoid communication overload.

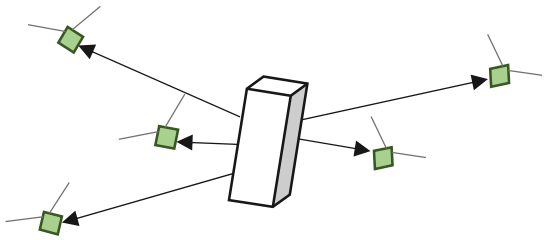

Figure 2.4: Centralized swarm

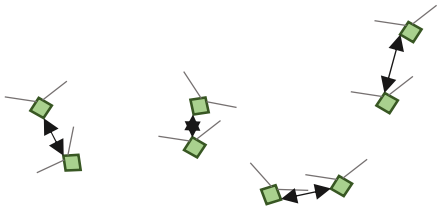

Figure 2.5: Decentralized swarm

When designing a flying formation mission, autonomous relative motion control is necessary to maintain spatial configuration, maneuver to a desired relative orbit and to correct naturally occurring relative drift. The common approach is the application of a 3-axis onboard propulsion system, allowing unrestricted thrust direction. In the case of the PRISMA mission [12], three distinct propulsion system were included on the follower satellite, consisting of a nominal Hydrazine propulsion system with six thrusters that provides torque-free translational capability, an experimental cold gas environmentally friendly propulsion system with two thrusters, and an additional experimental micro propulsion system based on MEMS-technology tested as a potential candidate for future missions where extremely low and accurate thrust is requested. For the CanX-4&5 mission [34], a cold gas propulsion system was used, equipped with four thrusters, and fueled with a liquid sulfur hexafluoride propellant. If the number of thrusters is limited, and thrust direction cannot be arbitrarily changed, a single-input control approach is also feasible, assuming the thrust vector is fixed to the body reference frame. As demonstrated in article [36], if a satellite is equipped with a passive magnetic attitude control system stabilizing the longitudinal axis along the local geomagnetic field, a single-input control system is able to achieve bounded relative trajectories with two satellites in near circular orbit, depending on orbital parameters and initial conditions. Passive magnetic control systems were particularly popular in the first decades of space exploration due to its simplicity, some are still used today on different small satellites. These systems rely on permanent

magnets to stabilize the satellite along the local geomagnetic induction vector and hysteresis rods, made from a magnetically soft material, to provide angular velocity damping [37]. Despite its low pointing accuracy, these systems are reliable for passive magnetic control and do not require power consumption.

Since miniaturized satellites pose unavoidable constraints on size, mass and energy sources, conventional propulsion systems are not used for control application. Alternative approaches have been proposed in recent years to develop effective, self-sufficient methods for motion control, requiring no propellant consumption, such as aerodynamic drag force and solar radiation pressure. Yet both methods require either solar sails onboard or specific form-factors with high area-to-mass ratios [38–40]. Conventional propulsion systems require continuous fuel expenditure to maintain formation geometry. If a satellites' fuel reserves are depleted its functionality will be compromised. Additionally, the risk of thruster plumes destabilizing the trajectories of neighbor spacecrafts, or blinding optical and/or thermal sensors onboard, makes fuel-dependent propulsion undesirable for smaller formations.

An article from MIT's Space System Laboratory [41] proposes the use of electromagnetic force between spacecrafts to control and maintain relative separation, relative attitude, and inertial rotation, which are critical maneuvers for formation flying. This can be achieved using high-power superconducting coils, coupled with reaction wheels for enhanced attitude control. The electrical current needed to generate the magnetic field is converted from solar radiation. Further studies on electromagnetic control [42,43], address the performance of electromagnetic force in LEO with an adaptative control approach to nonlinear relative translational motion and attitude dynamics. For an arbitrary N-satellite formation [42], a hybrid system is proposed with centralized translational control and decentralized attitude control. Alterations in one of the satellite's dipole causes actuation effects on all other satellites in the formation. Electromagnetic interactions generate torque, which inevitably leads to increasing angular momentum that can only be reduced by attitude actuators, such as reaction wheels, that can become saturated and lose control capability. Moreover, operation of electromagnetic formations in LEO is complicated by the fact that Earth has a strong magnetic field, which must be considered. Angular momentum control algorithms have been proposed to solve this issue [44,45]. It has been demonstrated that adjusting alternating magnetic dipole solutions to the constant geomagnetic field, effectively reduces satellite angular momentum, however this approach neglects accurate trajectory control. One possible solution, proposed in article [42] is to establish a formation of N-satellites with N-1 dipole interactions, leaving one available dipole that can be used to minimize angular momentum build-up on the

reaction wheels of each satellite. The force acting between pairs is the product of the individual values, but the torque caused by the external magnetic fields on each satellite is inverted if the polarity of the dipole is switched. Therefore, switching the polarity of all dipoles in the formation results in a net cancellation of the effect of the Earth's geomagnetic field, whilst internal forces and torques are maintained.

Considering the electromagnetic capability of the proposed ChipSat prototypes, decentralized translational motion control of a swarm can be achieved by modulating the interaction force between the magnetorquers on each spacecraft in order to prevent relative separation in the presence of disturbances. A swarm formation does not require specific spatial distribution; thus satellites can move along arbitrary trajectories using the electromagnetic interaction force to reduce relative separation in order to achieve and maintain a compact formation. Although, since it is impractical to include reaction wheels or any other actuator on board, a feasible attitude control solution must be devised. Excessive angular velocity will arise from the torque produced by dipole interactions and from the effect of the geomagnetic field on the magnetorquers, therefore, angular velocity damping is an essential process for stabilizing the ChipSat attitude. A straightforward approach is to use the classic feedback law [46], which can be implemented through the interaction between the magnetic moment generated by the magnetorquers and the Earth's magnetic field. This type of control stabilizes the satellite with specific relations between the control gains, providing asymptotical angular velocity damping.

2.5 Decentralized Electromagnetic Swarm Control

This dissertation proposes an autonomous relative translational motion and attitude control algorithm for a swarm operating in LEO, composed of 3.3 x 3.3 x 0.5 cm ChipSats with a mass of 10g, equivalent to the prototype proposed in article [25], and considering the same method of deployment as used for the Kicksat-2 mission [7]. The custom miniature magnetorquers are the sole actuators and due to its limited magnetic moment, the dipole interaction force is also limited. The swarm requires extremely short operating distances between satellites for active translational control. This limitation is considered and the constraints on initial conditions after deployment are analyzed as well. The state vector of each satellite is required for control calculation. Assuming each satellite is provided the relative motion information of satellites in close proximity through the onboard navigation system, the decentralized control algorithm is applied to eliminate relative drift and to achieve bounded relative trajectories. Due to the limited area of communication and effective range for the magnetic force application, the construction and maintenance of the swarm is achieved by periodically linking nearby satellites in interchangeable pairs based on relative motion information. The calculated dipole

interaction force is applied when control is necessary, disturbances and perturbing forces acting on nearby units are considered. When relative drift elimination is not required, the magnetic dipole of an unpaired ChipSat is used to provide asymptotical angular velocity damping. The proposed control algorithm was based on mathematical deductions presented in Chapter 3, and its performance was studied numerically through simulations performed with MATLAB.

Chapter 3

Orbital Dynamics

In this chapter, the fundamental orbital dynamics of the formation flying problem are reviewed. The information given is provided in more detail in [47], and in [48].

After deployment, satellites move along unbounded relative trajectories and the distance between them gradually increases in the absence of control, causing the swarm to degrade over time. The free-motion relative trajectory projections on the orbital plane are represented by elliptical spirals. Therefore, a straightforward approach to swarm distribution is to monitor and control the relative position of the instant centers of the ellipses. The Keplerian orbital parameters are used to represent the size, shape, and orientation of elliptical orbits, in 6-DOF:

$$[a, e, i, \Omega, \omega, \theta] \tag{3.1}$$

The semi-major axis (a) is used to describe the size of the elliptical orbit and eccentricity (e) is used to describe its shape, where $e=0$ implies a circular orbit. The orientation of the ellipse in the inertial reference frame is defined by three parameters. Inclination (i) is defined by the angle between the orbital plane and reference plane. The longitude of the ascending node (Ω) is the angle between the direction of the vernal equinox and the ascending node, in the reference plane, and the argument of periapsis (ω) is the angle in the orbital plane, between the ascending node and the perigee. Finally, the true anomaly (θ) is the angle that defines the position of the orbiting body along the ellipse at a specific time. Figure 2.1 illustrates the orbital representation of these parameters. Mean motion (n), which measures the average angular rate of a Keplerian orbit, is given by the equation:

$$n = \sqrt{\frac{\mu}{a^3}} = \frac{2\pi}{T} \tag{3.2}$$

where μ is Earth's standard gravitational parameter and T is the unperturbed orbital period. Since the mass of the Earth is much greater than the mass of the satellite the mass of the satellite can be neglected and the center of mass of the system is considered coincident with the position of the Earth's center of mass. It is assumed both bodies are represented as point masses and the only force acting on the system is the gravitational attraction between them.

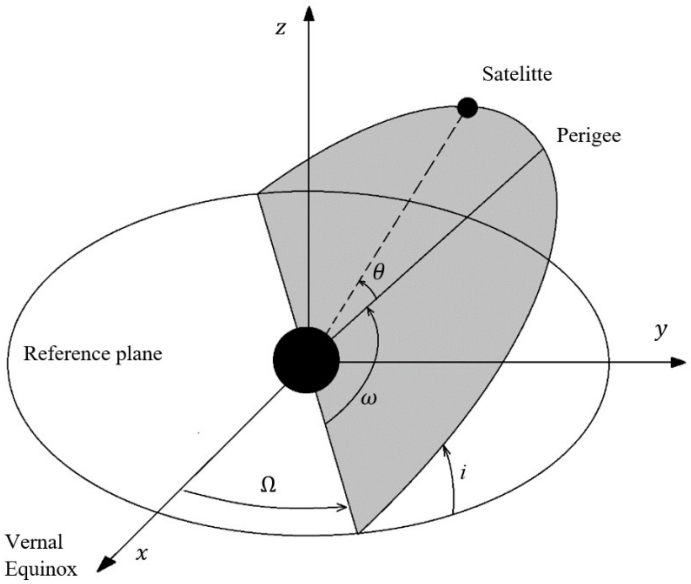

Figure 3.1: Keplerian orbital parameters

3.1 Reference Frames

A brief description of the reference frames and conversions between them is presented in this section. The Earth-Centered Inertial (ECI) reference frame is a non-rotating non-accelerating frame suited to describe Earth-bound orbital trajectories. The origin of the coordinate system is located at Earth's center of mass, with the X-axis pointing towards the vernal equinox, the Z-axis coincident with the Celestial Ephemeris Pole (CEP), Earth's axis of rotation, and the Y-axis lies in the equatorial plane, completing the right-handed orthogonal frame. The state vectors of a given satellite in the ECI frame are expressed as

$$\boldsymbol{X}_i = [X, Y, Z, \dot{X}, \dot{Y}, \dot{Z}]^T, i = 1, \dots, N \tag{3.3}$$

where N is the number of satellites in the swarm. The Keplerian orbital parameters are converted to state vectors in the ECI frame. For formation flying applications, the relative position and velocity of a follower relative to a leader are expressed in the Hill frame, a Local-Vertical Local-Horizontal (LVLH) rotating reference frame. Its origin is located at a reference point moving along a circular orbit at an orbital angular velocity equal to the mean motion n. The z-axis points towards the radial direction, the y-axis is aligned with orbital momentum and the x-axis completes the right-handed orthogonal frame. The relative state vectors are expressed in this frame as

$$\boldsymbol{x}_{ij} = \boldsymbol{x}_j - \boldsymbol{x}_i = [x, y, z, \dot{x}, \dot{y}, \dot{z}]^T, i = 1, \dots, N \text{ and } j = 1, \dots, N \tag{3.4}$$

Figure 2.2 represents the Hill frame relative to the ECI reference frame. The body reference frame is established to describe attitude of each satellite and has its origin located at the center of mass of the satellite. The axes are chosen to coincide with the principal axis of inertia. Attitude is described in quaternions.

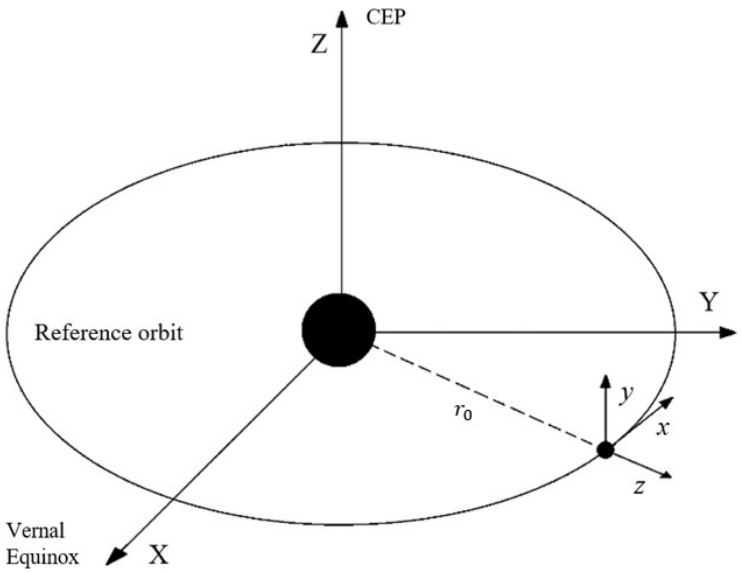

Figure 3.2: ECI and Hill reference frames

3.2 Reference Frame Conversions

The study of orbital dynamics and relative motion implies mathematical calculations, expressed in the different reference frames described above. The initial reference orbit of the swarm is designed using the Keplerian parameters, the initial state vectors of the satellites are then propagated in the ECI frame. The control laws are applied to the relative state vectors propagated in the LVLH frame, moving along the reference orbit. As a result, methods for transformation of vector components from one frame to another are frequently used throughout the simulation of the control algorithm.

3.2.1 Keplerian Parameters to ECI State Vectors

In order to convert the initial parameters in (3.1) into state initial state vector in (3.3) the semi-latus rectum p and the mean anomaly M must first be calculated with the following equations [49]:

$$p = a(1 - e^2) \tag{3.5}$$

$$M = \sqrt{\frac{\mu}{a^3}}(t - \tau) \tag{3.6}$$

where t is the current time and τ is the time of passage at the periapsis. Secondly, the eccentric anomaly E is calculated according to

$$E - e \sin E = M \tag{3.7}$$

which is a numerically solvable equation and E can be obtained through iterative calculation. For the initial iteration, a circular orbit $e=0$ is considered and $E1= M$, then Eq. (3.7) can be re-written according to Newton's method, which yields:

$$E_{n+1} = E_n - \frac{E_n - e \sin E_n - M}{1 - e \cos E_n} \tag{3.8}$$

Once the eccentric anomaly E is obtained, the following parameter can be calculated by the expressions below:

$$b = \left(\frac{a}{p}\right)^{1/2} \tag{3.9}$$

$$\cos\theta = \frac{\cos E - e}{1 - e \cos E} \tag{3.10}$$

$$\sin\theta = (1 - e^2)^{1/2} \frac{\sin E}{1 - e \cos E} \tag{3.11}$$

$$v_r = \left(\frac{\mu}{p}\right)^{1/2} e \sin\theta \tag{3.12}$$

$$v_n = \left(\frac{\mu}{p}\right)^{1/2} (1 + e \cos\theta) \tag{3.13}$$

$$\boldsymbol{R}_0 = \begin{bmatrix} a(\cos E - e) \\ b \sin E \\ 0 \end{bmatrix} \tag{3.14}$$

$$\boldsymbol{V}_0 = \begin{bmatrix} v_r \cos\theta - v_n \sin\theta \\ v_r \sin\theta + v_n \cos\theta \\ 0 \end{bmatrix} \tag{3.15}$$

where $\mu=3.986 \times 10^{14}\ m^3/s^2$ is Earth's standard gravitational parameter. The vectors $\boldsymbol{R}_0$ and $\boldsymbol{V}_0$ are the initial position and velocity vectors, respectively, in the reference orbital plane. v_r and v_n are the radial and normal components used to obtain the velocity vector. To describe the transformation of position and velocity vector components relative to the ECI frame, transformation matrices are utilized to rotate the sets of coordinates about the x-, y- and z-axis according to the angles Ω, i and ω, respectively,

$$\boldsymbol{A}_1 = \begin{bmatrix} \cos\Omega & \sin\Omega & 0 \\ -\sin\Omega & \cos\Omega & 0 \\ 0 & 0 & 1 \end{bmatrix} \tag{3.16}$$

$$\boldsymbol{A}_2 = \begin{bmatrix} 1 & 0 & 0 \\ 0 & \cos i & \sin i \\ 0 & -\sin i & \cos i \end{bmatrix} \tag{3.17}$$

$$\boldsymbol{A}_3 = \begin{bmatrix} \cos\omega & \sin\omega & 0 \\ -\sin\omega & \cos\omega & 0 \\ 0 & 0 & 1 \end{bmatrix} \tag{3.18}$$

the initial state vectors for the first satellite (leader) in the inertial frame are given by,

$$\boldsymbol{R}_i = [\,\boldsymbol{A}_1 \cdot \boldsymbol{A}_2 \cdot \boldsymbol{A}_3\,]^T\,\boldsymbol{R}_0 \tag{3.20}$$

$$\boldsymbol{V}_i = [\,\boldsymbol{A}_1 \cdot \boldsymbol{A}_2 \cdot \boldsymbol{A}_3\,]^T\,\boldsymbol{V}_0 \tag{3.19}$$

$$\boldsymbol{X}_i = [\boldsymbol{R}_i, \boldsymbol{V}_i]^T = [X, Y, Z, \dot{X}, \dot{Y}, \dot{Z}]^T \quad i = 1, \dots, N \tag{3.21}$$

$$\dot{\boldsymbol{R}}_i = \boldsymbol{V}_i \tag{3.22}$$

The MATLAB script for this for this function is provided in Appendix B.2.

3.2.2 ECI to Hill Frame

To obtain the relative state vectors required for the control calculations it is necessary to convert the inertial state of the leader-follower configuration to the rotating Hill reference frame (LVLH) whose axes are calculated according to the expressions below:

$$\boldsymbol{z} = \frac{\boldsymbol{R}_i}{\|\boldsymbol{R}_i\|} \qquad \boldsymbol{y} = \frac{\boldsymbol{R}_i \times \boldsymbol{V}_i}{\|\boldsymbol{R}_i \times \boldsymbol{V}_i\|} \qquad \boldsymbol{x} = \boldsymbol{y} \times \boldsymbol{z} \tag{3.23}$$

$$\boldsymbol{A} = [\,\boldsymbol{x}, \boldsymbol{y}, \boldsymbol{z}\,]^T \tag{3.24}$$

$$\boldsymbol{\omega} = \frac{\boldsymbol{R}_i \times \boldsymbol{V}_i}{\|\boldsymbol{R}_i\|^2} \tag{3.25}$$

where $\boldsymbol{A}$ is the rotation matrix from the ECI to the Hill reference frame and $\boldsymbol{\omega}$ expresses the orbital angular velocity directed towards the orbital kinetic momentum and therefore perpendicular to the reference orbit. The relative state vectors are defined as follows:

$$\boldsymbol{x}_{ij} = \left[\boldsymbol{A}(\boldsymbol{R}_j - \boldsymbol{R}_i), \boldsymbol{A}(\boldsymbol{V}_j - \boldsymbol{V}_i) - \boldsymbol{A}\left(\boldsymbol{\omega} \times (\boldsymbol{R}_j - \boldsymbol{R}_i)\right)\right]^T = \tag{3.26}$$

$$= \left[\boldsymbol{r}_{ij}, \boldsymbol{v}_{ij}\right]^T =$$

$$= \left[x_{ij}, y_{ij}, z_{ij}, \dot{x}_{ij}, \dot{y}_{ij}, \dot{z}_{ij}\right]^T, i \neq j, \;\; i = 1, \dots, N, j = 1, \dots, N$$

The MATLAB script for this function is included in Appendix B.3.

3.3 Two-Body Problem

Considering the two-body problem as the basis for designing a swarm, from Newton's gravitational laws it is possible to obtain the homogeneous second order differential equation for a single satellite experiencing gravitational forces. Let $\boldsymbol{R}_i$ and $\boldsymbol{R}_j$ be the position vectors of two bodies defined by their centers of mass, and m_i and m_j their respective masses, expressed in the inertial frame, and let $\boldsymbol{r}_c$ be the position of the center of mass of the two bodies, and let $\boldsymbol{R}_{ij}$ be the position vector of m_j relative to m_i , so that $\boldsymbol{R}_{ij} = \boldsymbol{R}_j - \boldsymbol{R}_i$.

$$\boldsymbol{r}_c = \frac{m_i \boldsymbol{R}_i + m_j \boldsymbol{R}_j}{m_i + m_j} \tag{3.27}$$

The attraction force exerted on m_i by m_j which acts along the line joining the two centers of mass is given by Newton's second law of universal gravitation:

$$\boldsymbol{F}_{ij} = \frac{G m_i m_j}{{R_{ij}}^2} \left(\frac{\boldsymbol{R}_{ij}}{R_{ij}} \right) \tag{3.28}$$

where G is the gravitational constant and $R_{ij} = ||\boldsymbol{R}_{ij}||$. According to Newton's third law, the force exerted on m_j by m_i is $\boldsymbol{F}_{ji} = -\boldsymbol{F}_{ij}$. Applying Newton's second law of motion results in

$$\boldsymbol{F}_{ij} = m_i \ddot{\boldsymbol{R}}_i \tag{3.29}$$

$$\boldsymbol{F}_{ji} = m_j \ddot{\boldsymbol{R}}_j \tag{3.30}$$

$$m_i \ddot{\boldsymbol{R}}_i + m_j \ddot{\boldsymbol{R}}_j = 0 \tag{3.31}$$

where $\ddot{\boldsymbol{R}}_i$ and $\ddot{\boldsymbol{R}}_j$ is the absolute acceleration of m_i and m_j, respectively, in the ECI frame.

Since $m_i + m_j \neq 0$, the acceleration of the center of mass of the two-body system is constant and equal to zero. From the second derivative of the relative position vector we can then obtain the equation of motion for the two-body system:

$$\ddot{\boldsymbol{R}}_{ij} = \ddot{\boldsymbol{R}}_j - \ddot{\boldsymbol{R}}_i \tag{3.32}$$

$$\ddot{\boldsymbol{R}}_{ij} = -\frac{G(m_i + m_j)}{{R_{ij}}^2} \left(\frac{\boldsymbol{R}_{ij}}{R_{ij}} \right)$$

$$\ddot{\boldsymbol{R}}_{ij} + \frac{\mu}{{R_{ij}}^3} \boldsymbol{R}_{ij} = 0 \tag{3.33}$$

The vector equation (3.33) is equivalent to three scalar equations from which it is possible to obtain the six integration constants that correspond to the initial state vector of a satellite. The solution to this equation can be obtained by calculating the first derivative of the angular momentum per unit mass in Eq. (3.34):

$$\boldsymbol{h} = \boldsymbol{r} \times \dot{\boldsymbol{r}} \tag{3.34}$$

$$\boldsymbol{R}_{ij} \times \left(\frac{d^2 \boldsymbol{R}_{ij}}{t^2} + \frac{\mu}{{R_{ij}}^3} \boldsymbol{R}_{ij} \right) = 0 \tag{3.35}$$

$$\boldsymbol{R}_{ij} \times \frac{d^2 R_{ij}}{t^2} = 0 \text{ , since } \boldsymbol{R}_{ij} \times \boldsymbol{R}_{ij} = 0$$

$$\frac{d}{dt}\left(\boldsymbol{R}_{ij} \times \frac{d\boldsymbol{R}_{ij}}{dt} \right) = \left(\frac{d\boldsymbol{R}_{ij}}{dt} \times \frac{d\boldsymbol{R}_{ij}}{dt} \right) + \boldsymbol{R}_{ij} \times \frac{d^2 \boldsymbol{R}_{ij}}{dt^2} = \boldsymbol{R}_{ij} \times \frac{d^2 \boldsymbol{R}_{ij}}{dt^2} = 0$$

$$\frac{d}{dt}(\boldsymbol{h}) = \frac{d}{dt}\left(\boldsymbol{R}_{ij} \times \frac{d\boldsymbol{R}_{ij}}{dt} \right) = 0 \tag{3.36}$$

The first derivative of Eq. (3.34), simplified in Eq. (3.35), confirms that the angular momentum is a constant vector and normal to the reference orbit, therefore the angular momentum is conserved in a two-body system.

3.4 Hill-Clohessy-Wiltshire Equations

The Hill-Clohessy-Wiltshire (HCW) equations [50] are a linear approximation of the relative motion of two arbitrarily chosen satellites within the swarm, in a leader-follower configuration expressed in the rotating Hill reference frame. The linearized ordinary differential equations of free motion have constant coefficients and can be solved analytically; the general solution is the sum of the solution to the homogeneous system, that depends on initial conditions, and the particular solution representing the effects of the applied forces, where electromagnetic control is later included. The equations are valid for small intersatellite separation, therefore the distance between a leader and a follower must be of much smaller order than the orbital radius of the leader. The accuracy of the HCW equations is limited by a number of simplifying assumptions made during their derivation, by utilizing the two-body gravitational equation of motion with no perturbations and assuming the leader is in a circular orbit. The linearization of the equations of relative motion (HCW) can be found in Appendix A.1.

Let $\boldsymbol{r}_i = [x_i, y_i, z_i]$ and $\boldsymbol{r}_j = [x_j, y_j, z_j]$ be the position vectors of the i-th to the j-th satellite, with $i = 1, \dots, N, j = 1, \dots, N, i \neq j$. The relative motion vector of the follower relative to the leader is $\boldsymbol{r}_{ij} = \boldsymbol{r}_j - \boldsymbol{r}_i = [x_{ij}, y_{ij}, z_{ij}]$, the free motion HCW equations are derived:

$$\ddot{x}_{ij} + 2\omega\dot{z}_{ij} = 0 \tag{3.37}$$

$$\ddot{y}_{ij} + \omega^2 y_{ij} = 0 \tag{3.38}$$

$$\ddot{z}_{ij} - 2\omega\dot{x}_{ij} - 3\omega^2 z_{ij} = 0 \tag{3.39}$$

The solutions to the Eqs. (3.37-3.39), provided in [38], is:

$$x_{ij}(t) = -3{C_1}^{ij}\,\omega t + 2{C_2}^{ij}\cos(\omega t) - 2{C_3}^{ij}\sin(\omega t) + {C_4}^{ij} \tag{3.40}$$

$$y_{ij}(t) = {C_5}^{ij}\sin(\omega t) + {C_6}^{ij}\cos(\omega t) \tag{3.41}$$

$$z_{ij}(t) = 2{C_1}^{ij} + {C_2}^{ij}\sin(\omega t) + {C_3}^{ij}\cos(\omega t) \tag{3.42}$$

where $C_1, \ldots, C_6$ are constant coefficients that provide a particular solution given the initial conditions x_o, y_o, z_o, $\dot{x}_o$, $\dot{y}_o$, $\dot{z}_o$ at $t = o$:

$$\begin{aligned} {C_1}^{ij} &= \frac{\dot{x}_{ij}(0)}{\omega} + 2z(0) \qquad {C_2}^{ij} = \frac{\dot{z}_{ij}(0)}{\omega} \qquad {C_3}^{ij} = -3z(0) - \frac{2\dot{x}_{ij}(0)}{\omega} \\ {C_4}^{ij} &= x(0) - \frac{\dot{z}_{ij}(0)}{\omega} \qquad {C_5}^{ij} = \frac{\dot{y}_{ij}(0)}{\omega} \qquad {C_6}^{ij} = y_{ij}(0) \end{aligned} \tag{3.43}$$

All periodic terms are at orbital frequency ω, equivalent to the frequency of revolution (mean motion, n) of the Hill frame. The term responsible for relative secular drift is $-3C_1\omega t$, in the along-track direction, growing linearly in time. The relative trajectory of two satellites is closed if $C_1 = o$. However, such ideal initial conditions for closed free motion almost never occur and drift will arise from either z_o or $\dot{x}_o$. Other perturbations and non-linear effects will cause additional relative drift. In order to eliminate drift and achieve bounded relative trajectories satellites must be controlled. The term C_4 is responsible for the displacement of the instant center of the ellipse in the along-track direction, referred to as relative shifts. The instant center of the ellipse can be obtained from Eq. (3.40) when the secular drift term equals zero. Relative shifts dictate the specific distribution of the satellites within the swarm. An example of a relative trajectory exhibiting drift is presented in Fig. 3.3. The MATLAB script used to calculate the trajectory of the satellites from Eqs. (3.37-3.39) is presented in Appendix B.4, and the C constants from Eqs. (3.43) are calculated using a function given in Appendix B.5.

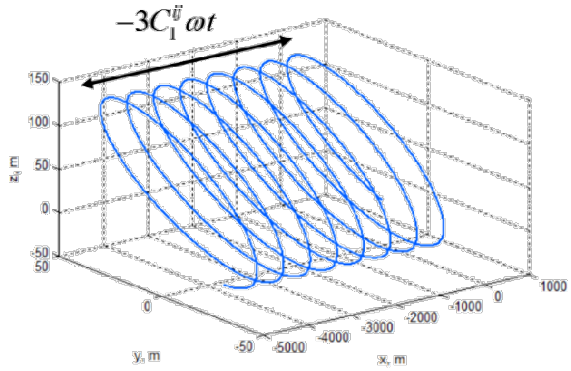

Figure 3.3: Trajectory demonstrating relative drift

3.5 Controlled Motion Equations

The electromagnetic force is considered for control of the swarm. This force originates from the interaction of the magnetic dipoles generated by the 3-axial orthogonal magnetorquers of each satellite in the swarm when active. Considering the leader-follower configuration for i and j satellites, the electromagnetic force acting on one of the satellites can be written as [44]:

$$\boldsymbol{F}_{ij} = \frac{3m_0}{4\pi}\left(\frac{\boldsymbol{m}_i \cdot \boldsymbol{m}_j}{{r_{ij}}^5}\boldsymbol{r}_{ij} + \frac{\boldsymbol{m}_i \cdot \boldsymbol{r}_{ij}}{{r_{ij}}^5}\boldsymbol{m}_j + \frac{\boldsymbol{m}_j \cdot \boldsymbol{r}_{ij}}{{r_{ij}}^5}\boldsymbol{m}_i - 5\frac{(\boldsymbol{m}_i \cdot \boldsymbol{r}_{ij})(\boldsymbol{m}_j \cdot \boldsymbol{r}_{ij})}{{r_{ij}}^7}\boldsymbol{r}_{ij}\right)$$
$$i = 1, \dots, N \quad j = 1, \dots, N \quad i \neq j \tag{3.43}$$

where $\boldsymbol{m}_i$ and $\boldsymbol{m}_j$ are the dipole vectors of the leader and follower respectively, $\boldsymbol{r}_{ij}$ is the relative position vector of the follower relative to the leader, $r_{ij} = ||\, \boldsymbol{r}_{ij} \,||$ and $m_0 = 4\pi \times 10^{-7}\ T\ m/A$ which is the vacuum permeability constant. The MATLAB script for the electromagnetic force calculation is given in Appendix B.8. Let the acceleration control vector be defined as

$$\boldsymbol{u}_{ij} = \boldsymbol{u}_j - \boldsymbol{u}_i = \left[u_x^{ij}, u_y^{ij}, u_z^{ij}\right] \tag{3.44}$$

$$u_y^{ij} = u_z^{ij} = 0 \tag{3.45}$$

with a single non-zero component in the along-track direction, defined as

$$u_x^{ij} = u_{ij} = f_{ij}/m \tag{3.46}$$

where m is the mass of the satellite. Applying this control vector to the HCW motion equations in Eqs. (3.37-3.39), from the i-th to the j-th satellites yields:

$$\ddot{x}_{ij} + 2\omega\dot{z}_{ij} = u_{ij} \tag{3.47}$$

$$\ddot{y}_{ij} + \omega^2 y_{ij} = 0 \tag{3.48}$$

$$\ddot{z}_{ij} - 2\omega\dot{x}_{ij} - 3\omega^2 z_{ij} = 0 \tag{3.49}$$

The full derivation of the controlled motion equations can be found in Appendix A.2. Assuming that for the time interval Δt the control (3.46) is constant. Then, the solution is:

$$x_{ij}(t) = -3{C_1}^{ij}\,\omega t + 2{C_2}^{ij}\,cos(\omega t) - 2{C_3}^{ij}\,sin(\omega t) + {C_4}^{ij} + \frac{4u_{ij}}{\omega^2} - \frac{3t^2 u_{ij}}{2} \tag{3.50}$$

$$y_{ij}(t) = {C_5}^{ij}\,sin(\omega t) + {C_6}^{ij}\,cos(\omega t) \tag{3.51}$$

$$z_{ij}(t) = 2{C_1}^{ij} + {C_2}^{ij}\,sin(\omega t) + {C_3}^{ij}\,cos(\omega t) + \frac{2tu_{ij}}{\omega} \tag{3.52}$$

The electromagnetic force has no effect on motion along the y-axis, which is defined only by initial conditions, consequently only the planar motion of the satellites in the x-z plane is considered.

3.6 Controlled Orbital Motion

The controlled orbital motion of each satellite is calculated in ECI reference frame. Because Earth is an ellipsoid with slightly flattened poles, the additional gravitational attraction around the equatorial plane causes orbital perturbations. Earth gravity harmonics are terms of the gravity potential series through which the deviations from a perfect sphere can be represented. The coefficient of the second harmonic J_2, the largest term of the zonal harmonics, is specifically related to the equatorial bulge resulting from the difference between the equatorial and polar radius of approximately 21 km, and its effect is considered in the gravitational force calculations. Perturbing forces such as higher-order harmonics, differential atmospheric drag or third body effects may also influence orbital motion but are not considered in this study. The second harmonic coefficient is $J_2 = 1082.8 \times 10^{-6}$ [51]. From the absolute position vector $\boldsymbol{R}_i = [X, Y, Z]$, in the ECI frame, the acceleration $\boldsymbol{a}_{J2}$ caused by the J_2 effect on a given satellite can be calculated through the expression:

$$\boldsymbol{a}_{j2} = \delta\frac{\boldsymbol{R}_i}{{R_i}^5}\left(\frac{5\times Z^2}{{R_i}^2} - 1\right) - \frac{2\delta}{{R_i}^5}\times[0,0,Z] \tag{3.53}$$

$$\delta = \frac{3}{2}{R_E}^2\mu \times 1082.8 \times 10^{-6} \tag{3.54}$$

where $R_E = 6.378 \times 10^6\ m$ is the equatorial radius of Earth and Z is the z-axis component of the absolute position vector. The acceleration $\boldsymbol{a}_{J2}$ can then be implemented into the force calculation:

$$\ddot{\boldsymbol{R}}_i = -\mu \frac{\boldsymbol{R}_i}{{R_i}^3} + \boldsymbol{a}_{j2} + \frac{\boldsymbol{F}_{ij}}{m} \tag{3.55}$$

$$i = 1, \dots, N \quad j = 1, \dots, N \quad i \neq j$$

where m the mass of each satellite. The force model used for the algorithm includes the gravitational attraction force considering the J_2 perturbation effect, as well as the electromagnetic force used for control. The aerodynamic force and radiation pressure effects are neglected. The MATLAB script of the force model is provided in Appendix B.10. To determine the electromagnetic force acting on the satellites the dipole vectors must first be calculated. Let the dipole vector of the leader and the follower be defined as

$$\boldsymbol{m}_i = \left[m_{ix}, m_{iy}, m_{iz}\right]^T \tag{3.56}$$

$$\boldsymbol{m}_j = \left[m_{jx}, m_{jy}, m_{jz}\right]^T \tag{3.57}$$

where $\boldsymbol{m}_i$ is the dipole of the leader and $\boldsymbol{m}_j$ is the dipole vector of the follower. Assume that the leader's dipole vector has a single non-zero component,

$$\boldsymbol{m}_i = [m_{ix}, 0, 0]^T \tag{3.58}$$

The components of the follower's dipole components m_{jx}, m_{jy}, m_{jz} can be obtained from the equation:

$$\boldsymbol{F}_{ij} - \boldsymbol{u}_{ij} = 0 \tag{3.59}$$

The simplified solution to the $\boldsymbol{m}_j$ vector components is determined with the MATLAB script provided in Appendix B.6, and yields:

$$m_{jx} = \frac{2\pi \cdot u_{ij} \cdot x_{ij}\left(-{x_{ij}}^2 + 4{y_{ij}}^2 + 4{z_{ij}}^2\right)\left({x_{ij}}^2 + {y_{ij}}^2 + {z_{ij}}^2\right)^{5/2}}{3m_0 \cdot m_{ix}\left(2{x_{ij}}^4 + 3{x_{ij}}^2 \cdot {y_{ij}}^2 + 3{x_{ij}}^2 \cdot {z_{ij}}^2 + {y_{ij}}^4 + 2{y_{ij}}^2 \cdot {z_{ij}}^2 + {z_{ij}}^4\right)} \tag{3.60}$$

$$m_{jy} = \frac{2\pi \cdot u_{ij} \cdot y_{ij}\left(-4{x_{ij}}^2 + {y_{ij}}^2 + {z_{ij}}^2\right)\left({x_{ij}}^2 + {y_{ij}}^2 + {z_{ij}}^2\right)^{5/2}}{3m_0 \cdot m_{ix}\left(2{x_{ij}}^4 + 3{x_{ij}}^2 \cdot {y_{ij}}^2 + 3{x_{ij}}^2 \cdot {z_{ij}}^2 + {y_{ij}}^4 + 2{y_{ij}}^2 \cdot {z_{ij}}^2 + {z_{ij}}^4\right)} \tag{3.61}$$

$$m_{jz} = \frac{2\pi \cdot u_{ij} \cdot z_{ij}\left(-4{x_{ij}}^2 + {y_{ij}}^2 + {z_{ij}}^2\right)\left({x_{ij}}^2 + {y_{ij}}^2 + {z_{ij}}^2\right)^{5/2}}{3m_0 \cdot m_{ix}\left(2{x_{ij}}^4 + 3{x_{ij}}^2 \cdot {y_{ij}}^2 + 3{x_{ij}}^2 \cdot {z_{ij}}^2 + {y_{ij}}^4 + 2{y_{ij}}^2 \cdot {z_{ij}}^2 + {z_{ij}}^4\right)} \tag{3.62}$$

For the algorithm, a specific function for real-time dipole calculation is constructed using the solution provided in Eqs. (3.60-3.62). The magnetic dipole moment of each satellite is calculated considering the relative position of the current pair. The interaction of two given dipoles results in the magnetic attraction/repulsion force used to control the relative trajectories of the ChipSats. The MATLAB script for this function is provided in Appendix B.7.

3.7 Controlled Angular Motion

In this section, rigid angular motion for each satellite is considered. Attitude control is obtained by applying the control torques generated by the magnetorquers, along the three orthogonal axes [52]. Its operation is based on the interaction between the magnetic dipole moment of each satellite and the Earth's magnetic field. When the relative motion control between satellites is inactive, the magnetorquers are utilized as actuators for angular velocity damping. Euler's equation for a rigid body with the inertia tensor $\boldsymbol{J}$ is:

$$\boldsymbol{J} \cdot \dot{\boldsymbol{\omega}} + \boldsymbol{\omega} \times (\boldsymbol{J} \cdot \boldsymbol{\omega}) = \boldsymbol{M} \tag{3.63}$$

where $\boldsymbol{\omega}$ is the angular velocity in the body-fixed reference frame and $\boldsymbol{M}$ is the sum of the torques acting on the satellite. Quaternions are used to describe satellite attitude, the kinematic relations in Euler's equations are the following:

$$\dot{\Lambda} = \frac{1}{2}\boldsymbol{C}\Lambda \tag{3.64}$$

$$\boldsymbol{C} = \begin{bmatrix} 0 & \omega_3 & -\omega_2 & \omega_1 \\ -\omega_3 & 0 & \omega_1 & \omega_2 \\ \omega_2 & -\omega_1 & 0 & \omega_3 \\ -\omega_1 & -\omega_2 & -\omega_3 & 0 \end{bmatrix} \tag{3.65}$$

where Λ is the quaternion and $\boldsymbol{C}$ is the derivation matrix containing the angular velocity vector components ω_1, ω_2, ω_3. The angular velocity and local geomagnetic field sensor measurements, necessary for the application of attitude control, can be obtained from the gyroscope and magnetometer onboard. For the simulations, let $\boldsymbol{m}_{geo}$ be the approximation of the geomagnetic dipole moment at the center of Earth pointing North, $\boldsymbol{m}_{geo} = [0, 0, -8^{-22}]$. The geomagnetic field acting on a given satellite can be calculated via the dipole model [42]:

$$\boldsymbol{B}_{geo} = \frac{m_0}{4\pi}\left(\frac{3\boldsymbol{R}_i(\boldsymbol{m}_{geo} \cdot \boldsymbol{R}_i)}{{R_i}^5} - \frac{\boldsymbol{m}_{geo}}{{R_i}^3}\right) \tag{3.66}$$

where $\boldsymbol{R}_i$ is the absolute position vector of a given satellite within the swarm, expressed in the ECI frame. The effect of magnetic fields generated by the magnetorquers of nearby satellites must also be considered and can be similarly calculated as follows [42]:

$$\boldsymbol{B}_j = \frac{m_0}{4\pi}\left(\frac{3\boldsymbol{r}_{ij}\left(\boldsymbol{m}_j \cdot \boldsymbol{r}_{ij}\right)}{{r_{ij}}^5} - \frac{\boldsymbol{m}_i}{{r_{ij}}^3}\right) \quad j = 1, \dots, N \tag{3.67}$$

where $\boldsymbol{r}_{ij}$ is the relative position vector, expressed in the Hill frame. Therefore, the total magnetic field is defined as:

$$\boldsymbol{B} = \boldsymbol{B}_j + \boldsymbol{B}_{geo} \quad j = 1, \dots, N \tag{3.68}$$

In order to reduce the satellite's kinematic moment the damping algorithm is applied. The magnetic moment for angular velocity damping can be calculated as:

$$\boldsymbol{m}_{damp} = \boldsymbol{\omega} \times \boldsymbol{B} \tag{3.69}$$

and the total sum of the torques acting on a given satellite is

$$\boldsymbol{M} = \left(\boldsymbol{m}_j + \boldsymbol{m}_{damp}\right) \times \boldsymbol{B} \tag{3.70}$$

The gravitational and aerodynamic torques, as well as the solar radiation pressure effect, are not considered in the attitude motion equations. The controlled angular motion equations and the control torque calculations are included in the force model of the algorithm, in Appendix B.10.

Chapter 4

Lyapunov-based Control Algorithm

The proposed decentralized algorithm is based on a set of operational rules to construct and maintain a compact swarm, by individually and independently controlling each satellite based on relative motion information. The control goal is to eliminate the relative drift between satellites. The shape and size of relative trajectories from Eqs. (3.37-3.39) are determined by the *C* values from Eq. (3.43). Henceforth, the constant values from the free relative motion in Eq. (3.43) are considered as varying at each time step, for the controlled motion Eqs. (3.47-3.49). From the motion equations (3.40-3.42) it is concluded that the C_1 constant is responsible for the drift. The following Lyapunov candidate function is constructed:

$$V = \frac{1}{2}(C_1^{ij})^2 \tag{3.71}$$

The conditions $V > 0$ and $V(0) = 0$ are satisfied. The derivative of the Lyapunov function along the system trajectories should be negative to satisfy the Barbashin-Krasovskii theorem [53] to achieve the global asymptotical stability. The derivative is the following:

$$\dot{V} = C_1^{ij}\dot{C}_1^{ij} = C_1^{ij}\left(\frac{\ddot{x}^{ij}}{\omega} + 2\dot{z}^{ij}\right) \tag{3.72}$$

Rearranging the expression, with the Lyapunov function as a definite negative function, yields:

$$\dot{V} = \frac{1}{\omega}C_1^{ij}(\ddot{x}^{ij} + 2\omega\dot{z}^{ij}) = C_1^{ij}\frac{1}{\omega}u_x = -\frac{k}{\omega}\left(C_1^{ij}\right)^2 \tag{3.73}$$

where $k > 0$. The resulting control law is

$$u^{ij} = -kC_1^{ij} \tag{3.74}$$

The control provides a convergence to closed relative trajectories. The calculated control is applied by the interchangeable pairing of two satellites and subsequent activation of its magnetorquers generating a magnetic attraction or repulsion force between them, actively eliminating relative drift between pairs, or avoiding collisions within the swarm. When orbital corrections are not necessary, the magnetic control is utilized for angular velocity

damping. Control is applied immediately after launch from random close coordinates, effectively constructing a stable swarm formation from the i-th to the j-th satellite and maintaining its integrity over the simulation period. The magnetorquers produce a limited maximum dipole moment, henceforth referred to as m_{max}. Consequently, each ChipSat can only operate within a limited range, outside of which the electromagnetic interaction force is negligible. Perturbating forces and torques caused by nearby pairs within operational distance are considered in the force calculations. It is assumed each ChipSat is capable of determining its own state and transmitting this information to nearby satellites in its communicational range. The operational rules and strategies described in this chapter are compiled in the source code of the swarm formation, provided in Appendix B.1.

4.1 Pairing Strategies

After deployment, the current state vector $\boldsymbol{X}_i$ of each ChipSat is determined. This information is then used to calculate relative state vectors $\boldsymbol{x}_{ij}$ and motion equation constants, including relative drift C_1, between every unit within communicational range. The primary objective when assembling and maintaining the swarm formation is to achieve bounded relative trajectories through relative drift elimination. Relative parameters are recalculated at the beginning of each time interval Δt, and the control force is applied until C_1 is approximately zero. The calculated control is applied simultaneously between paired satellites throughout the swarm; therefore, pair selection is an important step when considering a decentralized approach.

The main strategy employed is based on relative distance, meaning each i-th unit sorts all j-th satellites in its communicational range according to the relative distance,

$$r_{ij} = \sqrt{\left(x_{ij}\right)^2 + \left(y_{ij}\right)^2 + \left(z_{ij}\right)^2} \tag{3.75}$$

from itself and selects the nearest, if the calculated drift $C_1 > C_{min}$, where C_{min} is the defined minimum value for C_1 below which the relative drift between a pair is negligible, the pairing process is possible, otherwise the option is discarded, and the next satellite is considered. This strategy will be referred to as Pairing Method A. Alternatively, a similar strategy based on the calculated relative drift between possible pairs within communicational range was also studied. Firstly, an operational radius r_{c1_max} must be established inside the communication field to exclude satellites with excessively large relative distance. Each i-th unit sorts all j-th satellites, within the defined radius, selecting

the one with the largest C_1 calculated value, if $C_1 > C_{min}$ pairing is necessary. This strategy will be referred to as Pairing Method B.

4.2 Dipole Interaction

Once two considered satellites are successfully paired, $pair(i) = j$ and $pair(j) = i$ and their relative position vector $\boldsymbol{r}_{ij}$ is known, the magnetic dipole moment can be calculated. The magnetic dipoles are restricted to a maximum value m_{max}; thus the dipole vector of the leader is defined as $\boldsymbol{m}_i = [m_{max}, 0, 0]$ If the relative distance between the pair is larger than the minimum defined distance for dipole calculation, $r_{ij} > r_{min}$, the follower's dipole vector $\boldsymbol{m}_j$ can be obtained from Eqs. (3.60-3.62). If the maximum absolute value of the calculated dipole moment exceeds the maximum defined value, $max\{|m_{jx}|, |m_{jy}|, |m_{jz}|\}$, the dipole moment is recalculated as:

$$\boldsymbol{m}_j = \frac{\boldsymbol{m}_j}{\max\{|m_{jx}|, |m_{jy}|, |m_{jz}|\}} \cdot m_{max} \tag{3.76}$$

When the ChipSats are too close, the pairing option is rejected, and dipole calculations are not carried out in order to reduce collision risk and to avoid unnecessary application of the control force. Let r_{no_pair} be defined as the minimum distance between two satellites for dipole calculation. If $r_{min} < r_{no\_pair}$, $pair(i) = pair(j) = 0$, and the calculated dipole vectors are redefined as $\boldsymbol{m}_i = [0, 0, 0]$ and $\boldsymbol{m}_j = [0, 0, 0]$.

4.3 Collision Avoidance

The ChipSats in the swarm move along very close relative trajectories, therefore collisions between them are a substantial risk. As previously stated, dipole calculation is restricted to a minimum distance r_{no_pair} between two nearby satellites. Consider a smaller critical radius $r_{collision}$ around each satellite; if the trajectory of another satellites intersects this area, the control algorithm detects a collision risk. The control objective is to actively increase the relative distance between them through the polarity switch of the magnetorquers in order to generate a repulsive dipole interaction force. For any i-th and j-th satellites, with a relative distance $r_{ij} < r_{collision}$, the magnetic dipoles are calculated as follows:

$$\boldsymbol{m}_j = \frac{\boldsymbol{r}_{ij}}{r_{ij}} \cdot m_{collision} \tag{3.77}$$

$$\boldsymbol{m}_i = -\frac{\boldsymbol{r}_{ij}}{r_{ij}} \cdot m_{collision} \tag{3.78}$$

where $m_{collision}$ is the defined dipole value for collision avoidance. This type of control is applied continuously for as long as the ChipSat is within critical distance. If there is more than one satellite, the algorithm targets the nearest. During this process, relative drift temporarily increased, when a satellite is no longer at risk of collision, the control algorithm switches back to its default relative drift elimination mode.

Chapter 5

Numerical Study

Consider a swarm of the ChipSats deployed by a CubeSat in low Earth Orbit, each equipped with three orthogonal magnetorquers, capable of producing a magnetic dipole moment and not exceeding the maximum defined value. In case the magnetic dipole required for control exceeds this value, the maximum value is produced instead. The simulations of the proposed control algorithm are conducted using MATLAB. All the simulation parameters are listed in Table 5.1.

Table 5.1: Simulation parameters

Main swarm parameters	
Number of satellites in the swarm, N	20
Simulation time step, Δt	10 s
Initial conditions	
Initial relative drift, C_1	random([-0.1;0.1]) m
Initial relative position constants, C_2 - C_6	random([-0.1;0.1]) m
ChipSat parameters	
Mass of the ChipSat	0.01 kg
Inertia tensor, $\boldsymbol{J}$	$\mathrm{diag}\,(8\cdot10^{-7}, 8\cdot10^{-7}, 15\cdot10^{-7})\ \mathrm{kg\cdot m^2}$
Maximum magnetic dipole value of magnetorquers, m_{max}	0.01 Am^2
Orbital parameters	
Orbit altitude, a	500 000 m
Orbit inclination, i	51.7^o
Algorithm's parameters	
Minimum distance for dipole calculation, r_{min}	0.05 m
Maximum distance for the satellite pairing, rc_{1_max}	1 m
Distance for collision avoidance control application, $r_{collision}$	0.05 m
Magnetic dipole for collision avoidance, $r_{collision}$	0.0005 Am^2
Minimum distance between unpaired satellites for control application, r_{no_pair}	0.3 m
Minimum relative drift for pairing, C_{min}	0.01 m

5.1. Free Motion of the Swarm

The ChipSats are launched in random initial conditions in the vicinity of the origin of the Hill reference frame, the values and directions of the relative velocity vectors are arbitrary. Due to the random initial conditions after launch, relative motion is not bounded. Figure 5.1 shows an example of the free motion trajectories of twenty ChipSats. In the absence of control, relative drift causes separation between satellites and the formation will

eventually fly apart. Figure 5.2 shows the distance of each satellite relative to the first, which is gradually increasing over time. This separation between satellites is caused by relative drift, shown in Figure 5.3.

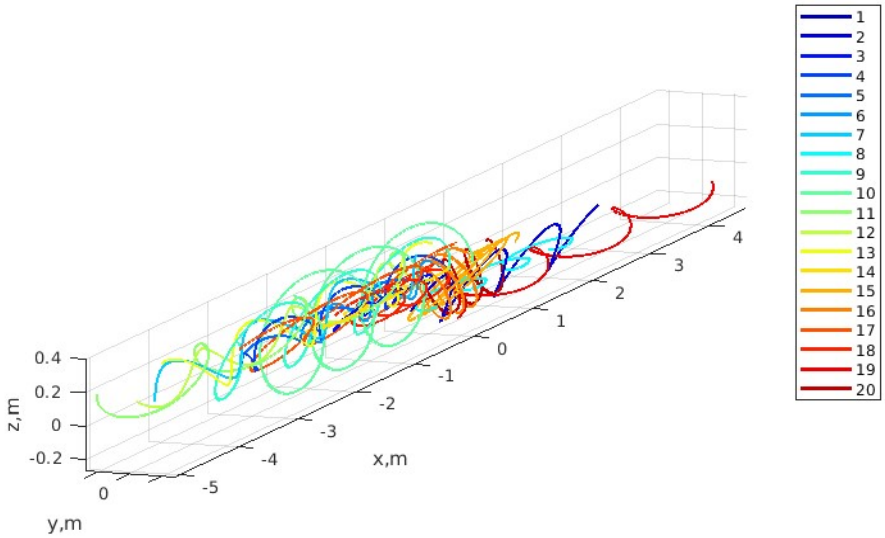

Figure 5.1: Relative free motion trajectories of the swarm

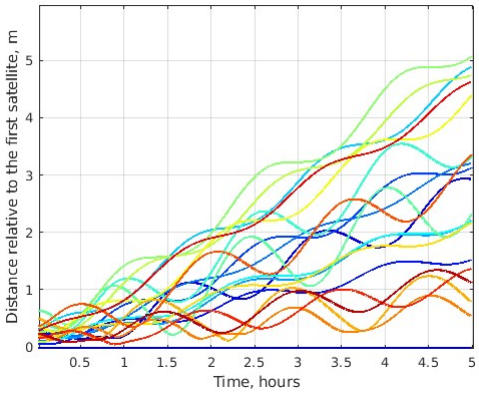

Figure 5.2: Distances relative to the first satellite in the swarm

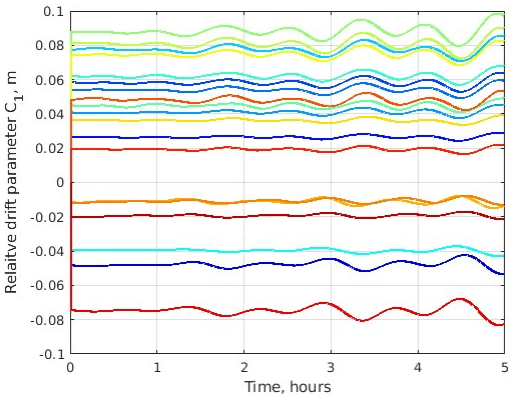

Figure 5.3: Relative drift during free motion

5.2. Controlled Motion Examples

5.2.1 Pairing Method A

Consider an application of the proposed control algorithm for the same initial conditions as described for the example of free relative motion. The results for pairing method A based on the nearest satellite with non-zero relative drift are first demonstrated in Figure 5.4. It can be observed that after the application of the control algorithm bounded relative trajectories are achieved, resulting in a significantly more compact formation. The results are further supported by the registered smaller distances between satellites, up to

approximately 1.5 *m* relative to the first satellite, as shown in Figure 5.5. The relative drift C_1 values, exhibited in Figure 5.6, converge to the vicinity of zero after 0.6 hours, meaning swarm stability is achieved. Subsequent peaks in relative drift values can be attributed to the collision avoidance control application. The temporary high relative drift values are rapidly decreased to the vicinity of zero by the default control application. Figure 5.7 demonstrates satellite pairing over the simulation period: the y-axis represents each satellite in the swarm and the assigned colors correspond to the satellite it is paired to at each time interval. The interchangeable pairing strategy enables relative drift elimination between all satellites in the swarm over time. After 1 hour, satellites are mostly not paired, and drift is eliminated. However, satellites will periodically pair to correct disturbances such as the ones caused by the collision avoidance control.

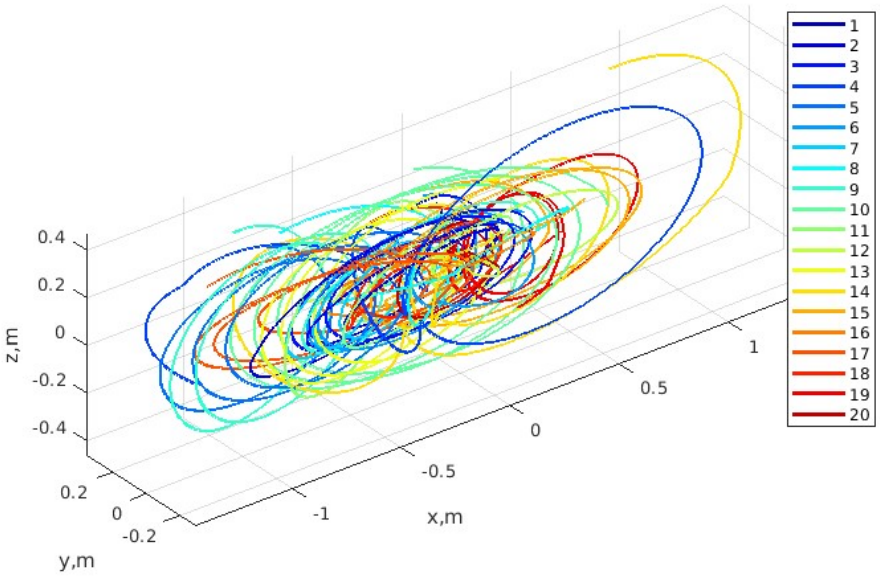

Figure 5.4: Relative trajectories for pairing method A

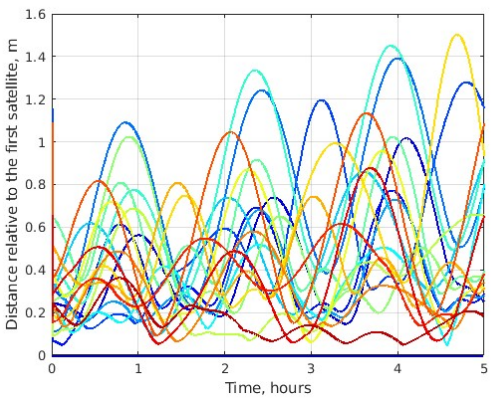

Figure 5.5: Distances relative to the first satellite for pairing method A

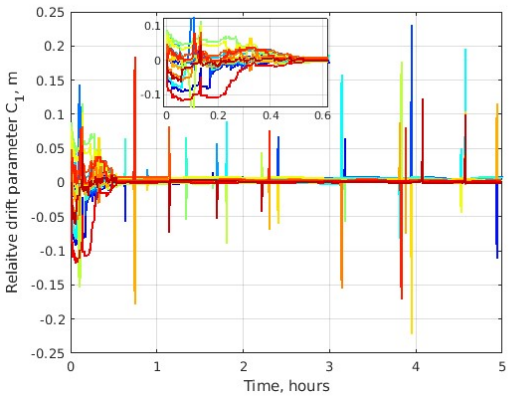

Figure 5.6: Relative drifts for pairing method A

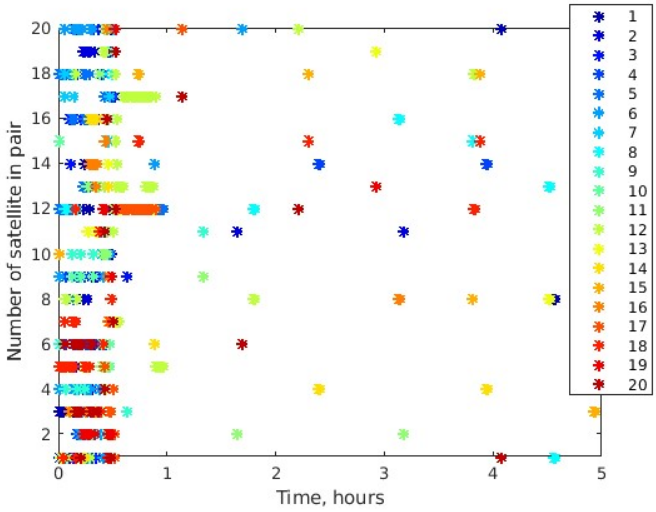

Figure 5.7: Satellite pairs over time for pairing method A

Figures 5.8 and 5.9 show the magnetic dipole moments of all the satellites and the electromagnetic forces produced over the simulation time. The magnetic dipoles values do not exceed the maximal value of 0.01 Am^2. The produced force is at its peak when it reaches the value of $3 \cdot 10^{-7}$ N. The subsequent peaks after a successful swarm assembly are caused by the collision avoidance control.

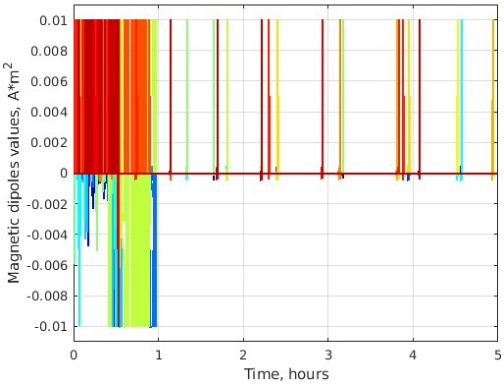

Figure 5.8: Magnetic dipole moment values for pairing method A

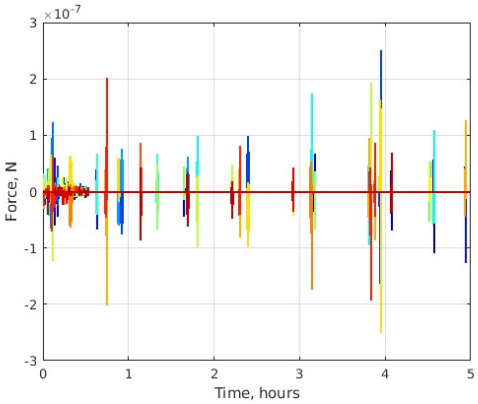

Figure 5.9: Electromagnetic forces produced for pairing method A

5.2.2 Pairing Method B

Consider the alternative pairing method B for the application of the swarm control algorithm, based on the highest relative drift value. A simulation of the swarm motion is performed with the same initial conditions from the previous example. Figure 4.10 shows the resulting bounded relative trajectories which are confined to a limited area of about 3 x 0.8 x 0.8 m^3, exhibiting slightly higher separation between satellites when compared to the results obtained from pairing method A. According to Figure 4.11, the distances relative to the first satellite do not increase with time. Figure 4.12 exhibits the relative drifts in the swarm; it can be concluded the formation stabilizes after 1.5 hours, at which point the relative drift parameter C_1 decreases to the acceptable value of 0.01 m. The subsequent increments of drift are caused by the collision avoidance control. Figure 4.13 shows the pairing of the satellites over the simulation period; as expected, a higher number of pairs is formed during the initial 1.5 hours, until swarm stability is achieved, afterwards satellites are periodically paired to correct disturbance in the swarm. Swarm stability is achieved with pairing method B, but when compared to pairing method A, the swarm exhibits slightly higher separation between satellites and the initial drift elimination is carried out over a longer period of time. Figures 4.14 and 4.16 show the magnetic dipole values between pairs and the electromagnetic forces produced, during the simulation period. It can be verified that for pairing method B, the magnetorquers produce the maximum magnetic dipole moment for longer during the initial assembly stage.

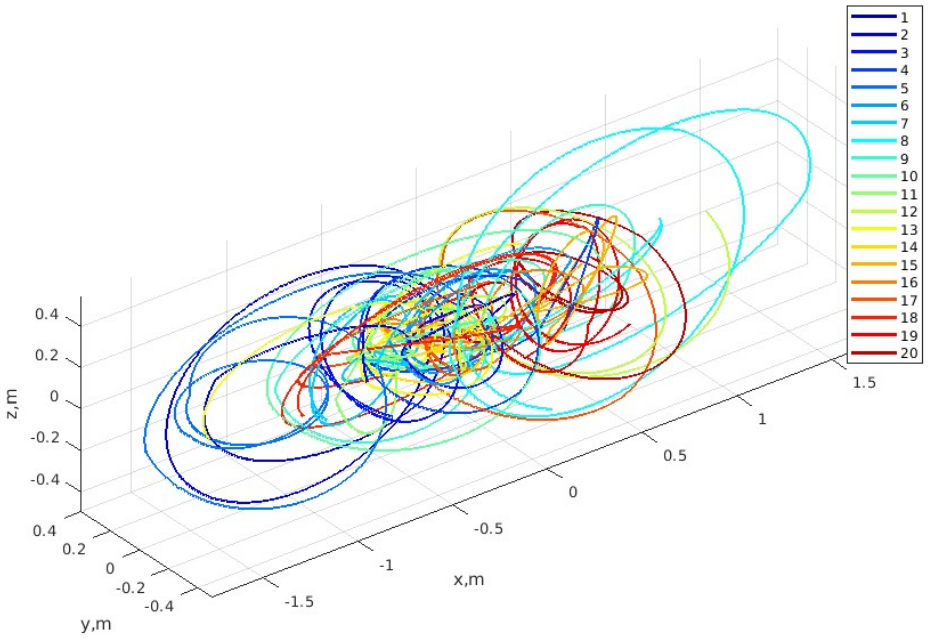

Figure 5.10: Relative trajectories for pairing method B

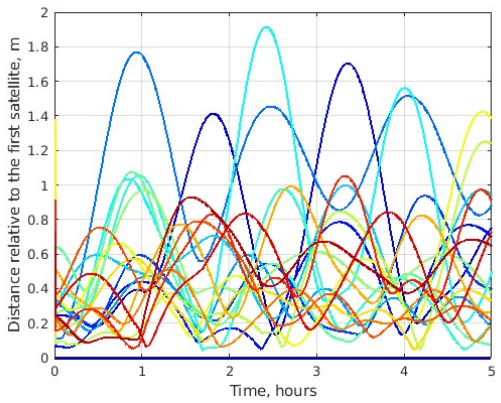

Figure 5.11: Distances relative to the first satellite for pairing method B

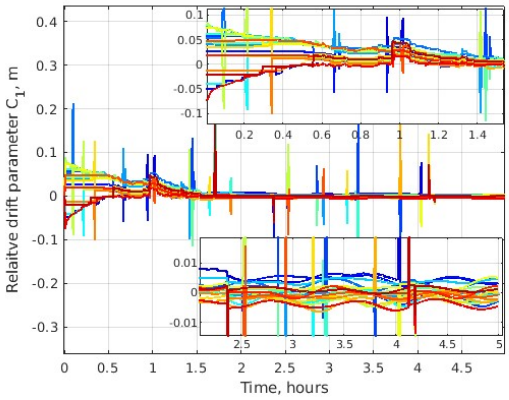

Figure 5.12: Relative drifts for pairing method B

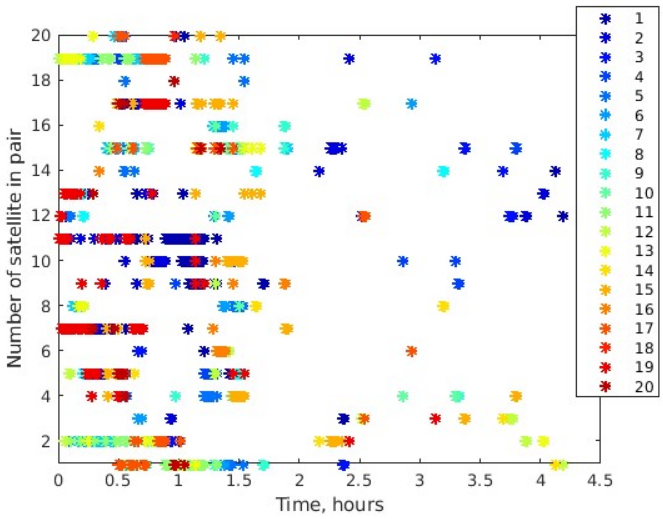

Figure 5.13: Satellite pairs over time for pairing method B

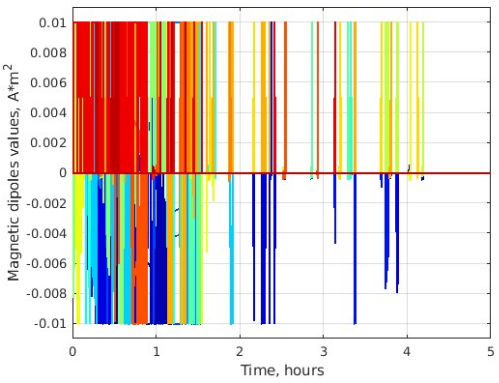

Figure 5.14: Magnetic dipole moment values for pairing method B

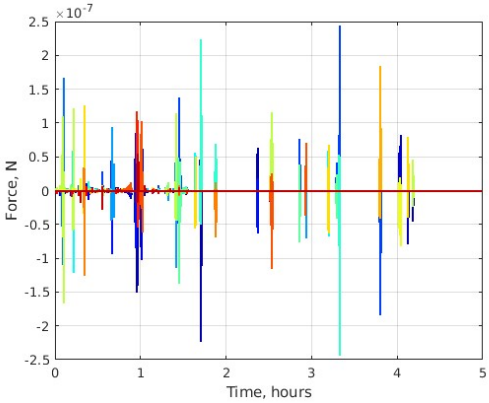

Figure 5.15: Electromagnetic forces produced for pairing method B

5.2.3 Attitude Control

When the satellites are not paired and therefore not involved in translational motion control the angular velocity damping algorithm is applied. The magnetic dipole interaction results in torque that affects angular motion and causes angular momentum to increase. Figure 4.16 shows the angular velocity components of all the satellites, Figure 4.17 shows the quaternion components of all the satellites. During active relative drift control the satellites angular rate increases up to 1000 *deg/s* that approximately equal to 3 rotations per second, which is considered a quite high value. Nevertheless, when satellites are not paired the angular velocity damping by the magnetorquers decreases these values quite rapidly. After 1 hour, when relative drift is mostly eliminated, the angular velocity is close to zero. The collision avoidance control can increase the angular velocity up to 100 *deg/s*, but this increment in angular motion is eventually damped.

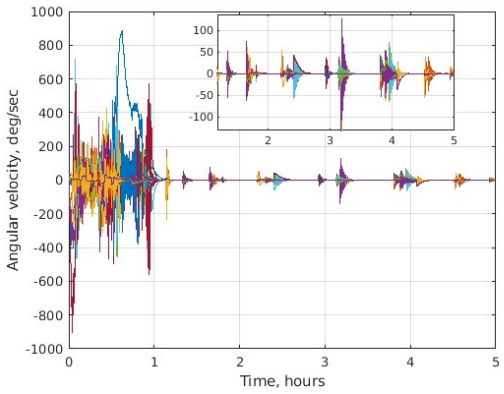

Figure 5.16: Angular velocity vector component

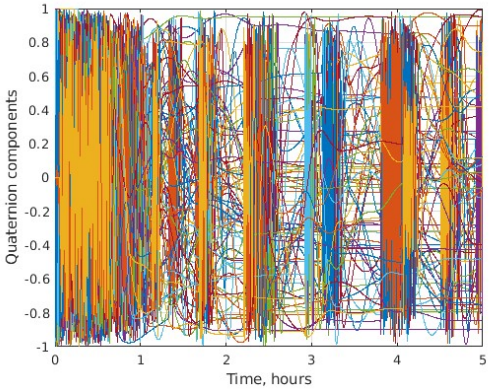

Figure 5.17: Quaternion component

5.3. Swarm Separation Analysis

Both pairing methods were successful at assembling the swarm with the proposed electromagnetic control rules. Nevertheless, the overall performance of the control application is influenced by several different algorithm parameters and other external conditions. Consider a simulation example where some of the satellites are separated from the others and the control application is only partially successful. All simulation parameters are equivalent to the previous demonstrations, except for the range of the random initial drift parameter which is defined as $C_1 \in [-0.3; 0.3]$ *m*. Pairing method A is utilized for this example, based on the nearest satellite with non-zero drift. Figure 4.18 demonstrates the relative trajectories of the twenty ChipSats over five hours of simulation. One of the satellites is separated from the swarm, in the negative direction of the *x*-axis, due to high initial drift that was not successfully eliminated by the control algorithm. A

group of four satellites managed to eliminate the relative drift amongst them but failed to eliminate the drift relative to the remaining satellites and were ultimately separated from the swarm, in the positive direction of the *x*-axis, consequently compromising swarm integrity. Figure 4.19 shows the relative distances of the satellites; the relative distances of the five satellites from the formation increased with time due to its inability to apply the required control force and eliminate drift. Their individual relative drifts registered during the simulation are exhibited in Figure 4.20; it is possible to distinguish the main section of the swarm, where control was successfully applied and the C_1 parameter converges to the vicinity of zero. The single satellite drifting towards the negative direction of the *x*-axis is represented above with varying positive relative drift values. The four remaining satellites separated from the formation, managed to eliminate the drift between one another but not relative to the main section of the swarm, registering similar negative C_1 values which caused the group to drift along the positive direction of the *x*-axis.

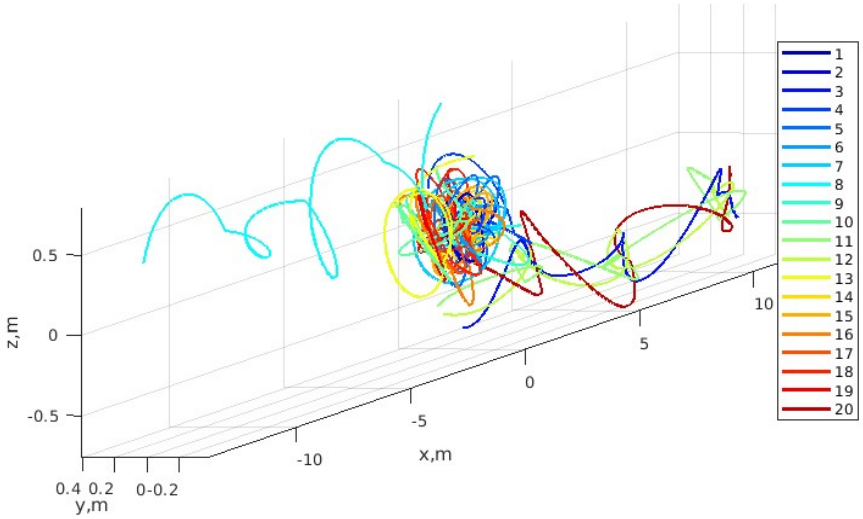

Figure 5.18: Relative trajectories exhibiting swarm separation

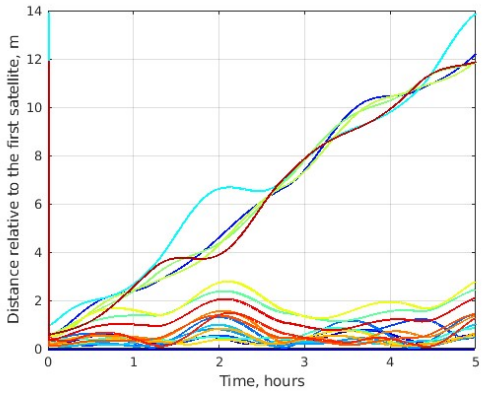

Figure 5.19: Distances relative to the first satellite

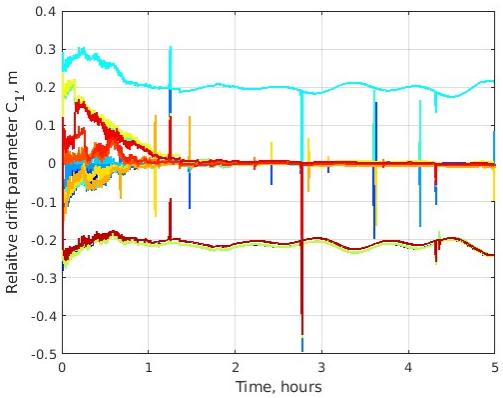

Figure 5.20: Relative drifts in case of swarm separation

In order to study this separation effect, different parameters must be considered. The performance of the control algorithm is tested over several Monte Carlo simulations using random initial conditions. Twenty numerical simulations were performed under adjusted parameters and random initial conditions. For each simulation, consider the number of satellites $N_{cluster}$ as the section of the swarm with the largest number of satellites with near-zero relative drift. This number accounts for the satellites kept in formation after the simulation period and can be compared to the total number of satellites in the simulation, $N_{total} = 20$. If $N_{cluster}/N_{total} = 1$, all satellites are able to stop relative drift between one another. In case $N_{cluster}/N_{total} < 1$, the control application is only partly successful, and some satellites are separated from the main section. The data obtained is used for statistical dispersion calculations to assess overall performance of the control algorithm.

Considering the influence of the initial drift parameter C_1 on the ability to apply the necessary control forces during swarm assembly, the simulations of the controlled motion are carried out for different intervals of the random initial value C_1, for both pairing methods, in an attempt to mimic adverse conditions imposed after the deployment of the ChipSats. For a random initial drift within the interval [-0.1;0.1] m, in accordance with the parameter used for the previous simulation examples established in Table 1, both pairing methods showed successful results with a median ratio $N_{cluster}/N_{total} = 1$. Figures 4.21 and 4.22 show the box plots of the collected data, for pairing methods A and B, respectively.

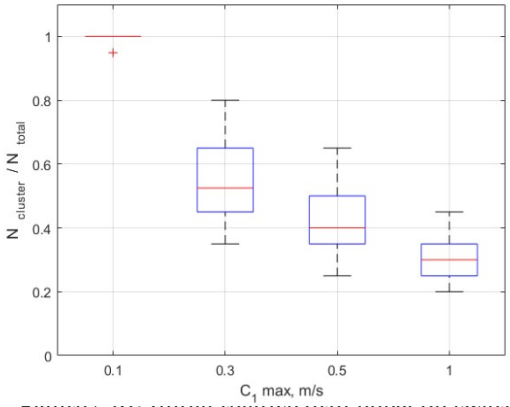

Figure 5.21: Initial relative drift effect on swarm separation for pairing method A

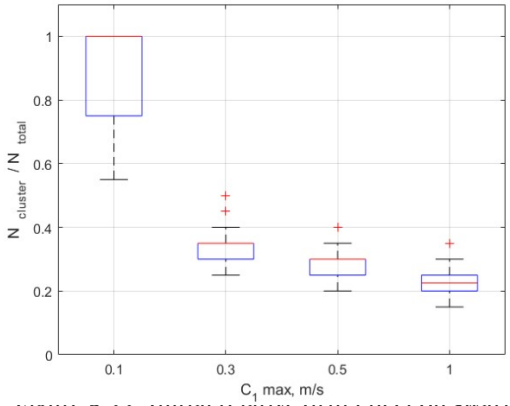

Figure 5.22: Initial relative drift effect on swarm separation for pairing method B

For a maximum C_1 value of 0.1 m, pairing method A registered a single outlier below the median, while pairing method B exhibited a higher deviation below this value with a lower quartile reaching $N_{cluster}/N_{total} = 0.75$ and minimum value of 0.55. When the maximum C_1 value is increased, so is the separation between satellites. For a maximum C_1 value of 0.3

m, 0.5 m, and 1 m, both methods performed significantly worse with median ratios falling below the 50% threshold, meaning more than half the satellites got separated. Larger initial relative drifts cause the distances between satellites to drastically increase early on, surpassing the limited reach of the dipole interaction force, as a result, the electromagnetic control force produced during the beginning of the simulation may already be far too weak to prevent separation. It is also worth noting that despite the generally reduced control efficiency for higher relative drift, pairing method A which targets the nearest satellite with non-zero relative drift, obtained higher $N_{cluster}/N_{total}$ ratios in every simulation than pairing method B which targets the satellite with the largest relative drift value. This can be explained by the fact that the electromagnetic control force is stronger and thus more efficiently applied for small relative distances, two nearby satellites produce a stronger interaction force that can reduce relative drift in a shorter period, whereas a weaker interaction force produced between two satellites with high relative drift and increasing relative distance would require a longer period of time to achieve the same result. Since separation is most likely to occur during the initial assembly stage, pairing method A can rapidly eliminate drift of nearby satellites, while pairing method B takes evidently longer to perform this task, which causes some ChipSats to separate from the swarm. This difference in the assembly period is also noticeable in the simulation examples given in Section 4.2.

Let the random initial drift interval be reset as [-0.1;0.1] m and consider the influence of the total number of ChipSats on the performance of the algorithm. A larger swarm implies additional random trajectories, increasing the disturbances caused by the number of active magnetorquers at any given time and frequent need for collision avoidance control. To assess the operational limitations on swarm size, twenty simulations are performed under the previously established parameters, for each different N_{total} values and for both paring methods. Figures 4.23 and 4.24 demonstrate the box plots of the data collected from these simulations. From the obtained results, it is asserted that performance, for both pairing methods, is reduced with the increment in swarm size. For an initial N_{total} of 20 satellites, method A wields outstanding results with two single outliers below the median $N_{cluster}/N_{total} = 1$, which indicates an ideal performance under the defined parameters. While method B wields the same median ratio as method A, data shows a comparatively higher deviation below this value, with a lower quartile reaching $N_{cluster}/N_{total} = 0.75$, and a registered minimum of 0.55. As the number of satellites increases, method A shows a slight reduction in performance, with progressively lower medians and higher deviations, yet still within acceptable values. In comparison, method B shows a significant reduction in performance proving its ineffectiveness at assembling

and maintaining larger swarms. The high deviation in the obtained results can be explained by the numerous random relative trajectories that arise from an increased number of satellites, which inevitably hinders the algorithm's ability to effectively apply the limited control force between all drifting satellites. Additionally, collision avoidance control occurrences temporarily increase relative drift and can also lead to swarm separation.

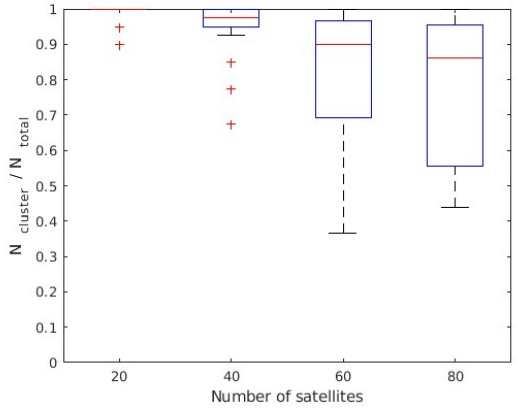

Figure 5.23: Effect of swarm size on swarm separation for pairing method A

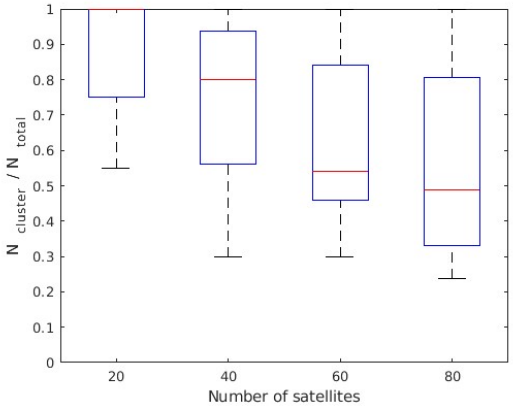

Figure 5.24: Effect of swarm size on swarm separation for pairing method B

Another important parameter worth considering is the value of the magnetic dipole produced. Although magnetorquers cannot produce large dipole moment values due to power, mass, and size restrictions, its magnitude has a direct influence on the calculated control force. Theoretically, a stronger magnetic dipole increases the magnitude of the interaction force between satellites, as well as its reach. However, an increment to this value also increases disturbances caused by nearby magnetorquers. To study the maximum dipole moment's effect on swarm separation, twenty simulation are performed for different maximum values, with a random initial drift interval of [-0.3;0.3] m. Figures 4.25 and 4.26 demonstrate the results obtained for pairing methods A and B. Data shows that pairing method A performs well with the standard operational parameter, but equivalent results can be achieved with half that value, 0.005 Am^2. When the maximum dipole moment is further reduced swarm separation increases. A more significant deviation occurs when the maximum value is increased to 0.02 Am^2. Since this method targets the closest drifting satellite, a stronger interaction force may be unnecessary during the assembly stage, after which there are less relative motion corrections required. However, it can aggravate disturbances between satellites and negatively affect performance. Pairing method B wields progressively better results for higher dipole moment values and performs well for the highest simulated value of 0.02 Am^2. This method targets the highest drifting nearby satellite, thus requiring the magnetorquers to

work at full capacity for longer until the swarm is assembled. An increment of the magnetic dipoles results in an augmented interaction force which, for this method, proves particularly beneficial during the initial stage.

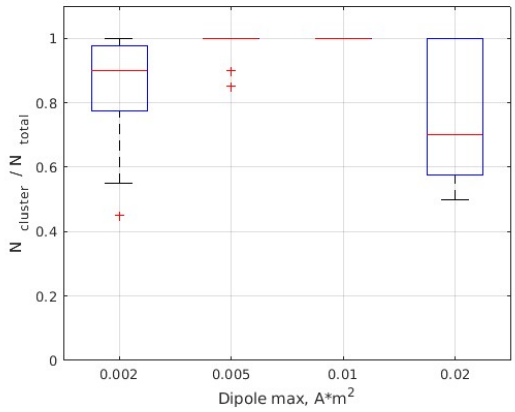

Figure 5.25: Maximum dipole moment effect on swarm separation for pairing method A

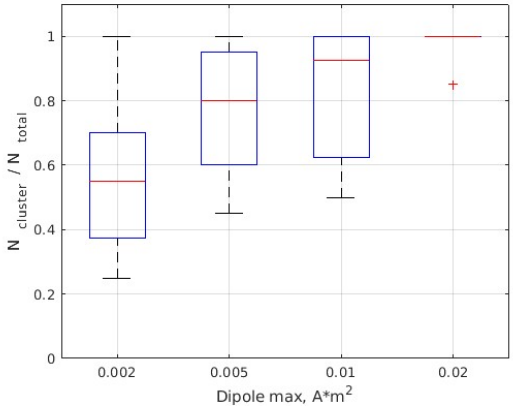

Figure 5.26: Maximum dipole moment effect on swarm separation for pairing method B

This comparative analysis indicates that pairing method A shows superior performance under straining conditions. Both methods can achieve and maintain swarm stability under favorable conditions, however method A's approach to decentralized control allows for a more efficient and swift drift elimination. Considering the magnetorquer's limited dipole moment, targeting the nearest drifting satellite proves to be a more advantageous strategy. The difference in performance is most noticeable when the number of satellites is increased; since the ChipSats are assembled at a faster rate, method A can be considered a more suitable strategy for preventing swarm separation during this stage. The most impactful parameter on both methods during the simulations is the initial relative drift. Any increment to this value significantly hinders performance due to limitations of the electromagnetic force. However, this is mainly influenced by the deployment mechanism used.

Chapter 6

Conclusions

This study demonstrates the operational capability of electromagnetic control for formation keeping, as an alternative to conventional propulsion systems. With future technology advancements towards the miniaturization and improved capability of core components, the utilization of magnetorquers as the sole actuators for rotational and translational control shows promising results. The proposed algorithm is designed for ChipSats with onboard magnetorquers in an attempt to implement decentralized electromagnetic control to swarm formation flight. Due to the small size and mass of the ChipSats, assume that the interaction force produced between magnetorquers is sufficiently strong to provide relative motion control as well as attitude stabilization. The decentralized application of control in the swarm can be achieved by independently eliminating relative drift between all satellites. Two distinct pairing methods are devised in order to regulate the interaction between ChipSats and study its effectiveness at achieving and maintaining bounded relative trajectories.

The comparative analysis shows the method targeting the nearest drifting satellite (pairing method A) is the most efficient at performing this task with consistent positive results for a restricted set of parameters. Its performance is still subject to irregularities during swarm assembly, especially due to adverse initial conditions after deployment, and the total number of satellites in the formation. The algorithm is successful with formations of up to forty satellites, but for larger swarms its efficiency varies significantly, as the complexity of the trajectories prevents accurate relative motion control. Potential mission applications for swarms may require hundreds of ChipSats to be deployed and weak performance may lead to the separation of dozens of satellites. For this reason, the algorithm must be optimized and further tested to assure optimal performance under specific mission conditions. The deployment mechanism is also an important factor that greatly affects the success of the formation. The study shows the initial relative drift to be the most impactful parameter on swarm separation; for large initial values, the algorithm cannot efficiently reduce relative drift in a timely manner due to the limited dipole moment, this causes the relative distance between satellites to drastically increase early on, preventing a successful assembly. The performance assessment made on this parameter indicates that for pairing method A the magnetorquers should ideally produce between 0.005 Am^2 and 0.01 Am^2, while for pairing method B a value of 0.02 Am^2 or more is recommended.

6.1. Future Work

During its developmental phase, the algorithm is tested over several simulations that allow the continuous improvement of its core functions. Due to the limited computing power available, its performance cannot be thoroughly tested under more straining conditions, mainly with larger numbers of satellites and/or for longer simulation periods, as these parameters significantly increase the complexity of a simulation. Further testing of the algorithm would likely expose performance weaknesses in some of its components that could potentially be improved or revised.

The two pairing methods enabled a comprehensive comparative study of the electromagnetic interaction and its ability to control relative motion. The same strategy could be applied to attitude control, by attempting to implement different control methods and comparing the obtained results. Moreover, the implementation of precise attitude pointing to each satellite, rather than simple angular velocity damping, would remarkably improve the operational capability of the swarm as a distributed sensor system.

Utilizing magnetorquers for both relative motion and attitude control poses a significant challenge for the development of the algorithm, as each control objective requires separate control calculations for the same actuator. Since both tasks are vital for formation flight, an ideal control strategy should be capable of modulating the electromagnetic interaction between all satellites in a way that allows simultaneous relative motion and attitude control, in order to achieve optimal performance of the formation as a whole.

6.2. Publications Resulting from the Research

- D. Ivanov, R. Gondar, A. Guerman, U. Monakhova '*Decentralized Electromagnetic Control of ChipSats Swarm Using Magnetorquers*' – Proc. of the IAC CyberSpace Edition 2020 (C1, IAF Astrodynamics Symposium, 1. Guidance, Navigation and Control) [54].

- D. Ivanov, R. Gondar, A. Guerman, U. Monakhova '*Electromagnetic Uncoordinated Control of a ChipSats Swarm Using Magnetorquers*' – Submitted to Acta Astronautica [55]

Bibliography

[1] A. A. B. Ruíz, *Carvalho, R. A. de, Estela, J., & Langer, M. (2020). Nanosatellites Space and Ground Technologies, Operations and Economics.*, vol. 3, no. 2. 2015.

[2] C. Foster *et al.*, 'Constellation phasing with differential drag on planet labs satellites', *J. Spacecr. Rockets*, vol. 55, no. 2, pp. 473–483, 2018, doi: 10.2514/1.A33927.

[3] A. Aldeghi, S. Carn, R. Escobar-Wolf, and G. Groppelli, 'Volcano monitoring from space using high-cadence planet CubeSat images applied to Fuego volcano, Guatemala', *Remote Sens.*, vol. 11, no. 18, 2019, doi: 10.3390/rs11182151.

[4] 'Nanosats Database'. https://www.nanosats.eu/ (accessed Sep. 23, 2020).

[5] 'Constellation Database'. https://www.nanosats.eu/tables#constellations (accessed Sep. 23, 2020).

[6] 'Planet to offer higher resolution, more spectral bands'. https://spacenews.com/planet-superdoves/ (accessed Sep. 23, 2020).

[7] Z. Manchester, M. Peck, and A. Filo, 'KickSat : A Crowd-Funded Mission To Demonstrate The World's Smallest Spacecraft', *Annu. AIAA/USU Conf. Small Satell.*, no. August 2013, pp. SSC13-IX–5, 2013.

[8] T. R. Perez and K. Subbarao, 'A Survey of Current Femtosatellite Designs, Technologies, and Mission Concepts', *JoSS*, vol. 5, no. 3, pp. 467–482, 2016, [Online]. Available: www.jossonline.com.

[9] 'Cracker-sized satellites demonstrate new space tech'. https://news.cornell.edu/stories/2019/06/cracker-sized-satellites-demonstrate-new-space-tech (accessed Sep. 23, 2020).

[10] G. Hulot, 'A constellation to study the Earth's magnetic field', pp. 351–358, 2010.

[11] F. Y. Hadaegh, S. J. Chung, and H. M. Manohara, 'On development of 100-gram-class spacecraft for swarm applications', *IEEE Syst. J.*, vol. 10, no. 2, pp. 673–684, 2016, doi: 10.1109/JSYST.2014.2327972.

[12] S. Persson, P. Bodin, E. Gill, J. Harr, and J. Jörgensen, 'PRISMA - An autonomous formation flying mission', *Eur. Sp. Agency, (Special Publ. ESA SP*, vol. 625 SP, no. September, pp. 25–29, 2006.

[13] P. Bodin, R. Larsson, F. Nilsson, C. Chasset, R. Noteborn, and M. Nylund, 'PRISMA: An in-orbit test bed for guidance, navigation, and control experiments', *J.*

Spacecr. Rockets, vol. 46, no. 3, pp. 615–623, 2009, doi: 10.2514/1.40161.

[14] C. Chasset, S. Berge, P. Bodin, and B. Jakobsson, '3-Axis Magnetic Control With Multiple Attitude Profile Capabilities in the Prisma Mission', *Sp. Technol.*, vol. 26, no. 3–4, pp. 137–154, 2006, doi: 10.2514/6.iac-06-c1.2.03.

[15] C. Chasset, R. Noteborn, P. Bodin, R. Larsson, and B. Jakobsson, '3-Axis magnetic control: Flight results of the TANGO satellite in the PRISMA mission', *CEAS Sp. J.*, vol. 5, no. 1–2, pp. 1–17, 2013, doi: 10.1007/s12567-013-0034-9.

[16] R. Noteborn, 'Flight Results from the PRISMA Optical Line of Sight Based Autonomous Rendezvous Experiment', *Proc. 4th Int. Conf. Spacecr. Form. Fly. Mission. an Technol. May 2011, Montr. Canada*, no. September 2015, p. 10, 2011.

[17] N. G. Orr, J. K. Eyer, B. P. Larouche, and R. E. Zee, 'Precision formation flight: The CanX-4 and CanX-5 dual nanosatellite mission', *Eur. Sp. Agency, (Special Publ. ESA SP*, no. 660 SP, 2008.

[18] N. H. Roth, B. Risi, C. C. Grant, and R. E. Zee, 'Flight Results from the CanX-4 and CanX-5 Formation Flying Mission', *4S Symp.*, no. 1, pp. 1–15, 2016, doi: 10.1016/j.jcrysgro.2014.02.053.

[19] 'KickSat'. https://www.kickstarter.com/projects/zacinaction/kicksat-your-personal-spacecraft-in-space (accessed Sep. 25, 2020).

[20] 'KickSat, A tiny open source spacecraft project'. https://kicksat.github.io/ (accessed Sep. 25, 2020).

[21] Z. Manchester, 'Centimeter-Scale Spacecraft: Design, Fabrication, And Deployment', no. August, 2015, [Online]. Available: https://ecommons.cornell.edu/handle/1813/41055.

[22] 'What is KickSat-2?' https://www.nasa.gov/ames/kicksat (accessed Sep. 25, 2020).

[23] V. H. Adams and M. Peck, 'R-Selected Spacecraft', *J. Spacecr. Rockets*, vol. 57, no. 1, pp. 90–98, 2020, doi: 10.2514/1.A34564.

[24] J. Cao, C. Clcmente, C. McInnes, J. Soraghan, and D. Uttamchandani, 'IAC-15-B4.6B.4 A novel concept for earth remote sensing using a bi-static femto-satellite swarm in sun synchronous orbit', *Proc. Int. Astronaut. Congr. IAC*, vol. 6, pp. 4654–4662, 2015.

[25] Z. Hu, T. Timmons, and C. Mcinnes, 'Enlighten – Research publications by members of the University of Glasgow BIS-RS-2019-26 Development of a 10g Femto-satellite with Active Attitude Control', no. November, pp. 12–14, 2019.

[26] S. Dayal and S. Blyde, 'IAC-20-B4,7,5,x60131 Highly distributed ChipSats to

provide in-situ measurements of the magnetic field for space weather monitoring Sehaz Dayal', no. October, pp. 12–14, 2020.

[27] 'A Super Solar Flare'. https://science.nasa.gov/science-news/science-at-nasa/2008/06may_carringtonflare (accessed Nov. 30, 2020).

[28] 'Near Miss: The Solar Superstorm of July 2012'. https://science.nasa.gov/science-news/science-at-nasa/2014/23jul_superstorm (accessed Nov. 30, 2020).

[29] M. Lingam and A. Loeb, 'Impact and mitigation strategy for future solar flares', pp. 1–7, 2017, [Online]. Available: http://arxiv.org/abs/1709.05348.

[30] A. M. Hein, Z. Burkhardt, and M. Eubanks, 'Attosats: Chipsats, other gram-scale spacecraft, and beyond', *arXiv*, pp. 1–11, 2019.

[31] D. Marchetti and M. Akhoondzadeh, 'Analysis of Swarm satellites data showing seismo-ionospheric anomalies around the time of the strong Mexico (M w = 8.2) earthquake of 08 September 2017', *Adv. Sp. Res.*, vol. 62, no. 3, pp. 614–623, 2018, doi: 10.1016/j.asr.2018.04.043.

[32] R. Opromolla, G. Fasano, G. Rufino, and M. Grassi, 'A review of cooperative and uncooperative spacecraft pose determination techniques for close-proximity operations', *Prog. Aerosp. Sci.*, vol. 93, no. July, pp. 53–72, 2017, doi: 10.1016/j.paerosci.2017.07.001.

[33] G. Di Mauro, M. Lawn, and R. Bevilacqua, 'Survey on guidance navigation and control requirements for spacecraft formation-flying missions', *J. Guid. Control. Dyn.*, vol. 41, no. 3, pp. 581–602, 2018, doi: 10.2514/1.G002868.

[34] N. H. Roth, B. Risi, C. C. Grant, and R. E. Zee, 'Flight Results from the CanX-4 and CanX-5 Formation Flying Mission', *4S Symp.*, vol. 9, no. 1, pp. 35-44–44, 2016, doi: 10.1016/j.jcrysgro.2014.02.053.

[35] NASA, 'State of the Art of Small Spacecraft Technology', *State Art Small Spacecr. Technol.*, no. December, pp. 1–202, 2018, [Online]. Available: https://sst-soa.arc.nasa.gov/04-propulsion.

[36] A. Guerman, M. Ovchinnikov, G. Smirnov, and S. Trofimov, 'Closed relative trajectories for formation flying with single-input control', *Math. Probl. Eng.*, vol. 2012, 2012, doi: 10.1155/2012/967248.

[37] M. Y. Ovchinnikov and V. I. Penkov, 'Passive magnetic attitude control system for the munin nanosatellite', *Cosm. Res.*, vol. 40, no. 2, pp. 142–156, 2002, doi: 10.1023/A:1015197303662.

[38] D. Ivanov, U. Monakhova, A. Guerman, M. Ovchinnikov, and D. Roldugin,

'Decentralized Differential Drag Based Control of Nanosatellites Swarm Spatial Distribution Using Magnetorquers', *Adv. Sp. Res.*, 2020, doi: 10.1016/j.asr.2020.05.024.

[39] S. Gong, G. Yunfeng, and J. Li, 'Solar sail formation flying on an inclined Earth orbit', *Acta Astronaut.*, vol. 68, no. 1–2, pp. 226–239, 2011, doi: 10.1016/j.actaastro.2010.08.022.

[40] G. Shengping, B. Hexi, and L. Junfeng, 'Solar sail formation flying around displaced solar orbits', *J. Guid. Control. Dyn.*, vol. 30, no. 4, pp. 1148–1152, 2007, doi: 10.2514/1.24315.

[41] E. M. C. Kong, D. W. Kwon, S. A. Schweighart, L. M. Elias, R. J. Sedwick, and D. W. Miller, 'Electromagnetic formation flight for multisatellite arrays', *J. Spacecr. Rockets*, vol. 41, no. 4, pp. 659–666, 2004, doi: 10.2514/1.2172.

[42] U. Ahsun, D. W. Miller, and J. L. Ramirez, 'Control of electromagnetic satellite formations in near-Earth orbits', *J. Guid. Control. Dyn.*, vol. 33, no. 6, pp. 1883–1891, 2010, doi: 10.2514/1.47637.

[43] D. W. Kwon, 'Propellantless formation flight applications using electromagnetic satellite formations', *Acta Astronaut.*, vol. 67, no. 9–10, pp. 1189–1201, 2010, doi: 10.1016/j.actaastro.2010.06.042.

[44] X. L. Huang, C. Zhang, and X. J. Ban, 'Dipole solution and angular-momentum minimization for two-satellite electromagnetic formation flight', *Acta Astronaut.*, vol. 119, pp. 79–86, 2016, doi: 10.1016/j.actaastro.2015.11.009.

[45] C. Zhang and X. L. Huang, 'Angular-momentum management of electromagnetic formation flight using alternating magnetic fields', *J. Guid. Control. Dyn.*, vol. 39, no. 6, pp. 1292–1302, 2016, doi: 10.2514/1.G001529.

[46] M. Y. Ovchinnikov and D. S. Roldugin, 'A survey on active magnetic attitude control algorithms for small satellites', *Prog. Aerosp. Sci.*, vol. 109, no. June, 2019, doi: 10.1016/j.paerosci.2019.05.006.

[47] H. D. Curtis *et al.*, *Orbital Mechanics for Engineering Students Third Edition Butterworth-Heinemann is an imprint of Elsevier*. 2014.

[48] G. R. Hintz, *Orbital Mechanics and Astrodynamics*. 2015.

[49] F. Guo, Y. Fan, and Z. Yiyu, *Space Electronic Reconnaissance: Localization Theories and Methods*, First Edit. John Wiley & Sons Singapore Pte Ltd., 2014.

[50] G. W. Hill, 'Researches in the Lunar Theory', *Am. J. Math.*, vol. 1, no. 1, pp. 5–26, 1878, doi: 10.2307/2369430.

[51] V. A. Chobotov, *Orbital Mechanics, Third Edition*. 2002.

[52] F. Celani, 'Robust three-axis attitude stabilization for inertial pointing spacecraft using magnetorquers', *Acta Astronaut.*, vol. 107, pp. 87–96, 2015, doi: 10.1016/j.actaastro.2014.11.027.

[53] A. M. Kovalev, 'The construction of Lyapunov functions with sign-definite derivative for systems satisfying the Barbashin-Krasovskii theorem', *J. Appl. Math. Mech.*, vol. 72, no. 2, pp. 164–168, 2008, doi: 10.1016/j.jappmathmech.2008.04.008.

[54] D. Ivanov, R. Gondar, A. Guerman, and U. Monakhova, 'Decentralized Electromagnetic Control of ChipSats Swarm Using Magnetorquers', 2020, [Online]. Available: https://iafastro.directory/iac/paper/id/60901/summary/.

[55] D. Ivanov, R. Gondar, U. Monakhova, A. Guerman, and M. Ovchinnikov, 'Electromagnetic Uncoordinated Control of a ChipSats Swarm Using Magnetorquers', *Acta Astronaut.*, 2021.

Appendix A - Hill-Clohessy-Wiltshire Equations

A.1 Linearization of the HCW Equations

There are different methods to derive the HCW equations available in the literature. The method applied here is described in more detail in [47]. To begin, consider two satellites in a leader-follower configuration orbiting Earth. Let $\boldsymbol{R}_i$ and $\boldsymbol{R}_j$ be the position vectors of the leader and of the follower, respectively, in the ECI reference frame. And let $\boldsymbol{R}_{ij}$ be the relative position vector of the follower relative to the leader, expressed in the ECI reference frame. Note that $\boldsymbol{R}_{ij}$ is of much smaller magnitude than $\boldsymbol{R}_i$ (or $\boldsymbol{R}_j$), so that

$$\frac{\|\boldsymbol{R}_{ij}\|}{\|\boldsymbol{R}_i\|} \ll 1 \tag{A.1}$$

The relative position vector of the follower can be defined as,

$$\boldsymbol{R}_j = \boldsymbol{R}_i + \boldsymbol{R}_{ij} \tag{A.2}$$

From Eq. (3.33) the equation of motion for the two bodies is determined,

$$\ddot{\boldsymbol{R}}_j + \mu \frac{\boldsymbol{R}_j}{\|\boldsymbol{R}_j\|^3} = 0$$

$$\ddot{\boldsymbol{R}}_{ij} = -\ddot{\boldsymbol{R}}_i - \mu \frac{\boldsymbol{R}_i + \boldsymbol{R}_{ij}}{\|\boldsymbol{R}_i + \boldsymbol{R}_{ij}\|^3} \tag{A.3}$$

It is known from Eq. (A.1.1), that $||\,\boldsymbol{R}_{ij}\,||$ is a comparatively small value, therefore all powers of $||\,\boldsymbol{R}_{ij}\,||/||\,\boldsymbol{R}_i\,||$ greater than unity can be neglected, according to Eq. (A.1), in order to simplify Eq. (A.1.3). First note that,

$$\begin{aligned}\|\boldsymbol{R}_j\|^2 = \|\boldsymbol{R}_i + \boldsymbol{R}_{ij}\|^2 = \boldsymbol{R}_j \cdot \boldsymbol{R}_j = (\boldsymbol{R}_i + \boldsymbol{R}_{ij}) \cdot (\boldsymbol{R}_i + \boldsymbol{R}_{ij}) \\ = \boldsymbol{R}_i \cdot \boldsymbol{R}_i + 2\boldsymbol{R}_i \cdot \boldsymbol{R}_{ij} + \boldsymbol{R}_{ij} \cdot \boldsymbol{R}_{ij}\end{aligned} \tag{A.4}$$

The term $\boldsymbol{R}_i \cdot \boldsymbol{R}_i = ||\,\boldsymbol{R}_{ij}\,||^2$, and can be factored out yielding,

$$\|\boldsymbol{R}_i + \boldsymbol{R}_{ij}\|^2 = \|\boldsymbol{R}_i\|^2 \left[1 + \frac{2\boldsymbol{R}_i \cdot \boldsymbol{R}_{ij}}{\|\boldsymbol{R}_i\|^2} + \left(\frac{\|\boldsymbol{R}_{ij}\|}{\|\boldsymbol{R}_i\|}\right)^2\right] \tag{A.5}$$

The term (|| $\boldsymbol{R}_{ij}$ ||/|| $\boldsymbol{R}_i$ ||)² is neglected by virtue of Eq. (A.1),

$$\left\|\boldsymbol{R}_i + \boldsymbol{R}_{ij}\right\|^2 = \|\boldsymbol{R}_i\|^2 \left[1 + \frac{2\boldsymbol{R}_i \cdot \boldsymbol{R}_{ij}}{\|\boldsymbol{R}_i\|^2}\right] \tag{A.6}$$

Since,

$$\left\|\boldsymbol{R}_j\right\|^{-3} = \left(\left\|\boldsymbol{R}_j\right\|^2\right)^{-\frac{3}{2}} \tag{A.7}$$

$$\left\|\boldsymbol{R}_i + \boldsymbol{R}_{ij}\right\|^{-3} = \|\boldsymbol{R}_i\|^{-3} \left[1 + \frac{2\boldsymbol{R}_i \cdot \boldsymbol{R}_{ij}}{\|\boldsymbol{R}_i\|^2}\right]^{-\frac{3}{2}} \tag{A.8}$$

Applying the binomial expansion theorem from [47, p. 378]:

$$(a+b)^n = a^n + n \cdot a^{n-1} \cdot b + \frac{n(n-1)}{2!} a^{n-2} \cdot b^2 + \frac{n(n-1)(n-2)}{3!} a^{n-3} \cdot b^3 + \cdots \tag{A.9}$$

$$\left(1 + \frac{2\boldsymbol{R}_i \cdot \boldsymbol{R}_{ij}}{\|\boldsymbol{R}_i\|^2}\right)^{-\frac{3}{2}} = 1 + \left(-\frac{3}{2}\right)\left(\frac{2\boldsymbol{R}_i \cdot \boldsymbol{R}_{ij}}{\|\boldsymbol{R}_i\|^2}\right) \tag{A.10}$$

Then Eq. (A.1.7) becomes,

$$\left\|\boldsymbol{R}_i + \boldsymbol{R}_{ij}\right\|^{-3} = \|\boldsymbol{R}_i\|^{-3} \left(1 - \frac{3\boldsymbol{R}_i \cdot \boldsymbol{R}_{ij}}{\|\boldsymbol{R}_i\|^2}\right)$$

$$\frac{1}{\left\|\boldsymbol{R}_i + \boldsymbol{R}_{ij}\right\|^3} = \frac{1}{\|\boldsymbol{R}_i\|^3} - \frac{1}{\|\boldsymbol{R}_i\|^5} \boldsymbol{R}_i \cdot \boldsymbol{R}_{ij} \tag{A.11}$$

Substituting Eq. (A.11) into Eq. (A.3) yields,

$$\ddot{\boldsymbol{R}}_{ij} = -\ddot{\boldsymbol{R}}_i - \mu\left(\frac{1}{\|\boldsymbol{R}_i\|^3} - \frac{1}{\|\boldsymbol{R}_i\|^5} \boldsymbol{R}_i \cdot \boldsymbol{R}_{ij}\right)\left(\boldsymbol{R}_i + \boldsymbol{R}_{ij}\right)$$

$$= -\ddot{\boldsymbol{R}}_i - \mu\left[\frac{\boldsymbol{R}_i + \boldsymbol{R}_{ij}}{\|\boldsymbol{R}_i\|^3} - \frac{1}{\|\boldsymbol{R}_i\|^5}\left(\boldsymbol{R}_i \cdot \boldsymbol{R}_{ij}\right)\left(\boldsymbol{R}_i + \boldsymbol{R}_{ij}\right)\right]$$

$$= -\ddot{\boldsymbol{R}}_i - \mu\left[\frac{\boldsymbol{R}_i}{\|\boldsymbol{R}_i\|^3} + \frac{\boldsymbol{R}_{ij}}{\|\boldsymbol{R}_i\|^3} - \frac{1}{\|\boldsymbol{R}_i\|^5}\left(\boldsymbol{R}_i \cdot \boldsymbol{R}_{ij}\right)\boldsymbol{R}_i + \overbrace{terms\ of\ higher\ order\ than\ 1\ in\ \boldsymbol{R}_{ij}}^{neglect}\right]$$

$$\ddot{\boldsymbol{R}}_{ij} = -\ddot{\boldsymbol{R}}_i - \mu\frac{\boldsymbol{R}_i}{\|\boldsymbol{R}_i\|^3} - \frac{\mu}{\|\boldsymbol{R}_i\|^3}\left[\boldsymbol{R}_{ij} - \frac{3}{\|\boldsymbol{R}_i\|^2}\left(\boldsymbol{R}_i \cdot \boldsymbol{R}_{ij}\right)\boldsymbol{R}_i\right] \tag{A.12}$$

The equation of motion (3.33) of the leader is:

$$\ddot{\boldsymbol{R}}_i = -\frac{\mu}{r^3}\boldsymbol{R}_i \tag{A.13}$$

Substituting it into Eq. (A.12) yields the simplified equation of the two-body system,

$$\ddot{\boldsymbol{R}}_{ij} = -\frac{\mu}{\|\boldsymbol{R}_i\|^3}\left[\boldsymbol{R}_{ij} - \frac{3}{\|\boldsymbol{R}_i\|^2}(\boldsymbol{R}_i \cdot \boldsymbol{R}_{ij})\boldsymbol{R}_i\right] \tag{A.14}$$

This expression is a linear approximation of the motion of the follower relative to the leader, obtained by dropping negligible terms, which is only valid if Eq. (A.1.1) is true. In the rotating Hill frame established in Section 3.1, the *z*-axis lies along the radial $\boldsymbol{R}_i$, so that,

$$\boldsymbol{R}_i = R_i\hat{\boldsymbol{k}} \tag{A.15}$$

where $R_i = \|\boldsymbol{R}_i\|$. The components of the relative position vector in the comoving frame can be defined as,

$$\ddot{\boldsymbol{R}}_{ij} = x_{ij}\,\hat{\boldsymbol{\imath}} + y_{ij}\,\hat{\boldsymbol{\jmath}} + z_{ij}\,\hat{\boldsymbol{k}} \tag{A.16}$$

Substituting Eq. (A.15) and Eq. (A.16) into Eq. (A.14) yields,

$$\begin{aligned}\ddot{\boldsymbol{R}}_{ij} &= -\frac{\mu}{{R_i}^3}\left[x_{ij}\,\hat{\boldsymbol{\imath}} + y_{ij}\,\hat{\boldsymbol{\jmath}} + z_{ij}\,\hat{\boldsymbol{k}} - \frac{3}{{R_i}^2}\left(R_i\hat{\boldsymbol{k}} \cdot \left(x_{ij}\,\hat{\boldsymbol{\imath}} + y_{ij}\,\hat{\boldsymbol{\jmath}} + z_{ij}\,\hat{\boldsymbol{k}}\right)\right)R_i\hat{\boldsymbol{k}}\right] \\ &= -\frac{\mu}{{R_i}^3}\left(x_{ij}\,\hat{\boldsymbol{\imath}} + y_{ij}\,\hat{\boldsymbol{\jmath}} - 2z_{ij}\,\hat{\boldsymbol{k}}\right)\end{aligned} \tag{A.17}$$

The equation obtained corresponds to the acceleration of the follower relative to the leader, measured in the ECI frame. From Eq. (3.36) it is determined the angular momentum is normal to the reference orbit plane, and so is the *y*-axis of the Hill reference frame. Since $\mathbf{h} = h\hat{\boldsymbol{\jmath}}$, the angular velocity and angular acceleration of the leader from Eq. (3.25) can be written as,

$$\boldsymbol{\omega} = \frac{\boldsymbol{R}_i \times \boldsymbol{V}_i}{{R_i}^2}\hat{\boldsymbol{\jmath}} = \frac{h}{{R_i}^2}\hat{\boldsymbol{\jmath}} \tag{A.18}$$

$$\dot{\boldsymbol{\omega}} = -\frac{2(\boldsymbol{R}_i \cdot \boldsymbol{V}_i)h}{{R_i}^4}\hat{\boldsymbol{\jmath}} \tag{A.19}$$

Where $\boldsymbol{V}_i$ is de first derivative of $\boldsymbol{R}_i$. The equation from [47, p. 382] is applied to calculate the relative acceleration of the two bodies, measured in the Hill frame:

$$\ddot{\boldsymbol{r}}_{ij} = \ddot{\boldsymbol{R}}_{ij} - \underbrace{\dot{\boldsymbol{\omega}} \times \boldsymbol{R}_{ij}}_{a} - \underbrace{\boldsymbol{\omega} \times \left(\boldsymbol{\omega} \times \boldsymbol{R}_{ij}\right)}_{b} - \underbrace{2\boldsymbol{\omega} \times \boldsymbol{v}_{ij}}_{c} \tag{A.20}$$

where,

$$\boldsymbol{r}_{ij} = x_{ij}\,\hat{\boldsymbol{\imath}} + y_{ij}\,\hat{\boldsymbol{\jmath}} + z_{ij}\,\hat{\boldsymbol{k}} \tag{A.21}$$

$$\boldsymbol{v}_{ij} = \dot{x}_{ij}\,\hat{\boldsymbol{\imath}} + \dot{y}_{ij}\,\hat{\boldsymbol{\jmath}} + \dot{z}_{ij}\,\hat{\boldsymbol{k}} \tag{A.22}$$

are the relative state vectors in the Hill reference frame, established in Eq. (3.26). substituting Eqs. (A.16), (A.18), and (A.19) into Eq. (A.20) yields

$$a)\quad \dot{\boldsymbol{\omega}} \times \boldsymbol{R}_{ij} = \left[-\frac{2(\boldsymbol{R}_i \cdot \boldsymbol{V}_i)h}{{R_i}^4}\hat{\boldsymbol{\jmath}}\right] \times \left(x_{ij}\,\hat{\boldsymbol{\imath}} + y_{ij}\,\hat{\boldsymbol{\jmath}} + z_{ij}\,\hat{\boldsymbol{k}}\right) = \frac{2(\boldsymbol{R}_i \cdot \boldsymbol{V}_i)h}{{R_i}^4}\left(-z_{ij}\,\hat{\boldsymbol{\imath}} + x_{ij}\,\hat{\boldsymbol{k}}\right) \tag{A.23}$$

$$b)\quad \boldsymbol{\omega} \times \left(\boldsymbol{\omega} \times \boldsymbol{R}_{ij}\right) = \frac{h}{{R_i}^2}\hat{\boldsymbol{\jmath}} \times \left[\frac{h}{{R_i}^2}\hat{\boldsymbol{\jmath}} \times \left(x_{ij}\,\hat{\boldsymbol{\imath}} + y_{ij}\,\hat{\boldsymbol{\jmath}} + z_{ij}\,\hat{\boldsymbol{k}}\right)\right] = -\frac{h^2}{{R_i}^4}\left(x_{ij}\,\hat{\boldsymbol{\imath}} + z_{ij}\,\hat{\boldsymbol{k}}\right) \tag{A.24}$$

$$c)\quad 2\boldsymbol{\omega} \times \boldsymbol{v}_{ij} = 2\frac{h}{{R_i}^2}\hat{\boldsymbol{\jmath}} \times \left(\dot{x}_{ij}\,\hat{\boldsymbol{\imath}} + \dot{y}_{ij}\,\hat{\boldsymbol{\jmath}} + \dot{z}_{ij}\,\hat{\boldsymbol{k}}\right) = 2\frac{h}{{R_i}^2}\left(\dot{z}_{ij}\,\hat{\boldsymbol{\imath}} - \dot{x}_{ij}\,\hat{\boldsymbol{k}}\right) \tag{A.25}$$

Considering Eq. (A.1.14), Eq. (A.1.17) becomes

$$\ddot{\boldsymbol{r}}_{ij} = \overbrace{-\frac{\mu}{{R_i}^3}\left(x_{ij}\,\hat{\boldsymbol{\imath}} + y_{ij}\,\hat{\boldsymbol{\jmath}} - 2z_{ij}\,\hat{\boldsymbol{k}}\right)}^{\ddot{\boldsymbol{R}}_{ij}} - \overbrace{\frac{2(\boldsymbol{R}_i \cdot \boldsymbol{V}_i)h}{{R_i}^4}\left(-z_{ij}\,\hat{\boldsymbol{\imath}} + x_{ij}\,\hat{\boldsymbol{k}}\right)}^{a} - \left[\overbrace{-\frac{h^2}{{R_i}^4}\left(x_{ij}\,\hat{\boldsymbol{\imath}} + z_{ij}\,\hat{\boldsymbol{k}}\right)}^{b}\right] - \overbrace{2\frac{h}{{R_i}^2}\left(\dot{z}_{ij}\,\hat{\boldsymbol{\imath}} - \dot{x}_{ij}\,\hat{\boldsymbol{k}}\right)}^{c} \tag{A.26}$$

The relative acceleration in the Hill frame is defined as

$$\ddot{\boldsymbol{r}}_{ij} = \ddot{x}_{ij}\,\hat{\boldsymbol{\imath}} + \ddot{y}_{ij}\,\hat{\boldsymbol{\jmath}} + \ddot{z}_{ij}\,\hat{\boldsymbol{k}} \tag{A.27}$$

and can be applied to Eq. (A.26),

$$\begin{aligned}\ddot{x}_{ij}\,\hat{\boldsymbol{\imath}} + \ddot{y}_{ij}\,\hat{\boldsymbol{\jmath}} + \ddot{z}_{ij}\,\hat{\boldsymbol{k}} = &\left[\left(\frac{h^2}{{R_i}^4} - \frac{\mu}{{R_i}^3}\right)x_{ij} + \frac{2(\boldsymbol{R}_i \cdot \boldsymbol{V}_i)h}{{R_i}^4}z_{ij} - 2\frac{h}{{R_i}^2}\dot{z}_{ij}\right]\hat{\boldsymbol{\imath}} \\ &-\frac{\mu}{{R_i}^3}y_{ij}\,\hat{\boldsymbol{\jmath}} + \left[\left(\frac{h^2}{{R_i}^4} + \frac{2\mu}{{R_i}^3}\right)z_{ij} - \frac{2(\boldsymbol{R}_i \cdot \boldsymbol{V}_i)h}{{R_i}^4}x_{ij} + 2\frac{h}{{R_i}^2}\dot{x}_{ij}\right]\hat{\boldsymbol{k}}\end{aligned} \tag{A.28}$$

Eq. (A.1.19) can be re-arranged according to the three unit components of the relative acceleration vector,

$$\begin{cases} \ddot{x}_{ij} = \left(\dfrac{h^2}{{R_i}^4} - \dfrac{\mu}{{R_i}^3}\right) x_{ij} + \dfrac{2(\boldsymbol{R}_i \cdot \boldsymbol{V}_i)h}{{R_i}^4} z_{ij} - 2\dfrac{h}{{R_i}^2}\dot{z}_{ij} \\ \ddot{y}_{ij} = -\dfrac{\mu}{{R_i}^3} y_{ij} \\ \ddot{z}_{ij} = \left(\dfrac{2\mu}{{R_i}^3} + \dfrac{h^2}{{R_i}^4}\right) z_{ij} - \dfrac{2(\boldsymbol{R}_i \cdot \boldsymbol{V}_i)h}{{R_i}^4} x_{ij} + 2\dfrac{h}{{R_i}^2}\dot{x}_{ij} \end{cases} \tag{A.29}$$

This set of linear second-order differential equations can be solved to obtain the relative position coordinates x_{ij}, y_{ij}, and z_{ij} in the Hill reference frame, as a function of time. Consider the circular orbit of the leader satellite, and that the angular momentum is constant, $\boldsymbol{R}_i \cdot \boldsymbol{R}_i = 0$. The angular velocity of the leader equals the frequency of revolution of the Hill frame, calculated with the mean motion Eq. (3.2),

$$\omega = n = \frac{V_i}{R_i} = \sqrt{\frac{\mu}{{R_i}^3}} \;\; and \;\; h = \sqrt{\mu R_i} \tag{A.30}$$

applying these substitutions to Eq. (A.29) yields the simplified Hill-Clohessy-Wiltshire equations:

$$\ddot{x}_{ij} + 2\omega\dot{z}_{ij} = 0 \tag{A.31}$$

$$\ddot{y}_{ij} + \omega^2 y_{ij} = 0 \tag{A.32}$$

$$\ddot{z}_{ij} - 2\omega\dot{x}_{ij} - 3\omega^2 z_{ij} = 0 \tag{A.33}$$

A.2 Derivation of the Controlled HCW Equations

With a projected circular orbit, it is possible to obtain an analytical solution to the HCW equations that provides bounded relative trajectories, since the coefficients in Eq. (A.31-A.33) are constant for circular orbits. Eqs. (A.31) and (A.33) are coupled and dictate the motion of the follower relative to the leader in the *x*-*z* plane, while Eq. (A.32) contains an isolated variable of the relative motion in the *z* direction, normal to the orbital plane and independent from the motion in the other two directions. The solution provided in Eqs. (3.40-3.43) is:

$$x_{ij}(t) = -3{C_1}^{ij}\,\omega t + 2{C_2}^{ij}\,cos(\omega t) - 2{C_3}^{ij}\,sin(\omega t) + {C_4}^{ij} \tag{A.34}$$

$$y_{ij}(t) = {C_5}^{ij}\,sin(\omega t) + {C_6}^{ij}\,cos(\omega t) \tag{A.35}$$

$$z_{ij}(t) = 2{C_1}^{ij} + {C_2}^{ij}\,sin(\omega t) + {C_3}^{ij}\,cos(\omega t) \tag{A.36}$$

$$\begin{aligned} {C_1}^{ij} &= \frac{\dot{x}_{ij}(0)}{\omega} + 2z(0) \qquad {C_2}^{ij} = \frac{\dot{z}_{ij}(0)}{\omega} \qquad {C_3}^{ij} = -3z(0) - \frac{2\dot{x}_{ij}(0)}{\omega} \\ {C_4}^{ij} &= x(0) - \frac{\dot{z}_{ij}(0)}{\omega} \qquad {C_5}^{ij} = \frac{\dot{y}_{ij}(0)}{\omega} \qquad {C_6}^{ij} = y_{ij}(0) \end{aligned} \tag{A.37}$$

The control vector, with a single non-zero component, is introduced in Eqs. (3.44-3.46) to correct the term *-3C₁ωt*, responsible for relative drift along the *x*-axis. Closed relative trajectories are achieved if $C_1 = 0$. The proposed controlled HCW are:

$$\ddot{x}_{ij} + 2\omega\dot{z}_{ij} = u_{ij} \tag{A.38}$$

$$\ddot{y}_{ij} + \omega^2 y_{ij} = 0 \tag{A.39}$$

$$\ddot{z}_{ij} - 2\omega\dot{x}_{ij} - 3\omega^2 z_{ij} = 0 \tag{A.40}$$

First, Eq. (A.40) is derived,

$$\frac{d}{dt}\ddot{z}_{ij} = \dddot{z}_{ij} - 2\omega\ddot{x}_{ij} - 3\omega^2\dot{z}_{ij} \tag{A.41}$$

Re-arranging and substituting Eq. (A.38) into Eq. (A.41) results in

$$\begin{aligned} \frac{d}{dt}\ddot{z}_{ij} &= \dddot{z}_{ij} - 2\omega\left(u_{ij} + 2\omega\dot{z}_{ij}\right) - 3\omega^2\dot{z}_{ij} \\ &= \dddot{z}_{ij} - 2\omega u_{ij} + \omega^2\dot{z}_{ij} = 0 \end{aligned} \tag{A.42}$$

$$\ddot{z}_{ij} + \omega^2 \dot{z}_{ij} = \overbrace{2\omega u_{ij}}^{control} \tag{A.43}$$

$$\begin{aligned} &\rightarrow {z_{ij}}^3 + \omega^2 z_{ij} = 0 \\ &z_{ij}\left({z_{ij}}^2 + \omega^2\right) = 0 \\ &z_{ij} = 0 \cup z_{ij} = \pm i\omega \end{aligned} \tag{A.44}$$

A particular solution to the Eq. (A.40) can be obtained if, $z_{ij}{}^3 = 0$, resulting in

$$z_{ij} = \frac{2u_{ij}}{\omega} \tag{A.45}$$

The particular solution in Eq. (A.45) is then added to the homogeneous solution in Eq. (A.36),

$$z_{ij}(t) = 2{C_1}^{ij} + {C_2}^{ij} sin(\omega t) + {C_3}^{ij} cos(\omega t) + \frac{2u_{ij}}{\omega} t \tag{A.46}$$

Deriving Eq. (A.46) two times yields,

$$\frac{d}{dt} z_{ij}(t) = \dot{z}_{ij}(t) = \omega {C_2}^{ij} cos(\omega t) - \omega {C_3}^{ij} sin(\omega t) + \frac{2u_{ij}}{\omega} \tag{A.47}$$

$$\frac{d}{dt} \dot{z}_{ij}(t) = \ddot{z}_{ij}(t) = -\omega^2 {C_2}^{ij} sin(\omega t) - \omega^2 {C_3}^{ij} cos(\omega t) \tag{A.48}$$

Eq. (A.47) is then substituted into Eq. (A.38)

$$\begin{aligned} &\ddot{x}_{ij} + 2\omega\left(\omega {C_2}^{ij} cos(\omega t) - \omega {C_3}^{ij} sin(\omega t) + \frac{2u_{ij}}{\omega}\right) = u_{ij} \\ &= \ddot{x}_{ij} + 2\omega^2 {C_2}^{ij} cos(\omega t) - 2\omega^2 {C_3}^{ij} sin(\omega t) + 3u_{ij} = 0 \end{aligned} \tag{A.49}$$

Integrating Eq. (A.49) two times yields

$$\iint \ddot{x}_{ij} = \iint -2\omega^2 {C_2}^{ij} cos(\omega t) + 2\omega^2 {C_3}^{ij} sin(\omega t) - 3u_{ij} \tag{A.50}$$

$$\int \dot{x}_{ij} = \int -2\omega\, {C_2}^{ij} sin(\omega t) - 2\omega {C_3}^{ij} cos(\omega t) - 3u_{ij}\, t + A \tag{A.51}$$

$$x_{ij}(t) = \overbrace{2{C_2}^{ij} cos(\omega t) - 2{C_3}^{ij} sin(\omega t)}^{homogenous\ \ solution} \overbrace{-\frac{3}{2} t^2 u_{ij} + At + B}^{particular\ \ solution} \tag{A.52}$$

where A and B are the integration constants. Then Eqs. (A.46), (A.48), and the first derivative of Eq. (A.52) are substituted into Eq. (A.40), and solved for constant A,

$$\ddot{z}_{ij} - 2\omega\dot{x}_{ij} - 3\omega^2 z_{ij} = 0$$

$$\begin{gathered}\left(-\omega^2 {C_2}^{ij} sin(\omega t) - \omega^2 {C_3}^{ij} cos(\omega t)\right) \\ -2\omega\left(-2\omega {C_2}^{ij} sin(\omega t) - 2\omega {C_3}^{ij} cos(\omega t) - 3u_{ij} t + A\right) \\ -3\omega^2\left(2{C_1}^{ij} + {C_2}^{ij} sin(\omega t) + {C_3}^{ij} cos(\omega t) + \frac{2u_{ij}}{\omega} t\right) = 0\end{gathered}$$

$$\begin{gathered}-\omega^2 {C_2}^{ij} sin(\omega t) - \omega^2 {C_3}^{ij} cos(\omega t) + 4\omega^2 {C_2}^{ij} sin(\omega t) + 4\omega^2 {C_3}^{ij} cos(\omega t) + 6\omega u_{ij} t - 2\omega A \\ - 6\omega^2 {C_1}^{ij} - 3\omega^2 {C_2}^{ij} sin(\omega t) - 3\omega^2 {C_3}^{ij} cos(\omega t) - 6\omega u_{ij} t = 0\end{gathered}$$

$$A = -3\omega {C_1}^{ij} \tag{A.53}$$

Substituting Eq. (A.53) into Eq. (A.52) along with Eq. (A.46) yields a closed solution set to the equations of motion in the x-z plane:

$$\begin{cases} x_{ij}(t) = 2{C_2}^{ij} cos(\omega t) - 2{C_3}^{ij} sin(\omega t) \overbrace{-\frac{3}{2} t^2 u_{ij} - 3\omega {C_1}^{ij} t + B}^{particular\ \ solution} \\ z_{ij}(t) = 2{C_1}^{ij} + {C_2}^{ij} sin(\omega t) + {C_3}^{ij} cos(\omega t) + \frac{2u_{ij}}{\omega} t \end{cases} \tag{A.54}$$

To determine B, the solution set is simplified for $t = 0$.

$$\begin{gathered}\rightarrow\ x_{ij}(0) = 2{C_2}^{ij} + B \\ {C_2}^{ij} = \frac{x_{ij}(0) - B}{2} \\ \rightarrow\ \dot{z}_{ij}(0) = \omega {C_2}^{ij} + \frac{2u_{ij}}{\omega} \\ {C_2}^{ij} = \frac{\dot{z}_{ij}(0)}{\omega} - \frac{2u_{ij}}{\omega^2}\end{gathered}$$

$$\begin{gathered}\frac{x_{ij}(0) - B}{2} = \frac{\dot{z}_{ij}(0)}{\omega} - \frac{2u_{ij}}{\omega^2} \\ B = \frac{4u_{ij}}{\omega^2} + \underbrace{x_{ij}(0) - \frac{2\dot{z}_{ij}(0)}{\omega}}_{={C_4}^{ij},\, from\ Eq.\ (A.2.2)}\end{gathered} \tag{A.55}$$

Then substituting Eq. (A.55) into Eqs. (A.54) yields the homogenous and particular solution set to the HCW motion equations, for closed relative trajectories between satellites.

$$\begin{cases} x_{ij}(t) = \overbrace{2{C_2}^{ij}\cos(\omega t) - 2{C_3}^{ij}\sin(\omega t)}^{homogenous\ \ solution} \overbrace{-\frac{3}{2}t^2 u_{ij} - 3\omega {C_1}^{ij} t + B}^{particular\ \ solution} \\ z_{ij}(t) = \overbrace{2{C_1}^{ij} + {C_2}^{ij}\sin(\omega t) + {C_3}^{ij}\cos(\omega t)}^{homogenous\ \ solution} \overbrace{+\frac{2u_{ij}}{\omega}t}^{particular\ \ solution} \end{cases}$$

The solution $y_{ij}(t)$ from Eq. (A.35), normal to the motion plane, remains unchanged by the control vector application, resulting in the solution set presented in Eq. (3.50-3.52).

Appendix B - MATLAB script

B.1 Swarm Source Code

```
clc
close all
clear all

dt = 10; % Simulation time step
T_end = 5*60*60; % Simulation time
T = 0  : dt : T_end-dt;

N = 20;  % Number of satellites in the swarm

for i = 1 : N

  X_i{i}=zeros(13,length(T)); % The state vector of each satellite is set to zero

 for j = 1 : N

  xsat_diff{i,j} = zeros(6,length(T)); % The relative state vector of each satellite is set to zero
  C_constants{i,j} = zeros(6,length(T)); % HCW constants are set to zero

 end

end

clst_sat = zeros(N+1,length(T)); % Pairing links are set to zero
pair = zeros(N,length(T)); % Number of pairs is set to zero

mu = 3.986*10^14; % Gravitational parameter
R_earth = 6.371e6; % Earth's radius
Mass = 10*10^-3; % Satellite mass

%% Initial orbital parameters
Height = 500e3;           % Height of the satellite orbit
Rad = R_earth + Height;
incl_1 = 51.7*pi/180;     % Inclination
epsilon = 0;              % Eccentricity
phi = 0;                  % longitude of the ascending node
omega = 0;                % Argument of the pericenter
t_pi = 0;                 % pericenter time
t_cur = 0;                % current time
approx = 0;               % first step for Newton Method

[r, v, D] = orbitalMotionKeplerian(mu, Rad, epsilon, phi, omega, incl_1, t_pi, t_cur, approx);
% The Keplerian orbital parameters are converted to inital state vactors in the ECI frame

X_i{1}(1:3,1) = r; %
X_i{1}(4:6,1) = v; % Initial state vector of the satellite (ECI)

Omega = cross(X_i{1}(1:3,1),X_i{1}(4:6,1))/norm(X_i{1}(1:3,1))^2; % Orbital angular velocity
A = orbital_dcm(X_i{1}(:,1)); % Transition matrix to HILL reference frame

Force = zeros(N,T_end/dt,3); % The electromagnetic force is set to zero
B = zeros(N,T_end/dt,3); % The magnetic field is set to zero
mdipole = zeros(N,T_end/dt,3); % The magnetic dipole moment is set to zero
sat_dist = zeros(N,N,T_end/dt); % The closeste satellite targets are set to zero
C1_min_value = 0.01; % Minimim relative drift for pair selection
r_min = 0.05; % Minimum distance for dipole calculation
r_min_no_pair = 0.3; %minimum distance between unpaired satellite
r_min_collision_avoid = 0.1; % Minimum distance for collision avoidance
mdipoleMax = 0.01;    % Maximum dipole value
mdipole_collision = 0.0005; % Dipole value for collision avoidance
r_C1_max = 1; % Defined area for pairing method B
C1_max = 0.1; % Maximum relative drift after deployment
N_swarm = 1; % Number of satellites in the swarm after the simulation, if =N no satellites are lost

X_i{1}(7:10,1) = [1 0 0 0]; % Quaternion initial conditions for the first satellite, omega is zero

%% load('dX_defined_coordinates.mat');
% Loads a specific set of initial coordinates and conditions for the satellites

for i = 2 : N % Initial conditions for the swarm

    C_coord(1,i) = random('unif',-C1_max,C1_max); %
    C_coord(2:6,i) = normrnd(0,0.1,5,1);          % Random initial conditions for the swarm

    dX(:,i) = trajectory(norm(Omega),C_coord(:,i),0); % Initial trajectories
```

```
    % Initial state vectors in the HILL frame
    X_i{i}(1:6,1) = [X_i{1}(1:3,1)+A'*dX(1:3,i);X_i{1}(4:6,1)+A'*dX(4:6,i)+cross(Omega,A'*dX(1:3,i))];
    % Quaternion initial conditions, omega is zero
    X_i{i}(7:10,1) = [1 0 0 0];

end

%% Main cycle %%
 opts = odeset('InitialStep',1e-3);

for t = 2 : 1 : length(T)

t/T(end)*dt

  for i = 1 : N % Numerical motion integration

    % Integration of the satellite motion equations
    [~,X_new] = ode45(@(t1,X) Right_part(t,X,A'*squeeze(Force(i,t-1,:))/Mass,squeeze(mdipole(i,t-
1,:)),squeeze(B(i,t-1,:))),[0,dt],X_i{i}(:,t-1),opts);
    X_i{i}(:,t) = X_new(end,:)';
  end

A = orbital_dcm(X_i{1}(:,t)); % Transition matrix to HILL reference frame

  for i = 1 : N  % Calculation of relative satellite vectors, constants, and distances
      for j = 1 : N
          if i ~= j
            % Relative state vector calculation
            xsat_diff{i,j} (:,t) = [A*(X_i{j}(1:3,t) - X_i{i}(1:3,t));A*((X_i{j}(4:6,t) -
X_i{i}(4:6,t))-cross(Omega,(X_i{j}(1:3,t) - X_i{i}(1:3,t))))];
            % Relative motion constants
            C_constants{i,j} (:,t) = coord2const(xsat_diff{i,j}(:,t), norm(Omega));
          end
         sat_dist(i,j,t) = norm(xsat_diff{i,j}(1:3,t)); % Relative distance
      end
  end

%%  Pairing method B (optional - pairing method A must be disabled first)
%   for i = 1 : N % Pairing the satellites according to maximum C1 inside the area of r_C1_max
%
%       C_1_i = zeros(1,N);
%
%       for j = 1:N
%           C_1_i(j) = abs(C_constants{i,j} (1,t));
%       end
%
%       [~,j_max] = sort(C_1_i,'descend'); % Sorts satellites according to relative drift
%
%       for Num = 1:N
%           r = xsat_diff{i,j_max(Num)} (1:3,t);
%           if (abs(C_constants{i,j_max(Num)} (1,t))> C1_min_value) && (norm(r) < r_C1_max)
%              % Selects the nearest satellite with nonzero relative drift
%                 j_maximum = j_max(Num);
%                 clst_sat(i,t) = j_maximum;
%               break;
%           end
%       end
%
%       if Num == N && abs(C_constants{i,j_max(Num)} (1,t))< C1_min_value
%          % Discards pairing option if conditions are not met
%           clst_sat(i,t) = N+1;
%       end
%   end

%% Pairing method A
for i = 1 : N
   [~,j_min] = sort(squeeze(sat_dist(i,:,t))); % Sorts satellites according to relative distance
     for Num = 2:N
         if abs(C_constants{i,j_min(Num)} (1,t))> C1_min_value
            % Selects the nearest satellite with nonzero relative drift
            % and checks pairing conditions
                j_minimum = j_min(Num);
                clst_sat(i,t) = j_minimum;
              break;
         end
     end
         if Num == N && abs(C_constants{i,j_min(Num)} (1,t))< C1_min_value
            % Discards pairing option if conditions are not met
          clst_sat(i,t) = N+1;
         end
end

%% Dipole calculation
for i = 1 : N
     if i == clst_sat(clst_sat(i,t),t)
```

```
        j = clst_sat(i,t);
        pair(i,t) = j; %
        pair(j,t) = i; % Added variable "pair" for figure plot
        u = -norm(Omega)*C_constants{i,j}(1,t)/dt; % Control Vector
        r = xsat_diff{i,j} (1:3,t); % Relative position
        if norm(r) > r_min % Control is applied only if the relative diatance is more than r_min
            mdipole(i,t,:) = [mdipoleMax;0;0];
            mdipole(j,t,:) = dipoles(r,mdipole(i,t,:),u/2*Mass);
            Maximum = max(abs(mdipole(j,t,:)));
            if Maximum > mdipoleMax % Dipole calculation if the maximum established value is exceeded
                mdipole(j,t,:) = mdipole(j,t,:)/Maximum * mdipoleMax;
            end
        end
     end
end

%% If satellites are too close to each other the control is not applied
for i = 1 : N
    for j = 1 : N
        r = xsat_diff{i,j} (1:3,t);
         if (i ~= j) && (norm(r) < r_min_no_pair) % Conditions for satellites too close for pairing
             if (pair(j,t) ~= i) && (norm(squeeze(mdipole(j,t,:))) ~= 0) && (pair(j,t) ~= 0) &&
(pair(i,t) ~= 0)
                 mdipole(j,t,:) = [0;0;0]; % Dipole calculation is cancelled
                 mdipole(pair(j,t),t,:) = [0;0;0];
                 pair(pair(j,t),t) = 0; % Satellite pairing is cancelled
                 pair(j,t) = 0;
             end
         end
    end
end

%% Collision avoidance
for i = 1 : N
    for j = 1 : N
        r = xsat_diff{i,j} (1:3,t);
         if (i ~= j) && (norm(r) < r_min_collision_avoid) && (t > 300/dt) % Collision conditions
                % Dipole calculation for collision avoidance
                mdipole(j,t,:) = r/norm(r)*mdipole_collision;
                mdipole(i,t,:) = -r/norm(r)*mdipole_collision;
         end
    end
end

%% Calculation of the forces acting on all satellties
for i = 1 : N
    for j = 1: N
        r = xsat_diff{i,j}(1:3,t);
         if (i ~= j)
            % Forces acting on a satellite
            Force(j,t,:) = squeeze(Force(j,t,:)) +
ControlForce(r,squeeze(mdipole(i,t,:)),squeeze(mdipole(j,t,:)));
            % Satellites' magnetic fields
            B(i,t,:) = squeeze(B(i,t,:)) + magnetic_field(r,squeeze(mdipole(j,t,:)));
         end
    end
   % The geomagnetic field is considered
   B(i,t,:) = squeeze(B(i,t,:)) + magnetic_field(squeeze(X_i{i}(1:3,t)),[0; 0; -8e22]);
end

end

%% Figure plotting %%
colorm=colormap('Jet');

figure('Color',[1 1 1])
j = 1;

for i = 1 : N

plot3(xsat_diff{i,j}(1,2:end),xsat_diff{i,j}(2,2:end),xsat_diff{i,j}(3,2:end),'LineWidth',2,'Color',colo
rm(i*3,:))
hold on

end
xlabel('x,m')
ylabel('y,m')
zlabel('z,m')
grid on

figure('Color',[1 1 1])
j = 1;   %for the plot

for i = 1 : N
    if i~=j
```

```
        plot(T/3600,C_constants{i,j}(1,:),'LineWidth',2,'Color',colorm(i*3,:))
        hold on

        C_const_end(i) = C_constants{i,j}(1,end);
    end
end
xlabel('Time, hours')
ylabel('C_1')

for i = 1 : N
    if C_const_end(i) < C1_min_value
       N_swarm = N_swarm + 1;
    end
end
figure('Color',[1 1 1])
j = 1;   %for the plot

for i = 1 : N

plot(T/3600,pair(i,:),'*','LineWidth',2,'Color',colorm(i*3,:))
hold on

end
legend('1','2','3','4','5','6','7','8','9','10','11','12','13','14','15','16','17','18','19','20')
xlabel('Time, hours')
ylabel('Number of satellite in pair')


figure('Color',[1 1 1])
j = 1;   %for the plot

for i = 1 : N

plot(T/3600,squeeze(mdipole(i,:,1)),'LineWidth',2,'Color',colorm(i*3,:))
hold on
plot(T/3600,squeeze(mdipole(i,:,2)),'LineWidth',2,'Color',colorm(i*3,:))
plot(T/3600,squeeze(mdipole(i,:,3)),'LineWidth',2,'Color',colorm(i*3,:))

end
xlabel('Time, hours')
ylabel('Dipoles, A*m^2')

figure('Color',[1 1 1])
j = 1;   %for the plot

for i = 1 : N

plot(T/3600,Force(i,:,1),'LineWidth',2,'Color',colorm(i*3,:))
hold on
plot(T/3600,Force(i,:,2),'LineWidth',2,'Color',colorm(i*3,:))
plot(T/3600,Force(i,:,3),'LineWidth',2,'Color',colorm(i*3,:))

end
xlabel('Time, hours')
ylabel('Force, N')


figure('Color',[1 1 1])
j = 1;   %for the plot

for i = 1 : N

plot(T/3600,squeeze(sat_dist(i,j,:)),'LineWidth',2,'Color',colorm(i*3,:))
hold on

end
xlabel('Time, hours')
ylabel('Relative distance for the first satellite')

figure('Color',[1 1 1])
j = 1;   %for the plot

for i = 1 : N

plot(T/3600,X_i{i}(7:10,:))
hold on

end
xlabel('Time, hours')
ylabel('Quaternion components')
```

```
figure('Color',[1 1 1])
j = 1;   %for the plot

for i = 1 : N

plot(T/3600,X_i{i}(11:13,:)*180/pi)
hold on

end
xlabel('Time, hours')
ylabel('Angular velocity, deg/sec')
```

B.2. Keplerian Parameter Conversion to ECI Reference Frame

```
function [r, v, D] = orbitalMotionKeplerian(mu, p, epsilon, phi, omega, inc, t_pi, t_cur, approx)
% returns position and velocity of the satellite in the ECI

% mu - gravitational parameter
% p - semi-latus rectum
% epsilon - eccentricity
% phi - longitude of the ascending node
% omega - argument of the pericenter
% inc - inclination
% t_pi - pericenter time
% t_cur - current time
% approx - first step for Newton Method

if epsilon < 1
    a = p/(1 - epsilon^2);
    b = sqrt(a*p);
    M = sqrt(mu/a^3)*(t_cur - t_pi);
    misclosure = 1;
    D = approx;
    while misclosure > 1e-11
        D = (epsilon*sin(D) - epsilon*cos(D)*D + M)/(1 - epsilon*cos(D));
%         D = D - (D - epsilon*sin(D) - M)/(1 - epsilon*cos(D));
        misclosure = abs(D - epsilon*sin(D) - M);
    end
%     display(D - epsilon*sin(D) - M)
    r1 = [a*(cos(D) - epsilon); b*sin(D); 0];
    cosTheta = (cos(D) - epsilon)/(1 - epsilon*cos(D));
    sinTheta = sqrt(1 - epsilon^2)*sin(D)/(1 - epsilon*cos(D));
    Vr = sqrt(mu/p)*epsilon*sinTheta;
    Vn = sqrt(mu/p)*(1 + epsilon*cosTheta);
    v1 = [Vr*cosTheta - Vn*sinTheta; Vr*sinTheta + Vn*cosTheta; 0];
else
    display('nonelliptic!')
    r = -1;
    v = -1;
    D = -1;
    return;
end
A1 = [cos(phi), sin(phi), 0;...
     -sin(phi), cos(phi), 0;...
        0,        0,    1];

A2 = [1,      0,          0;...
      0,  cos(inc), sin(inc);...
      0, -sin(inc), cos(inc)];

A3 = [cos(omega), sin(omega), 0;...
     -sin(omega), cos(omega), 0;...
           0,         0,      1];

B = (A1')*(A2')*(A3');

r = B*r1;
v = B*v1;
end
```

B.3. Rotation Matrix from ECI to HILL Reference Frame

```
function [ A ] = orbital_dcm(X)
% Rotation matrix to HILL reference frame
```

```
z=X(1:3)/norm(X(1:3));
y=cross(X(1:3),X(4:6))/norm(cross(X(1:3),X(4:6)));
x=cross(y,z);

A=[x,y,z];
A=A';

end
```

B.4. Trajectory Solution for the HCW Equations

```
function [X]=trajectory(w,C,t)
% Solution to the HCW equations
% w is angular velocity

X(:,1)=-3*C(1)*w*t+2*C(2)*cos(w*t)-2*C(3)*sin(w*t)+C(4);
X(:,2)=C(5)*sin(w*t)+C(6)*cos(w*t);
X(:,3)=2*C(1)+C(2)*sin(w*t)+C(3)*cos(w*t);
X(:,4)=-3*C(1)*w-2*C(2)*w*sin(w*t)-2*C(3)*w*cos(w*t);
X(:,5)=C(5)*w*cos(w*t)-C(6)*w*sin(w*t);
X(:,6)=C(2)*w*cos(w*t)-C(3)*w*sin(w*t);

end
```

B.5. HCW Constants

```
function [C] = coord2const( X, w )
% HCW constants calculated from the free motion equation

C(1) = 2*X(3)+X(4)/w;
C(2) = X(6)/w;
C(3) = -3*X(3)-2*X(4)/w;
C(4) = X(1)-2*X(6)/w;
C(5) = X(5)/w;
C(6) = X(2);

end
```

B.6. Dipole Solution

```
clc
close all
clear all
syms m0 ml_1 ml_2 ml_3 mf_1 mf_2 mf_3 x y z u real

ml=[ml_1;0;0];
mf=[mf_1;mf_2;mf_3];
r=[x;y;z];
r_norm=norm(r);
U=[u;0;0];
m0=4*pi*10^-7;

F=3*m0/2/pi*(ml'*mf*r./r_norm^5+ml'*r*mf/r_norm^5+mf'*r*ml/r_norm^5-5*(ml'*r)*(mf'*r)*r/r_norm^7);

S=solve(F-U==0,mf_1,mf_2,mf_3)

simplify(S.mf_1)
simplify(S.mf_2)
simplify(S.mf_3)
```

B.7. Dipole Calculation

```
function [mf] = dipoles(r, ml, u)

x=r(1);
y=r(2);
z=r(3);

m0=4*pi*10^-7;

ml_1=ml(1);
ml_2=ml(2);
```

```
ml_3=ml(3);

mf_1=(2*pi*u*(x^2 + y^2 + z^2)^(3/2)*(- ml_1^2*x^4 + 4*ml_1^2*x^2*y^2 + 4*ml_1^2*x^2*z^2 -
4*ml_1*ml_2*x^3*y + 6*ml_1*ml_2*x*y^3 + 6*ml_1*ml_2*x*y*z^2 - 4*ml_1*ml_3*x^3*z + 6*ml_1*ml_3*x*y^2*z +
6*ml_1*ml_3*x*z^3 - 3*ml_2^2*x^2*y^2 + ml_2^2*x^2*z^2 + 2*ml_2^2*y^4 + 3*ml_2^2*y^2*z^2 + ml_2^2*z^4 -
8*ml_2*ml_3*x^2*y*z + 2*ml_2*ml_3*y^3*z + 2*ml_2*ml_3*y*z^3 + ml_3^2*x^2*y^2 - 3*ml_3^2*x^2*z^2 +
ml_3^2*y^4 + 3*ml_3^2*y^2*z^2 + 2*ml_3^2*z^4))/(3*m0*(ml_1*x + ml_2*y + ml_3*z)*(2*ml_1^2*x^2 +
ml_1^2*y^2 + ml_1^2*z^2 + 2*ml_1*ml_2*x*y + 2*ml_1*ml_3*x*z + ml_2^2*x^2 + 2*ml_2^2*y^2 + ml_2^2*z^2 +
2*ml_2*ml_3*y*z + ml_3^2*x^2 + ml_3^2*y^2 + 2*ml_3^2*z^2));

mf_2=(2*pi*u*(x^2 + y^2 + z^2)^(3/2)*(- 4*ml_1^2*x^3*y + ml_1^2*x*y^3 + ml_1^2*x*y*z^2 + ml_1*ml_2*x^4 -
8*ml_1*ml_2*x^2*y^2 + ml_1*ml_2*y^4 - ml_1*ml_2*z^4 - 8*ml_1*ml_3*x^2*y*z + 2*ml_1*ml_3*y^3*z +
2*ml_1*ml_3*y*z^3 + ml_2^2*x^3*y - 4*ml_2^2*x*y^3 + ml_2^2*x*y*z^2 + 2*ml_2*ml_3*x^3*z -
8*ml_2*ml_3*x*y^2*z + 2*ml_2*ml_3*x*z^3 - ml_3^2*x^3*y - ml_3^2*x*y^3 - 6*ml_3^2*x*y*z^2))/(3*m0*(ml_1*x
+ ml_2*y + ml_3*z)*(2*ml_1^2*x^2 + ml_1^2*y^2 + ml_1^2*z^2 + 2*ml_1*ml_2*x*y + 2*ml_1*ml_3*x*z +
ml_2^2*x^2 + 2*ml_2^2*y^2 + ml_2^2*z^2 + 2*ml_2*ml_3*y*z + ml_3^2*x^2 + ml_3^2*y^2 + 2*ml_3^2*z^2));

mf_3=(2*pi*u*(x^2 + y^2 + z^2)^(3/2)*(- 4*ml_1^2*x^3*z + ml_1^2*x*y^2*z + ml_1^2*x*z^3 -
8*ml_1*ml_2*x^2*y*z + 2*ml_1*ml_2*y^3*z + 2*ml_1*ml_2*y*z^3 + ml_1*ml_3*x^4 - 8*ml_1*ml_3*x^2*z^2 -
ml_1*ml_3*y^4 + ml_1*ml_3*z^4 - ml_2^2*x^3*z - 6*ml_2^2*x*y^2*z - ml_2^2*x*z^3 + 2*ml_2*ml_3*x^3*y +
2*ml_2*ml_3*x*y^3 - 8*ml_2*ml_3*x*y*z^2 + ml_3^2*x^3*z + ml_3^2*x*y^2*z - 4*ml_3^2*x*z^3))/(3*m0*(ml_1*x
+ ml_2*y + ml_3*z)*(2*ml_1^2*x^2 + ml_1^2*y^2 + ml_1^2*z^2 + 2*ml_1*ml_2*x*y + 2*ml_1*ml_3*x*z +
ml_2^2*x^2 + 2*ml_2^2*y^2 + ml_2^2*z^2 + 2*ml_2*ml_3*y*z + ml_3^2*x^2 + ml_3^2*y^2 + 2*ml_3^2*z^2));

mf=[mf_1;mf_2;mf_3];

end
```

B.8. Electromagnetic Force Calculation

```
function [F] = ControlForce(r, ml, mf)

 r_norm = norm(r);

 m0=4*pi*10^-7;

 F=3*m0/2/pi*(ml'*mf*r./r_norm^5+ml'*r*mf/r_norm^5+mf'*r*ml/r_norm^5-5*(ml'*r)*(mf'*r)*r/r_norm^7);

end
```

B.9. Magnetic Field Calculation

```
function [B] = magnetic_field(r, mdipole)

 r_norm = norm(r);
 m0=4*pi*10^-7;
 B = m0/(4*pi)*((3*r*dot(mdipole,r))/r_norm^5 - mdipole/r_norm^3);
```

B.10. Force Model

```
function [dX] = Right_part(t,X,f_a,M,B)

dX(1)=X(4);
dX(2)=X(5);
dX(3)=X(6);
Rad=norm(X(1:3));
mu=3.986*10^14; % Universal gravitational parameter

R = 6378000; % Earth radius
delta = 3/2*1082.8e-6*mu*R^2;
x = X(1);
y = X(2);
z = X(3);
r = [X(1);X(2);X(3)];
acceleration_J2 = delta*r/norm(r)^5*(5*z^2/norm(r)^2 - 1)...
    - 2*delta/norm(r)^5*[0; 0; z]; % J2 effect

dX(4)=-mu*X(1)/Rad^3+acceleration_J2(1)+f_a(1);
dX(5)=-mu*X(2)/Rad^3+acceleration_J2(2)+f_a(2);
dX(6)=-mu*X(3)/Rad^3+acceleration_J2(3)+f_a(3); % Gravitation attraction including J2 perturbations
dX=dX';

%% Controlled angular motion
quaternion = X(7:10);
omega = X(11:13);
```

```
C = [0 omega(3) -omega(2) omega(1);
    -omega(3) 0 omega(1) omega(2);
    omega(2) -omega(1) 0 omega(3);
    -omega(1) -omega(2) -omega(3) 0];

M = quatrotate(quaternion',M')'; % Torque acting on a satellite
B = quatrotate(quaternion',B')'; % Magnetic field acting on a satellite

dX(7:10) = 1/2*C*quaternion;
J = diag([0.8e-6 0.8e-6 1.5e-6]);

Damp_coef = 10;
Damping = Damp_coef*cross(omega,B);
M = M+Damping;
mdipoleMax = 0.01;
Maximum = max(abs(M));
 if Maximum > mdipoleMax
    M = M/Maximum * mdipoleMax;
 end

dX(11:13) = inv(J)*(-cross(omega,J*omega)+cross(M,B));


end
```